A CAHN-HILLIARD APPROACH TO MODELLING PHASE SEPARATION IN BIMETALLIC NANOPARTICLES

by

MOHAMMAD AFRAZ AHMED

A thesis submitted to the
University of Birmingham
for the degree of
DOCTOR OF PHILOSOPHY

School of Metallurgy & Materials
University of Birmingham
July 2015

UNIVERSITY OF
BIRMINGHAM

University of Birmingham Research Archive

e-theses repository

This unpublished thesis/dissertation is copyright of the author and/or third parties. The intellectual property rights of the author or third parties in respect of this work are as defined by The Copyright Designs and Patents Act 1988 or as modified by any successor legislation.

Any use made of information contained in this thesis/dissertation must be in accordance with that legislation and must be properly acknowledged. Further distribution or reproduction in any format is prohibited without the permission of the copyright holder.

Abstract

In this work, a ternary system of Cahn-Hilliard equations is used to model phase separation processes in bimetallic nanoparticles. The third component in the ternary system is taken to be vacuum, such that we are able to simulate bimetallic nanoparticles without any need to impose restrictions on the nanoparticle boundary. Strain effects, due to lattice mismatch, are introduced by coupling with the Navier-Lamé equations. The use of this diffuse-interface approach allows the simulation of significantly larger systems than currently feasible with atomistic methods. Particular attention is paid to the core-shell to quasi-Janus particle transition that has been observed in CuAg and other bimetallic nanoparticles of weakly miscible elements. Our simulations are able to capture the various effects seen previously in experimental work and in atomistic simulations. In particular, we observe a transition from core-shell structure to quasi-Janus particle structure as the size of the particles increases. Moreover, it is shown that core-shell particles prevail when the thickness of the shell is small in comparison to the core size. The inclusion of elastic effects into the model further promotes the formation of quasi-Janus particles. The transition from core-shell to quasi-Janus particle structure is, however, also seen in the absence of elastic effects.

Dedicated to my beloved grandfather,

Haji Mohammed Hussain

(1930-2015).

Acknowledgements

I wish to thank my supervisor, Dr. Nils Warnken, for his support and encouragement throughout my time as a PhD student. This work would not have been possible without him. I would also like to express my gratitude to my co-supervisor, Prof. Roy Johnston, and to Dr. Ivailo Atanasov, for many fruitful discussions regarding my work. In addition, I wish to thank the examiners of my thesis, Prof. Riccardo Ferrando and Dr. Alessandro Mottura, for their advice. I am also grateful to the EPSRC for their financial support.

My thanks go out to all those who have supported me at the University of Birmingham since I came here as an undergraduate, in the School of Physics & Astronomy, in 2006. In particular, I wish to thank Prof. Raymund Jones and Prof. Alberto Vecchio.

Special thanks are reserved for Dr. A. Detta, of the Queen Elizabeth Hospital, and for Dr. Abid Karim, of the Medical School, for their friendship. It has been a great pleasure to know them for the last eight years or so.

I wish to thank my family for their support and patience. In particular, I am forever indebted to my parents. My most sincere thanks also go to my cousin, Asad, for all his support since I came to Birmingham, and for always welcoming me with open arms. Finally, to my grandfather: Thank you for the happiness you brought to my life, and for the love and respect you gave me. It is a great honour to be your grandson. May you rest in peace.

Contents

1 Introduction **1**

1.1 Pattern formation and self-assembly in nanoparticles 3

1.1.1 Factors affecting chemical ordering in nanoalloys 5

1.2 Atomistic simulations 7

1.3 CuAg system 8

1.4 Outline of this work 11

2 Phase-field methods **13**

2.1 Landau theory of phase transitions 15

2.2 Cahn-Hilliard free energy 17

2.3 Free energy of a homogeneous system 20

2.4 Cahn-Hilliard equation 25

2.4.1 Interfacial energy 29

2.4.2 Spinodal Decomposition 30

2.4.3 Ostwald Ripening 33

2.5 Allen-Cahn equation 34

3 Multicomponent systems **35**

3.1 Multiple order parameter phase-field models 35
3.2 Multicomponent Cahn-Hilliard equations 37
3.2.1 Ternary Cahn-Hilliard equations 39
3.2.2 Ternary regular solution 41
3.2.3 Interfacial energy for a ternary system 43

4 Numerical methods for phase-field equations 46
4.1 Finite difference method 48
4.1.1 Boundary conditions 51
4.2 Time discretization 53
4.2.1 Explicit methods 53
4.2.2 Implicit methods 55
4.3 Spectral methods 56
4.4 Exponential Time-Differencing 58
4.5 Unconditionally gradient-stable algorithms 60
4.6 Adaptive time step 63
4.7 Discussion 64

5 Elastic effects caused by lattice mismatch 66
5.1 Stress 71
5.2 The stiffness tensor, C_{ijkl} 72
5.3 Coupling with the Cahn-Hilliard equation 73
5.3.1 Elastic energy 75
5.4 Numerical solution 76

6 Simulations 79

6.1 Dimensionless form of the Cahn-Hilliard equation 81
6.2 Classification of particles 83
6.3 Varying regular solution parameters, Ω_{ij} 85
6.4 Varying composition 99
6.5 Elastic effects 103
6.6 Varying size 108
6.7 CuAg system 112
6.8 Discussion 123

7 Future Work **130**

List of References **132**

List of Figures

1.1 Some of the possible configurations of a binary nanoparticle: a) Core-shell, b) Janus particle, c) Mixed d) Three-shell/onion-like. Reprinted with permsision from Ferrando *et al.*, *Chem. Rev.* 108(3), 845-910 (2008). Copyright 2008 American Chemical Society. 5

1.2 Quasi-Janus and ball-and-cup configurations. 6

2.1 Double-well form of the free energy, given by equation (2.22). 25

2.2 Diffuse interface with hyperbolic tangent profile. 28

2.3 Numerical solution of Cahn-Hilliard equation, showing the process of spinodal decomposition. 33

2.4 Numerical solution of Cahn-Hilliard equation, showing the process of Ostwald ripening. 34

3.1 Plot of the free energy of a ternary regular solution. In this case, all Ω_{ij} are equal. The height represents the energy, while the other two axes represent the composition of two of the components. 42

3.2 Numerical solution of the ternary Cahn-Hilliard equations, with the bulk free energy given by the ternary regular solution model; red, blue and white represent the three components. 43

4.1 9-point stencil used for calculating the finite difference approximation of the Laplacian in 2D. 51

4.2 *Ghost nodes* are in yellow. 53

5.1 Material in the undeformed, reference state undergoes a deformation which displaces the material from $\mathbf{x}'$ to $\mathbf{x}$. 67

5.2 Numerical solution of the binary Cahn-Hilliard equation with elastic effects included. 78

6.1 Structure of the code. 80

6.2 $\delta_{\text{off}-\text{centre}}$ for a core-shell and quasi-Janus particle. 85

6.3 Numerical solution of the ternary Cahn-Hilliard equations with $\Omega_{\text{blue}-\text{red}} = 3.0, \Omega_{\text{red}-\text{white}} = 3.0, \Omega_{\text{blue}-\text{white}} = 3.0$, grid size: 128x128, $\Delta t = 1 \times 10^{-4}$. 86

6.4 Numerical solution of the ternary Cahn-Hilliard equations with $\Omega_{\text{blue}-\text{red}} = 2.0, \Omega_{\text{red}-\text{white}} = 3.5, \Omega_{\text{blue}-\text{white}} = 3.5$, grid size: 128x128, $\Delta t = 1 \times 10^{-4}$. 87

6.5 Numerical solution of the ternary Cahn-Hilliard equations with $\Omega_{\text{blue}-\text{red}} = 3.5, \Omega_{\text{red}-\text{white}} = 3.5, \Omega_{\text{blue}-\text{white}} = 3.5$, grid size: 256×256, $\Delta t = 1 \times 10^{-4}$. 87

6.6 Variation of $\delta_{\text{off}-\text{centre}}$ with dimensionless time, t. The graph corresponds to the simulation shown in figure 6.5. 88

6.9 Variation of $\delta_{\text{off}-\text{centre}}$ with $\Omega_{\text{blue}-\text{white}}$ for fixed $\Omega_{\text{blue}-\text{red}} = 3.0$ and $\Omega_{\text{red}-\text{white}} = 4.0$. 90

6.7 Numerical solution of the ternary Cahn-Hilliard equations with $\Omega_{\text{blue}-\text{red}} = 3.0, \Omega_{\text{red}-\text{white}} = 3.5, \Omega_{\text{blue}-\text{white}} = 4.0$, grid size: 256×256, $\Delta t = 1 \times 10^{-5}$. 91

6.8 Steady-state solutions obtained for $\Omega_{\text{blue}-\text{red}} = 3.0$ and $\Omega_{\text{red}-\text{white}} = 4.0$, while increasing $\Omega_{\text{blue}-\text{white}}$ from fig. a) to fig. f) 92

6.10 Numerical solution of the ternary Cahn-Hilliard equations with $\Omega_{\text{blue}-\text{red}} = 3.0, \Omega_{\text{red}-\text{white}} = 4.0, \Omega_{\text{blue}-\text{white}} = 4.0$, grid size: 256×256, $\Delta t = 1 \times 10^{-5}$. 93

6.11 Numerical solution of the ternary Cahn-Hilliard equations with $\Omega_{\text{blue}-\text{red}} = 3.0, \Omega_{\text{red}-\text{white}} = 4.0, \Omega_{\text{blue}-\text{white}} = 4.5$, grid size: 256×256, $\Delta t = 1 \times 10^{-5}$. 94

6.12 Numerical solution of the ternary Cahn-Hilliard equations with $\Omega_{\text{blue}-\text{red}} = 3.0, \Omega_{\text{red}-\text{white}} = 4.0, \Omega_{\text{blue}-\text{white}} = 5.0$, grid size: 256×256, $\Delta t = 1 \times 10^{-5}$. 95

6.13 Numerical solution of the ternary Cahn-Hilliard equations with $\Omega_{\text{blue}-\text{red}} = 3.0, \Omega_{\text{red}-\text{white}} = 4.0, \Omega_{\text{blue}-\text{white}} = 5.5$, grid size: 256×256, $\Delta t = 1 \times 10^{-6}$. 96

6.14 Numerical solution of the ternary Cahn-Hilliard equations with $\Omega_{\text{blue}-\text{red}} = 3.0, \Omega_{\text{red}-\text{white}} = 4.0, \Omega_{\text{blue}-\text{white}} = 6.0$, grid size: 256×256, $\Delta t = 7 \times 10^{-7}$. 97

6.15 Numerical solution of the ternary Cahn-Hilliard equations with $\Omega_{\text{blue}-\text{red}} = 3.0, \Omega_{\text{red}-\text{white}} = 4.0, \Omega_{\text{blue}-\text{white}} = 6.5$, grid size: 256×256, $\Delta t = 6 \times 10^{-7}$. 98

6.16 Steady-state solutions obtained for a blue : red ratio of 20 : 80. $\Omega_{\text{blue-red}} = 3.0$, $\Omega_{\text{red-white}} = 4.0$, $\Omega_{\text{blue-white}} = 6.0$. 100

6.17 Steady-state solutions obtained for a blue : red ratio of 30 : 70. $\Omega_{\text{blue-red}} = 3.0$, $\Omega_{\text{red-white}} = 4.0$, $\Omega_{\text{blue-white}} = 6.0$. 100

6.18 Steady-state solutions obtained for a blue : red ratio of 40 : 60. $\Omega_{\text{blue-red}} = 3.0$, $\Omega_{\text{red-white}} = 4.0$, $\Omega_{\text{blue-white}} = 6.0$. 101

6.19 Steady-state solutions obtained for a blue : red ratio of 50 : 50. $\Omega_{\text{blue-red}} = 3.0$, $\Omega_{\text{red-white}} = 4.0$, $\Omega_{\text{blue-white}} = 6.0$. 101

6.20 Steady-state solutions obtained for a blue : red ratio of 60 : 40. $\Omega_{\text{blue-red}} = 3.0$, $\Omega_{\text{red-white}} = 4.0$, $\Omega_{\text{blue-white}} = 6.0$. 102

6.21 steady-state solutions obtained for varying blue : red ratios, going from 30 : 70 in a) to 80 : 20 in f). Blue and red together occupy 30% of the system. $\Omega_{\text{blue-red}} = 3.0$, $\Omega_{\text{red-white}} = 4.0$, $\Omega_{\text{blue-white}} = 5.0$. 102

6.22 Simulation with 5% lattice mismatch included; $\Omega_{\text{blue-red}} = 3.0, \Omega_{\text{red-white}} = 4.0, \Omega_{\text{blue-white}} = 6.0$; grid size: 128×128, $\Delta t = 5 \times 10^{-7}$. 104

6.23 Simulation with 10% lattice mismatch included; $\Omega_{\text{blue-red}} = 3.0, \Omega_{\text{red-white}} = 4.0, \Omega_{\text{blue-white}} = 6.0$; grid size: 128×128, $\Delta t = 5 \times 10^{-7}$. 105

6.24 Comparison of steady-state solutions obtained for $\Omega_{\text{blue-red}} = 3.0, \Omega_{\text{red-white}} = 4.0, \Omega_{\text{blue-white}} = 6.0$, a) without elasticity, b) with 10% misfit. 106

6.25 Simulation with 15% lattice mismatch included; $\Omega_{\text{blue-red}} = 3.0, \Omega_{\text{red-white}} = 4.0, \Omega_{\text{blue-white}} = 6.0$; grid size: 128×128, $\Delta t = 1 \times 10^{-8}$. 107

6.26 steady-state solutions for $\Omega_{\text{blue-red}} = 3.0, \Omega_{\text{red-white}} = 4.0, \Omega_{\text{blue-white}} = 5.5$. The domain length in b) is double that in a). 109

6.27 $\Omega_{\text{blue-red}} = 3.0, \Omega_{\text{red-white}} = 4.0, \Omega_{\text{blue-white}} = 5.5$, domain length = $4\sqrt{2}\pi$nm (double that used in figure 6.13); grid size = 256×256, $\Delta t = 1 \times 10^{-6}$. 110

6.28 $\Omega_{\text{blue-red}} = 3.0, \Omega_{\text{red-white}} = 4.0, \Omega_{\text{blue-white}} = 5.0$, domain length = $\sqrt{2}\pi$nm, i.e. half the length of the simulation box used in figure 6.12. 111

6.29 Simulation of CuAg system, $\xi = 5$; grid size = 256×256, $\Delta t = 1 \times 10^{-}6$. 115

6.30 Simulation of CuAg system, $\xi = 4$; grid size = 256×256, $\Delta t = 3 \times 10^{-8}$. 116

6.31 steady-state solutions for CuAg system, with blue : red composition ratios varying from 30 : 70 to 80 : 20. The particle accounts for 40% of the system size. Grid size = 256×256; $\Delta t = 1 \times 10^{-6}$. 117

6.32 Simulation of CuAg system, $\xi = 5$, domain length = $6\sqrt{2}\pi$nm. 118

6.33 Simulation of CuAg system, $\xi = 5$, domain length = $20\sqrt{2}\pi$nm. 119

6.34 Simulation of CuAg system, $\xi = 5$, domain length = $40\sqrt{2}\pi$nm. 120

6.35 CuAg system, $\xi = 5$, domain length = $80\sqrt{2}\pi$nm, grid size = 800×800, $\Delta t = 3 \times 10^{-9}$. 121

6.36 CuAg system, with elastic effects included, $\xi = 5$, domain length = $10\sqrt{2}\pi$nm. 122

6.37 Spherical cap model for Janus nanoparticles. 125

6.38 Comparison of simulation results with an analytical model. $\Omega_{\text{red}-\text{blue}} = 3.0$ and $\Omega_{\text{red}-\text{white}} = 4.0$ in each case, while $\Omega_{\text{blue}-\text{white}}$ is varied. 126

6.39 Core-shell particles are seen in the analytical model when $\Omega_{\text{blue}-\text{white}} > \Omega_{\text{red}-\text{white}} + \Omega_{\text{blue}-\text{red}}$. Although the core is off-centred, it is beneath the surface, and hence equivalent to a centred core-shell particle in the analytical model. 127

Chapter 1

INTRODUCTION

Nanoparticles — particles consisting of several individual atoms or molecules, and generally defined as having a diameter between 1nm and 100nm — have attracted a great deal of attention from the scientific community in recent years, due to the fact that their properties show distinct variations from those of both the corresponding bulk material and of smaller molecules [1]. Furthermore, the inclusion of two or more different atomic species in a nanoparticle leads to a large number of possible chemical configurations that a nanoparticle of any given composition may adopt, with different configurations and morphologies often exhibiting distinct properties to one another. This leads to a high degree of tunability, thus paving the way to a vast array of possible applications in fields such as magnetics [2], optics [3], medicine [4] and catalysis [5].

Of particular significance to the properties of nanoparticles is the large surface-to-volume ratio, which leads to surface atoms having a far greater influence than they would in the corresponding bulk material. This provides opportu-

nities in the field of catalysis, since smaller amounts of a catalyst in nanoparticle form are required to provide the same catalytic activity, thus reducing expenditure. In this context, bimetallic *core-shell* nanoparticles can offer a more economical approach. A core-shell particle consists of a core of one element surrounded by a shell of another element. Thus, by utilising core-shell particles with a core made of a cheaper metal than the shell, it is possible to reduce the cost of catalysts further. Pt, for example, is used as a catalyst in solid oxide fuel cells. Due to its cost, however, it is increasingly being alloyed with other elements, such as Ir and Ru in a core-shell configuration. In certain cases, it has been shown that alloying in this way can also provide enhanced catalytic properties compared to pure nanoparticles. Core-shell Pt-Ru nanoparticles are an example, and have been shown to be more effective than monometallic Pt nanoparticles in the oxidation of CO in fuel cells [6].

In biomedicine, nanoparticles have found applications as markers used for detecting protein and DNA sequences [1, 4], and in targeted drug delivery and targeted cancer therapy. Ag nanoparticles have been shown to exhibit anti-bacterial properties [7, 8]. Monometallic magnetic nanoparticles, as well as bimetallic nanoparticles containing a constituent magnetic element alloyed to a non-magnetic element, have been used in cancer therapy and targeted drug delivery [1], and are also touted as future materials for high-density magnetic recording devices, such as hard disk drives [1].

Modelling the size-dependence of the properties of nanoparticles is essen-

tial, both as a tool for gaining fundamental insights into the physics of the system, and in order to guide future experiments, ultimately leading to new technological applications. To date, the vast majority of modelling studies have been focused on atomistic computational methods such as Density Functional Theory (DFT), Monte Carlo methods and Molecular Dynamics simulations. However, due to limitations on currently available computational resources, atomistic simulations are restricted to the modelling of systems consisting of approximately 10^4 atoms or less, and modelling the transition to bulk is not feasible.

1.1 Pattern formation and self-assembly in nanoparticles

Bimetallic nanoparticles — or *nanoalloys* — consist of a mixture of two types of atom. For a given number of atoms, the chemical arrangement of a bimetallic nanoparticle may depend on several contributory factors, including the relative sizes of the constituent atoms, the relative surface energies and the relative bond strengths of the three types of bond present. The various chemical arrangements that a bimetallic nanoparticle may adopt are outlined below [1, 9], and an illustration is provided in figure 1.1.

Core-shell nanoparticles

Core-shell nanoparticles are — as their name suggests — nanoparticles which have a core of one element surrounded by a shell of the other element. This

morphology is energetically favourable in cases where there is a significant difference in the surface energies of the constituent elements, with the shell then consisting of the element with the lower surface energy.

Janus nanoparticles

Janus particles are side-segregated particles with two faces at the surface, and with an interface between both faces. Similar to Janus particles are the so-called *quasi-Janus* and *ball-and-cup* configurations. In Quasi-Janus nanoparticles the core is displaced to an off-centre position. However, a thin layer of the other element still surrounds the core. Ball-and-cup nanoparticles have a distinctly curved interface between the two constituent elements of the nanoparticle; however, the interface is only found on one side of the particle. An illustration of quasi-Janus and ball-and-cup configurations is shown in figure 1.2.

Mixed nanoparticles

The placement of atoms in a mixed nanoparticle can be either ordered or random, as shown in figure 1.1.

Multi-shell nanoparticles

Multi-shell nanoparticles consist of several layered onion-like shells, with the shells alternating between the two constituent types of atom.

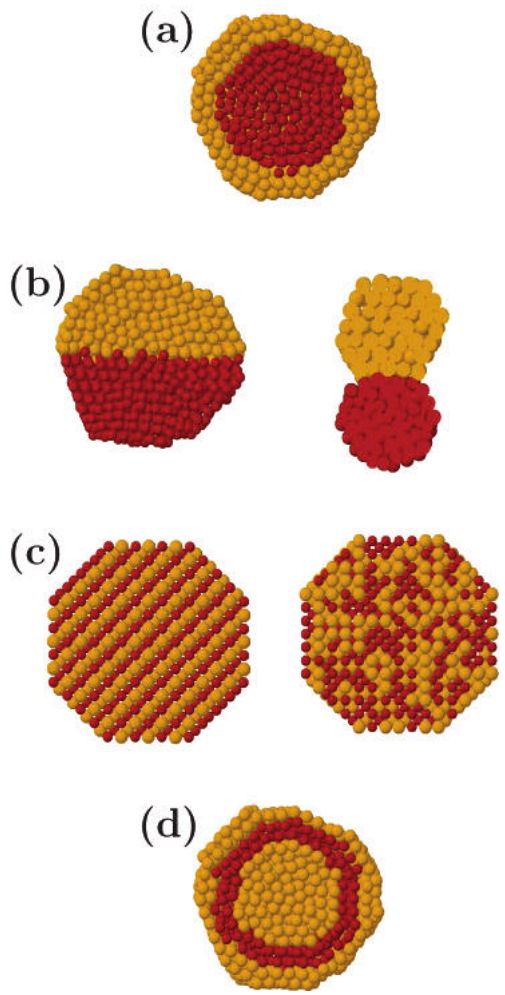
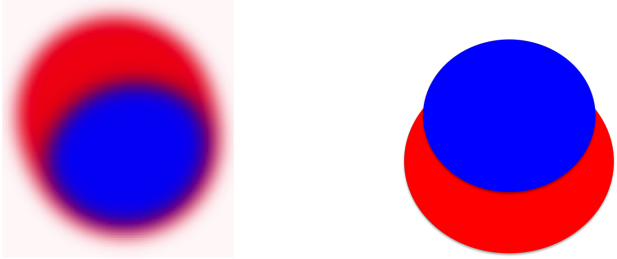


Figure 1.1: Some of the possible configurations of a binary nanoparticle: a) Core-shell, b) Janus particle, c) Mixed d) Three-shell/onion-like. Reprinted with permsision from Ferrando *et al.*, *Chem. Rev.* 108(3), 845-910 (2008). Copyright 2008 American Chemical Society.

1.1.1 Factors affecting chemical ordering in nanoalloys

The main factors affecting the chemical ordering of bimetallic nanoparticles are given below [1, 9]. In general, the configuration of a given nanoalloy is dependent upon a combination of these factors, as well as the particular



Quasi-Janus configuration Ball-and-cup configuration

Figure 1.2: Quasi-Janus and ball-and-cup configurations.

conditions in which the nanoalloy is generated.

Relative bond strengths

Given a nanoalloy consisting of atoms of type A and B, strong A-B bonds will favour mixed configurations. If, on the other hand, A-A or B-B bonds are the strongest, this will favour segregation in the nanoalloy.

Relative surface energies

The element with the lower surface energy will usually be found at the surface, in order to minimise the surface contribution to the free energy.

Relative atomic sizes

The element having the smaller atomic size will typically be positioned in the core, as this can minimise the elastic strain due to lattice mismatch.

Charge transfer

The transfer of electrons between elements with differing electronegativities favours mixed configurations, such that attractive Coulombic interactions are

maximised.

Strength of binding to substrate or surfactant

In the case of supported or passivated nanoparticles, there is a tendency for the element which binds most strongly to the substrate or surfactant to be positioned nearer the surface.

1.2 Atomistic simulations

The last few decades have seen a tremendous increase in computational resources available, and as a result, computer simulation has become an essential tool in the armoury of the scientist. In the field of nanoscience, recent years have seen the overlapping of experimental and computational length scales, with high-precision experimental apparatus allowing the study of smaller nanoclusters, and advances in computational hardware leading to the study of ever-larger nanoclusters.

As far as bimetallic nanoparticles are concerned, the main aim of a simulation is to find the most stable structure for a system, given a particular set of conditions (e.g. the total number of atoms, the composition, the temperature etc.). However, as the number of atoms increases, there is a factorial increase in the number of possible chemical arrangements, making it a difficult task to find the structure with the lowest energy. The possible configurations for a fixed number of atoms and fixed composition, and for the same overall structure are known as *homotops* [1, 9], with the number of homotops given

by

$$\frac{N!}{N_A!N_B!} = \frac{N!}{N_A!(N-N_A)!}\,, \tag{1.1}$$

where N_A and N_B are the number of atoms of type A and type B respectively, and where $N = N_A + N_B$ is the total number of atoms. A cluster consisting of 15 atoms of type A and 15 of type B, for example, gives rise to 155117520 homotops! Many of these will be equivalent due to symmetry. Nevertheless, this poses a challenging problem.

1.3 CuAg system

Nanoalloy systems of weakly miscible metals, such as CuAg, tend to adopt phase-separated configurations. In the case of CuAg, there are several reasons for this. The presence of a considerably large lattice mismatch of approximately 12% between Cu and Ag induces elastic strain and promotes the segregation of the larger Ag atoms to the surface of the nanoparticle. Moreover, the lower cohesiveness and lower surface energy of Ag compared to Cu both favour the segregation of Ag to the surface [10].

Recent experiments and computer simulations have shown that CuAg nanoparticles undergo size-dependent structural phase transitions. At the lower end of the scale, CuAg nanoparticles tend to have a core-shell structure with a Cu core surrounded by an Ag shell, such that the surface contribution to the free energy is minimised. It has been found, however, that as the size of the particles is increased, a transition from core-shell structure to quasi-Janus

structure occurs, in which the two elements are separated and the Cu core is off-centred, while still being coated in a thin layer of Ag (see figure 1.2) [11, 12].

The experimental literature on Cu-Ag nanoparticles is still somewhat limited [1]. The last few years have, however, seen an increased interest in the system, and several experimental studies of Cu-Ag nanoparticles have been conducted [11, 12, 13, 14, 15, 16, 17, 18]. Cazayous et al. [14] have recently used the method of vapour deposition to synthesise CuAg nanoparticles under ultra-high vacuum, depositing the nanoparticles onto a thin amorphous carbon film, resulting in core-shell particles with a Cu core and Ag shell. The results of Langlois et al., using the same techniques, have also confirmed this [11]. They obtained nanoparticles of the order of 25nm and found that a Cu core size of under 12nm leads to core-shell structures. For core sizes above 12nm, they found that almost no particles conform to a core-shell structure, with evidence of the generation of Janus particles. In 2012, Langlois and coworkers [12] studied CuAg nanoparticles of various chemical compositions, synthesised via pulsed laser deposition. They concluded that there is a dependence of the configuration on the amount of Ag present, with a core-shell configuration being adopted for an Ag shell thickness under 4nm and a Janus configuration otherwise. Pellarin et al. [18] have recently conducted experiments on smaller CuAg nanoparticles of the order of 5nm in diameter, and have suggested that the nanoparticles most probably adopt a core-shell configuration.

Several computational studies of CuAg nanoparticles have also been conducted recently [1, 12, 19, 20, 21, 22, 23, 24]. Global optimisation studies of small clusters consisting of 30–40 atoms have shown that core-shell structures are, in general, preferred [21, 25]. These results have also been verified by further optimisation at the DFT level [26]. Global optimisation of 34, 38 and 98 atom clusters of CuAg have been performed in ref. [27], with the global minima corresponding to core-shell structures for all compositons. DFT calculations were also carried out to confirm some of the results obtained for the 38 atom clusters. Molecular dynamics simulations of the growth of CuAg nanoparticles by deposition — whereby Ag atoms are deposited onto a core of Cu or vice versa — have given rise to stable core-shell structures or metastable onion-like structures consisting of three layers [1, 19, 20].

The experimental work of Langlois and co–workers, mentioned previously [12], was supported with DFT calculations and molecular dynamics simulations, for small clusters, which suggested the formation of off-centre Cu cores in Ag-rich clusters. Bochicchio and Ferrando [28, 29] have studied the global optimisation of CuAg in various structural motifs and have found that off-centred cores are preferable in all cases. They did, however, find that for icoashedral particles, a centred core is preferable for small Cu core sizes, and that there is a transition to a particle with an off-centred core as the size of the Cu core is increased.

1.4 Outline of this work

The aim of this work is to develop a new approach for modelling bimetallic nanoparticles, whereby atomistic calculations are coupled to a continuum-scale method. The proposed continuum-scale method is the so-called *phase-field method*, which has been widely used in the modelling of processes such as solidification [30], dendritic growth and spinodal decomposition [31]. We pay particular attention to the CuAg system and its size-dependent properties.

The phase-field method is a *diffuse-interface* approach to modelling the evolution of a thermodynamic system. The general idea behind the method is to choose an *order parameter* which takes on distinct values in the different phases/components of the system and varies smoothly at the interface between the phases/components, such that the interface has a finite width. The method is based upon a Cahn-Hilliard/Ginzburg-Landau formulation of a free energy functional of the order parameter, ϕ. One may then derive a partial differential equation that governs the time evolution of ϕ, with the particular form of the equation being dependent upon whether ϕ corresponds to a conserved or non-conserved quantity. In this way, the whole domain may be governed by a single PDE (for a binary system), and interfaces are tracked automatically. In terms of its application to modelling nanoparticles, the phase-field method allows us to simulate significantly larger system sizes than would be possible with atomistic methods. Moreover, it is possible to exclude certain effects, such as elasticity, from the model, thus allowing us

to probe the influence of different properties separately.

An outline of this thesis is as follows. In Chapter 2, the phase-field method is introduced, and in particular, we pay attention to the Cahn-Hilliard theory [32]. In Chapter 3, the ideas laid down in Chapter 2 are extended to account for multicomponent systems. In Chapter 4, we provide an overview of the numerical methods typically used in the solution of the phase-field equations. The effects of lattice mismatch, and the coupling of elasticity to phase-field models is discussed in Chapter 5. In Chapter 6, phase-field simulations of bimetallic nanoparticles are presented, followed by a discussion of the results obtained. Finally, in Chapter 7 possibilites for future work are discussed.

Chapter 2

PHASE-FIELD METHODS

In the last few decades, the modelling of phase transformations on the continuum scale has been carried out using either *sharp-interface models* or *diffuse-interface models* [33]. An example of a sharp-interface model is the *Stefan problem* [34, 35], in which a two-phase material with a moving boundary/interface between the phases is modelled. In such models, the interface between phases is considered to have zero width. The problem is formulated as a set of coupled differential equations, with one differential equation needed for each phase. In addition, boundary conditions must also be applied at the interface. For this reason, sharp interface methods require explicit tracking of the location of the interface. In two and three spatial dimensions, and particularly for complex morphologies, sharp interface models can thus become complicated to solve, due to the difficulty in tracking the interface [36].

In *phase-field* models, one defines an *order parameter*, ϕ (also known as the *phase-field*) over the entire domain of the system. This order parameter is defined in such a way that it has a distinct, constant value in each of the

constituent phases of the system, while varying continuously at the interfaces between the phases. The free energy of the system, or alternatively the entropy, is then formulated in terms of the order parameter. Taking into account the minimization of the free energy, or the maximization of the entropy [37], and imposing any constraints or conservation laws on the system then gives us the equations that govern the evolution of the system. The advantage of such an approach over the sharp-interface models is that the interface is taken into account automatically, with no requirement to impose boundary conditions at the interface, or to track the interface explicitly, thus leading to a reduction in the number of differential equations to be solved, and also, therefore, in the complexity of the model.

As an example, in modelling the solidification of a pure material, it is natural to define the order parameter, $\phi(x)$, as the local fraction of solid material present at the point x. Thus, ϕ would take the value 0 in the liquid phase and 1 in the solid phase, with a smooth variation between 0 and 1 at the solid/liquid interface. Phase-field models may be split into effectively two groups. The particular solidifcation example mentioned here belongs to the type of phase-field model in which the order parameter corresponds to an actual physical quantity. This class of methods has been applied to modelling solid-state phase transformations [37]. On the other hand, there are phase-field models in which the order parameter is merely phenomenological in nature, and does not correspond to any physically measurable quantity. In this case, the introduction of the order parameter simply serves as a tool to avoid explicit tracking of the interface [36].

The foundations of the phase-field method lie in the work of Cahn and Hilliard in the 1950s and 60s [32], [38], [39]. The method's basis is in considering the free energy functional of a heterogeneous system to be a function of the composition (the order parameter) and the gradients of the composition — an idea first put forward by van der Waals in developing his square gradient theory [40]. The work of Cahn and Hilliard led to the derivation of what is now known as the Cahn-Hilliard equation for conserved order parameters, which has been used to model processes such as spinodal decomposition, nucleation, Ostwald ripening and solid-state phase transformations in binary alloys. These ideas were further developed by Allen and Cahn [41], after whom the Allen-Cahn equation for non-conserved order parameters is named. The majority of phase-field models which have appeared in later years can be traced back to the Cahn-Hilliard and Allen-Cahn equations. An example is the popular model of Wheeler, Boettinger and McFadden [42], who modelled isothermal solidifcation in binary alloys using a coupling of a Cahn-Hilliard type equation for the composition to an Allen-Cahn equation for the non-conserved liquid fraction.

2.1 Landau theory of phase transitions

Since the development of phase-field models was heavily influenced by the Landau mean-field theory, it is instructive to begin with a discussion of the Landau theory of phase transitions and the role of an *order parameter* in the description of first- and second-order phase transitions. A phase transition is

an abrupt change-of-state of matter in response to an infinitesimal change of some parameter (e.g. temperature, pressure, density etc.). As a result, a system undergoing a phase transition goes from a *disordered* state to an *ordered* state or vice versa. Since this change is abrupt, it follows that the free energy must be a non-analytic (discontinuous) function of the variable, X, where X is the parameter which has changed to induce the phase transition [43]. This non-analyticity may arise, for example, if there is a discontinuity in $\partial F/\partial X$ or $\partial^2 F/\partial X^2$ at a *critical point*, giving rise to a first- or second-order phase transition respectively.

The aim of Landau theory is to deduce an approximate form for the free energy, F, which is adequate in describing the properties of the system, as follows. We begin by defining an *order parameter*, ϕ, for the system. The order parameter is used to distinguish between the ordered and disordered states, and it is usually chosen such that it is zero in the disordered state and has some finite value in the ordered state.

The main assumption in Landau theory is that fluctutations of the order parameter are negligible, and hence, only the mean value of the order parameter is used in order to calculate thermodynamic quantities. Landau therefore postulated that the free energy density, $f(T, \phi)$, of the system may be written as a power series in the order parameter, ϕ [44, 45],

$$f(T, \phi) = f(T, \phi = 0) + \sum_{n=2} \frac{a_n(T)}{n} \phi^n \,, \tag{2.1}$$

while taking into account the symmetry of the system, such that any terms which would lead to a violation of the symmetry are neglected. Here, a_n is a constant that generally depends on the temperature, T.

2.2 Cahn-Hilliard free energy

Since the Landau theory of phase transitions neglects fluctuations, it is only possible to use it in the description of the bulk properties of a system. However, many properties of real systems are goverened by the interfaces between phases. It is therefore necessary to construct a theory which accounts for the effects of interfaces, and this is the goal of Cahn-Hilliard theory.

Cahn and Hilliard [32] assumed that the free energy density of a system may be expanded as a function of the order parameter and derivatives of the order parameter, with the derivatives accounting for spatial variations across interfaces. This approach was not, in fact, a new one, and was actually first proposed in 1893 by van der Waals who used it to describe the liquid-gas interface in a one-component system [40]. It was later reinvented by Landau and Lifshitz in their theory of magnetic domain structure [40] and was used by Ginzburg and Landau in their theory of superconductivity [46].

Consider the total free energy functional of a two-phase system, $F[\phi, T]$, such that

$$F[\phi, T] = \int_V f(\phi, T) \mathrm{d}V \,, \tag{2.2}$$

where $f(\phi, T)$ is the free energy density of the system, and the integral is over the whole volume of the system. ϕ is known as an *order parameter*, usually defined as

$$\phi = \begin{cases} 1 & \text{ordered phase} \\ 0 & \text{disordered phase} \end{cases}$$

with ϕ varying smoothly across the interface between the two phases, $0 < \phi < 1$. Following the approach of Cahn and Hilliard [32], we expand the free energy density, $f(\phi, \nabla\phi, \nabla^2\phi, ...)$, about f_0 — the free energy of the system when the system is uniform throughout — in order to correct for nonhomogeneous effects. Thus,

$$\begin{aligned} f(\phi, \nabla\phi, \nabla^2\phi, ...) &= f(\phi, 0, 0, ...) + \left.\frac{\partial f}{\partial \phi}\right|_0 (\phi - \phi) + \left.\frac{\partial f}{\partial \nabla\phi}\right|_0 \nabla\phi + ... \\ &\quad + \left.\frac{\partial f}{\partial \nabla^2\phi}\right|_0 (\nabla^2\phi) + ... \\ &\quad + \frac{1}{2}\Bigg[\left.\frac{\partial^2 f}{\partial(\nabla\phi)^2}\right|_0 (\nabla\phi)^2 + \left.\frac{\partial^2 f}{\partial(\nabla^2\phi)^2}\right|_0 (\nabla^2\phi)^2 \\ &\quad + 2\left.\frac{\partial^2 f}{\partial(\nabla\phi)\partial(\nabla^2\phi)}\right|_0 (\nabla\phi)^3 + ...\Bigg] + ... \qquad (2.3) \\ &= f_0(\phi) + \kappa_1\nabla\phi + \kappa_2\nabla^2\phi + \kappa_3(\nabla\phi)^2\,, \qquad (2.4) \end{aligned}$$

where the subscript, 0, refers to the case in which the system is uniform throughout, and where

$$\kappa_1 = \left.\frac{\partial f}{\partial(\nabla\phi)}\right|_0, \qquad \kappa_2 = \left.\frac{\partial f}{\partial(\nabla^2\phi)}\right|_0, \qquad \kappa_3 = \frac{1}{2}\left.\frac{\partial^2 f}{\partial(\nabla\phi)^2}\right|_0. \quad (2.5)$$

Terms higher than second-order have been neglected. Since the free energy is invariant to changes in the sign of a coordinate, terms involving odd orders of differentiation are set to zero. Hence, $\kappa_1 = 0$, and the total free energy of the system may be written as

$$F[\phi, T] = \int_V \left(f_0(\phi, T) + \kappa_2 \nabla^2 \phi + \kappa_3 (\nabla \phi)^2 \right) \mathrm{d}V \,. \tag{2.6}$$

Let us now consider the second term in this equation and use the divergence theorem, to obtain

$$\int_V \kappa_2 \nabla^2 \phi \, \mathrm{d}V = \kappa_2 \nabla \phi \cdot \mathbf{n} \, \mathrm{d}S - \int_V \nabla \kappa_2 \nabla \phi \, \mathrm{d}V \,. \tag{2.7}$$

In one dimension, $\kappa_2 \nabla \phi = \kappa_2 \frac{\mathrm{d}\phi}{\mathrm{d}x}$, and therefore the first term in equation (2.7) is zero, as before, due to symmetry. In higher dimensions, we may choose the boundary of integration such that $\nabla \phi \cdot \mathbf{n} = 0$ at the boundary. Hence,

$$\int_V \kappa_2 \nabla^2 \phi \, \mathrm{d}V = - \int_V \frac{\mathrm{d}\kappa_2}{\mathrm{d}\phi} (\nabla \phi)^2 \, \mathrm{d}V \,. \tag{2.8}$$

We may therefore write the free energy as

$$F[\phi, T] = \int_V \left(f_0(\phi, T) + \frac{\kappa}{2} (\nabla \phi)^2 \right) \mathrm{d}V \,, \tag{2.9}$$

with

$$\begin{aligned}\kappa &\equiv 2\kappa_3 - 2\frac{\mathrm{d}\kappa_2}{\mathrm{d}\phi} \\ &= \left.\frac{\partial^2 f}{\partial(\nabla\phi)^2}\right|_0 - 2\left.\frac{\partial^2 f}{\partial\phi\partial\nabla^2\phi}\right|_0 . \end{aligned} \tag{2.10}$$

The function $f_0(\phi)$ is typically chosen as a double-well function with minima corresponding to the value of ϕ taken in the two different phases (e.g. 0 and 1). Note that it is not necessary, however, for the minima to be located at $\phi = 0$ and $\phi = 1$ — one could just as well choose $\phi = -1$ and $\phi = 1$ to be the minima, and indeed this is a popular choice in the literature. The underlying physics of the system is recovered in both cases.

2.3 Free energy of a homogeneous system

Regular Solution Theory

Considering pairwise interactions only, the internal energy, U, of a binary alloy consisting of N_A atoms of type A and N_B atoms of type B may be expressed as

$$U = -\epsilon_{AA}N_{AA} - \epsilon_{BB}N_{BB} - \epsilon_{AB}N_{AB}\,, \tag{2.11}$$

where $-\epsilon_{AA}$, $-\epsilon_{BB}$ and $-\epsilon_{AB}$ are the interaction energies between A-A, B-B and A-B pairs respectively, and where N_{AA}, N_{BB} and N_{AB} are the number of A-A, B-B and A-B nearest-neighbour pairs respectively.

Now, for a randomly ordered configuration of the alloy, the probability of a given site being occupied by either an A or B atom is given by the total fraction of A and B atoms respectively. If we denote by

$$c_A \equiv c = \frac{N_A}{N} \tag{2.12}$$

and

$$c_B \equiv 1 - c = \frac{N_B}{N}\,, \tag{2.13}$$

the fractions of A and B atoms respectively, with $N \equiv N_A + N_B$ being the total number of atoms, then the number of pairs of each type are given by [47]

$$\begin{aligned} N_{AA} &= \frac{Nzc^2}{2} \\ N_{BB} &= \frac{Nz(1-c)^2}{2} \\ N_{AB} &= Nzc(1-c)\,, \end{aligned} \tag{2.14}$$

where z is the coordination number. Hence, substituting the above into equation (2.11), we find

$$\begin{aligned} U &= -\epsilon_{AA}\frac{Nzc^2}{2} - \epsilon_{BB}\frac{Nz(1-c)^2}{2} - \epsilon_{AB}Nzc(1-c) \\ &= -\frac{Nz}{2}\Big(\epsilon_{AA}c^2 + \epsilon_{BB}(1-c)^2 + 2\epsilon_{AB}c(1-c)\Big) \\ &= -\frac{Nz}{2}\Big(\epsilon_{AA}c + \epsilon_{BB}(1-c) + 2c(1-c)\epsilon\Big)\,, \end{aligned} \tag{2.15}$$

where

$$\epsilon \equiv \epsilon_{AB} - \frac{\epsilon_{AA}+\epsilon_{BB}}{2}\,. \tag{2.16}$$

Let us now consider the entropy, S, given by

$$S = k_B \ln W\,, \tag{2.17}$$

where k_B is Boltzmann's constant and W is the number of possible microstates (ways of arranging the A and B atoms) for a given macrostate (total number of atoms) of the system, and is given by

$$W = \frac{N!}{N_A!N_B!} = \frac{N!}{(Nc)!\big[N(1-c)\big]!}\,. \tag{2.18}$$

Substituting into equation (2.17) and using Stirling's approximation, we obtain

$$\begin{aligned} S &\approx k_B\Big\{N\ln N - N - \Big(Nc\ln(Nc) + N(1-c)\ln\big(N(1-c)\big) - N(1-c)\Big)\Big\} \\ &= -Nk_B\big(c\ln c + (1-c)\ln(1-c)\big)\,. \end{aligned} \tag{2.19}$$

Assuming that the pressure is zero, so that the Gibbs free energy, $F = A + pV$, is equal to the Helmholtz free energy, $A = U - TS$, where T is the temperature, we obtain

$$\begin{aligned} F = U - TS &= -\frac{Nz}{2}\Big(\epsilon_{AA}c + \epsilon_{BB}(1-c) + 2c(1-c)\epsilon\Big) \\ &\quad + Nk_BT\Big(c\ln c + (1-c)\ln(1-c)\Big) \\ &= cF_A + (1-c)F_B - Nz\epsilon c(1-c) \\ &\quad + Nk_BT\Big(c\ln c + (1-c)\ln(1-c)\Big)\,, \end{aligned} \tag{2.20}$$

where $F_A = -Nz\epsilon_{AA}c/2$ and $F_B = -Nz\epsilon_{AA}(1-c)/2$ are the free energies of the pure A and B components of the system [47]. The term $-Nz\epsilon$ is usually called the *regular solution parameter*, Ω, so that

$$\begin{aligned} F &= cF_A + (1-c)F_B + \Omega c(1-c) \\ &\quad + Nk_BT\Big(c\ln c + (1-c)\ln(1-c)\Big)\,. \end{aligned} \tag{2.21}$$

Note that if Ω is negative, then the free energy function has only one minimum, located at $c = 0.5$, and the system is completely miscible regardless of the temperature. If, on the other hand, the regular solution parameter is positive, then there is a trade-off between the entropic and energetic contributions to the free energy. In this case, a *critical temperature*, $T = T_c$, exists. Above the critical temperature, there is only one minimum of the free energy, and the system exists as a mixture of the two components. As the temperature is lowered to below T_c, however, the free energy exhibits two minima. As a result, the system undergoes phase separation into two demixed phases which are rich in each component. This phenomenon is known as *spinodal decomposition* and is discussed further in section 2.4.2.

Polynomial form

Polynomial forms for the free energy typically take the form of a double-well potential and are used as an approximation to physical models such as the regular solution model. An example is

$$f(\phi) = \frac{\phi^4}{4} - \frac{\phi^2}{2}\,. \tag{2.22}$$

The minima are then located at $\phi = 1$ and $\phi = -1$ (see figure 2.1). A similar polynomial form, with minima at $\phi = 0$ and $\phi = 1$, is given by

$$f(\phi) = \phi^2(1 - \phi^2)^2\,. \tag{2.23}$$

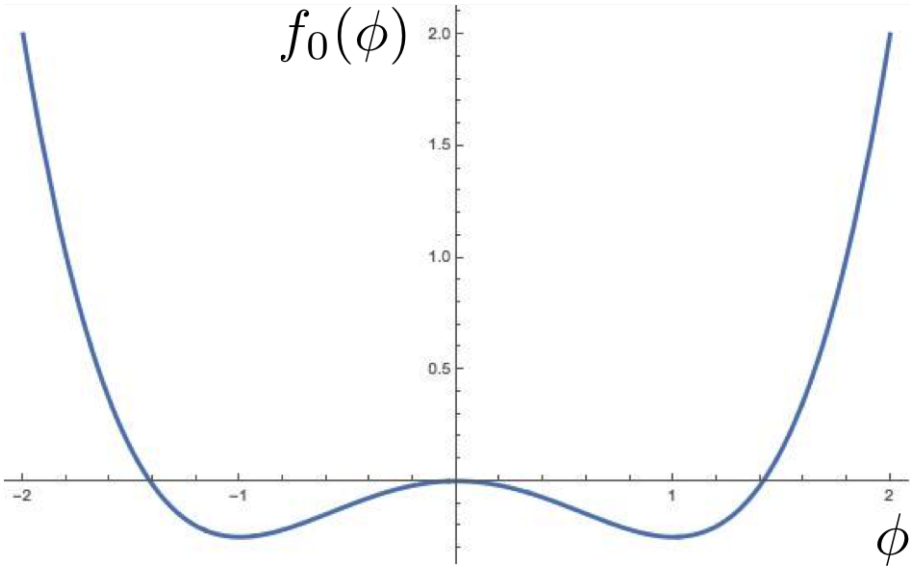


Figure 2.1: Double-well form of the free energy, given by equation (2.22).

2.4 Cahn-Hilliard equation

If a conserved quantity (e.g. composition) is chosen to be the order parameter, then ϕ must obey a continuity equation. Hence,

$$\frac{\partial \phi}{\partial t} = -\nabla \cdot \vec{J}, \tag{2.24}$$

where the flux, $\vec{J}$, is given by Fick's first law

$$\vec{J} = -M \nabla \mu \,. \tag{2.25}$$

Here, M is the solute mobility and μ is the chemical potential, which is defined as the variational derivative of F with respect to ϕ [45]

$$\mu = \frac{\delta F}{\delta \phi}\,. \tag{2.26}$$

Combining equations (2.24), (2.25) and (2.26), we obtain

$$\frac{\partial \phi}{\partial t} = \nabla \cdot \left(M \nabla \frac{\delta F}{\delta \phi} \right), \tag{2.27}$$

where the variational derivative of the free energy (equation (2.9)) is given by

$$\frac{\delta F}{\delta \phi} = \frac{\partial f_0(\phi)}{\partial \phi} - \kappa \nabla^2 \phi\,, \tag{2.28}$$

and therefore

$$\frac{\partial \phi}{\partial t} = \nabla \cdot \left[M \nabla \left(\frac{\partial f_0(\phi)}{\partial \phi} - \kappa \nabla^2 \phi \right) \right]. \tag{2.29}$$

Equation (2.29) is the general form of the Cahn-Hilliard equation, with the specific form being dependent upon the choice of $f_0(\phi)$.

Gradient Energy Term

Consider the gradient energy term, $\kappa \nabla^2 \phi$, and let us assume that the bulk free energy is given by

$$f_0(\phi) = \frac{\phi^4}{4} - \frac{\phi^2}{2}\,. \tag{2.30}$$

Without the gradient energy term, the equilibrium constraint that $\frac{\delta F}{\delta \phi} = 0$ implies that $\phi^3 - \phi = 0$. Thus, we find that $\phi = -1$ or $\phi = 1$. On the other

hand, if we include the gradient energy term, then in one dimension, we have

$$\kappa \frac{\partial^2 \phi}{\partial x^2} - \frac{\partial f_0(\phi)}{\partial \phi} = 0\,. \tag{2.31}$$

Multiplying both sides by $\frac{\partial \phi}{\partial x}$, and integrating from $-\infty$ to a position x, we obtain [45]

$$\begin{aligned} 0 &= \kappa \int_{-\infty}^{x} \frac{\partial^2 \phi}{\partial x'^2} \frac{\partial \phi}{\partial x'}\, \mathrm{d}x' - \int_{-\infty}^{x} \frac{\partial f_0(\phi)}{\partial \phi} \frac{\partial \phi}{\partial x'}\, \mathrm{d}x' \\ &= \frac{\kappa}{2} \int_{-\infty}^{x} \frac{\partial}{\partial x'} \left(\frac{\partial \phi}{\partial x'} \right)^2 \mathrm{d}x' - \big(f_0(\phi(x)) - f_0(\phi(-\infty)) \big) \\ &= \frac{\kappa}{2} \left(\frac{\partial \phi}{\partial x} \right)^2 - f_0(\phi(x)) + f_0(\phi(-\infty))\,, \end{aligned} \tag{2.32}$$

where $\phi(-\infty) = -1$. On substitution of equation (2.30) for $f_0(\phi)$, we find that

$$\frac{\kappa}{2} \left(\frac{\mathrm{d}\phi}{\mathrm{d}x} \right)^2 = \frac{\phi^4}{4} - \frac{\phi^2}{2} + \frac{1}{4}\,, \tag{2.33}$$

and hence

$$\begin{aligned} \frac{\mathrm{d}\phi}{\mathrm{d}x} &= \sqrt{\frac{2}{\kappa}} \sqrt{\frac{\phi^4}{4} - \frac{\phi^2}{2} + \frac{1}{4}} \\ &= \frac{1}{\sqrt{2\kappa}} \sqrt{\phi^4 - 2\phi^2 + 1} \\ &= \frac{1}{\sqrt{2\kappa}} \sqrt{(\phi^2 - 1)^2} \\ &= \pm \frac{\phi^2 - 1}{\sqrt{2\kappa}}\,. \end{aligned} \tag{2.34}$$

In order to solve this equation, we separate the terms and integrate:

$$\pm \int \frac{\mathrm{d}\phi}{1-\phi^2} = \int \frac{\mathrm{d}x}{\sqrt{2\kappa}}\,, \tag{2.35}$$

which gives

$$\mp \tanh^{-1}(\phi) = \frac{x}{\sqrt{2\kappa}}\,, \tag{2.36}$$

or

$$\phi_{\mathrm{eq}} = \pm \tanh\left(\frac{x}{\sqrt{2\kappa}}\right), \tag{2.37}$$

where ϕ_{eq} denotes the equilibrium profile (the subscript has been omitted above). Thus, the gradient energy term, $\kappa\nabla^2\phi$, leads to diffuse interfaces, as shown in figure 2.2, with a characteristic interfacial width given by $\sqrt{2\kappa}$.

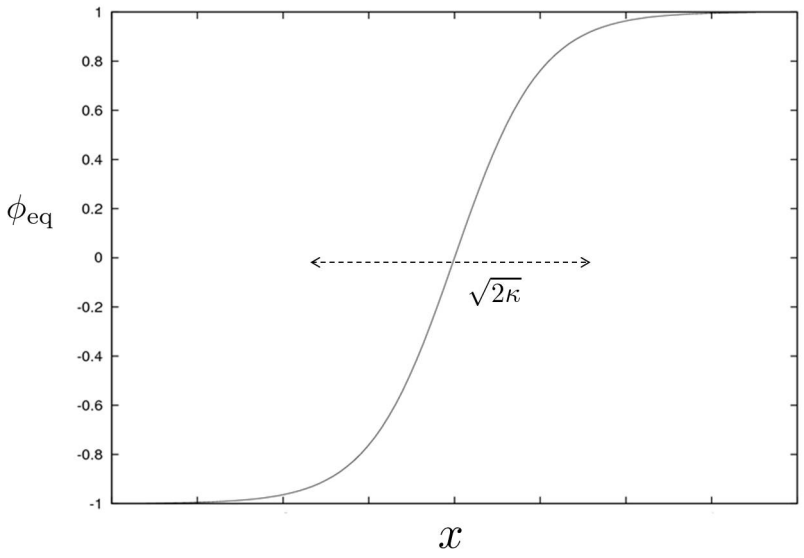


Figure 2.2: Diffuse interface with hyperbolic tangent profile.

2.4.1 Interfacial energy

The interfacial energy, σ, of a flat 1D interface, in the Cahn-Hilliard model is given by [32, 48]

$$\sigma = \int_{-\infty}^{\infty} \left[\Delta f(\phi) + \kappa \left(\frac{\mathrm{d}\phi}{\mathrm{d}x} \right)^2 \right] \mathrm{d}x \,, \tag{2.38}$$

where

$$\Delta f(\phi) = f_0(\phi) - \Big[\phi \mu_B + (1-\phi)\mu_A \Big] \,, \tag{2.39}$$

and μ_A and μ_B are the chemical potentials of species A and B in the A and B phases respectively:

$$\mu_A = \left. \frac{\partial f_0}{\partial \phi} \right|_A \,, \qquad \mu_B = \left. \frac{\partial f_0}{\partial \phi} \right|_B \,. \tag{2.40}$$

For the specific case of the homogeneous free energy being given by the regular solution theory, we have [32]

$$\begin{aligned} \Delta f(\phi) &= -\Omega(\phi - \phi_e)^2 \\ &\quad + k_B T \left\{ \phi \ln(\phi/\phi_e) + (1-\phi) \ln\left(\frac{1-\phi}{1-\phi_e} \right) \right\} , \end{aligned} \tag{2.41}$$

where ϕ_e can be either of the equlibrium compositions given by the regular solution model.

2.4.2 Spinodal Decomposition

Spinodal decomposition is the process whereby a homogeneous mixture of two components undergoes spontaneous phase separation to form two stable phases. Consider an initially homogeneous binary mixture of composition ϕ_0, and let us apply a one-dimensional sinusoidal fluctuation, so that [31]

$$\phi - \phi_0 = A\cos\left(\frac{2\pi x}{\lambda}\right) \equiv A\cos(\beta x)\,, \tag{2.42}$$

where $\beta \equiv 2\pi/\lambda$, A is the amplitude and λ is the wavelength of the fluctuation. Assuming the compositional fluctuation to be sufficiently small, we may expand the free energy density, $f(\phi)$, in a Taylor series, about ϕ_0:

$$f(\phi) = f(\phi_0) + \left.\frac{\partial f}{\partial \phi}\right|_{\phi=\phi_0}(\phi-\phi_0) + \frac{1}{2}\left.\frac{\partial^2 f}{\partial \phi^2}\right|_{\phi=\phi_0}(\phi-\phi_0)^2 + \cdots \tag{2.43}$$

The free energy of the mixture,

$$F = \int \left\{ f(\phi) + \frac{\kappa}{2}(\nabla\phi)^2 \right\} \mathrm{d}V\,, \tag{2.44}$$

may then be written as

$$\frac{F}{\Gamma} = \int \left\{ f(\phi_0) + \left.\frac{\partial f}{\partial \phi}\right|_{\phi=\phi_0}(\phi-\phi_0) + \frac{1}{2}\left.\frac{\partial^2 f}{\partial \phi^2}\right|_{\phi=\phi_0}(\phi-\phi_0)^2 + \frac{\kappa}{2}\left(\frac{\partial\phi}{\partial x}\right)^2 \right\} \mathrm{d}x\,, \tag{2.45}$$

where Γ is the area of the system. Hence, the free energy density is

$$\begin{aligned} f(\phi) &= \frac{1}{\lambda}\int_0^\lambda \left\{ f(\phi_0) + A\cos\left(\frac{2\pi x}{\lambda}\right)\left.\frac{\partial f}{\partial \phi}\right|_{\phi=\phi_0} \right. \\ &\quad + \frac{1}{2}A^2\cos^2\left(\frac{2\pi x}{\lambda}\right)\left.\frac{\partial^2 f}{\partial \phi^2}\right|_{\phi=\phi_0} \\ &\quad \left. + \frac{4\pi^2}{\lambda^2}\kappa A^2 \sin^2\left(\frac{2\pi x}{\lambda}\right)\right\} \mathrm{d}x\,. \end{aligned} \tag{2.46}$$

Let us now consider each term in the integral separately:

$$\frac{1}{\lambda}\int_0^\lambda f(\phi_0)\mathrm{d}x = f(\phi_0) \tag{2.47}$$

$$\left.\frac{\partial f}{\partial \phi}\right|_{\phi=\phi_0}\frac{A}{\lambda}\int_0^\lambda \cos\left(\frac{2\pi x}{\lambda}\right)\mathrm{d}x = \left.\frac{\partial f}{\partial \phi}\right|_{\phi=\phi_0}\frac{A}{\lambda}\left[\sin\left(\frac{2\pi x}{\lambda}\right)\frac{\lambda}{2\pi}\right]_0^\lambda = 0 \tag{2.48}$$

$$\begin{aligned} \left.\frac{\partial^2 f}{\partial \phi^2}\right|_{\phi=\phi_0}\frac{A^2}{2\lambda}\int_0^\lambda \cos^2\left(\frac{2\pi x}{\lambda}\right)\mathrm{d}x &= \left.\frac{\partial^2 f}{\partial \phi^2}\right|_{\phi=\phi_0}\frac{A^2}{4\lambda}\left[\sin\left(\frac{4\pi x}{\lambda}\right)\frac{\lambda}{4\pi} + x\right]_0^\lambda \\ &= \left.\frac{\partial^2 f}{\partial \phi^2}\right|_{\phi=\phi_0}\frac{A^2}{4} \end{aligned} \tag{2.49}$$

$$\begin{aligned} \frac{1}{\lambda}\frac{4\pi^2}{\lambda^2}\frac{\kappa}{2}A^2\int_0^\lambda \sin^2\left(\frac{2\pi x}{\lambda}\right)\mathrm{d}x &= \frac{\pi^2}{\lambda^3}\kappa A^2\int_0^\lambda\left(1-\cos\left(\frac{4\pi x}{\lambda}\right)\right)\mathrm{d}x \\ &= \frac{\pi^2}{\lambda^3}\kappa A^2\left[x - \sin\left(\frac{4\pi x}{\lambda}\right)\frac{\lambda}{4\pi}\right]_0^\lambda \\ &= \frac{\pi^2}{\lambda^2}\kappa A^2 \end{aligned} \tag{2.50}$$

Hence, the change in the free energy density upon applying the sinusoidal fluctuation given by equation (2.42), is

$$\Delta f = \frac{A^2}{4}\left[\frac{\partial^2 f}{\partial \phi^2} + \kappa\beta^2\right]. \tag{2.51}$$

Since κ is positive, Δf is positive if the second derivative, f'', is positive, in which case the homogeneous mixture is stable with respect to such fluctuations, and phase separation is not energetically favourable. On the other hand, when f'' is negative, Δf is negative when β is less than the critical wavenumber β_c,

$$\beta_c = \sqrt{\frac{|f''|}{\kappa}}, \tag{2.52}$$

through which we may define the critical wavelength, λ_c, as

$$\lambda_c = \sqrt{\frac{4\pi^2\kappa}{|f''|}}, \tag{2.53}$$

such that the mixture is unstable to any fluctuation of wavelength $\lambda > \lambda_c$.

Figure 2.3 shows a series of snapshots from a numerical simulation of the Cahn-Hilliard equation in 2D. The simulation is started with a homogeneous mixture of two components with equal compositions. A random fluctuation is then applied, and the system is allowed to evolve. During the initial stages, we see the process of spinodal decomposition and phase separation. Domain coarsening is seen in the latter stages.

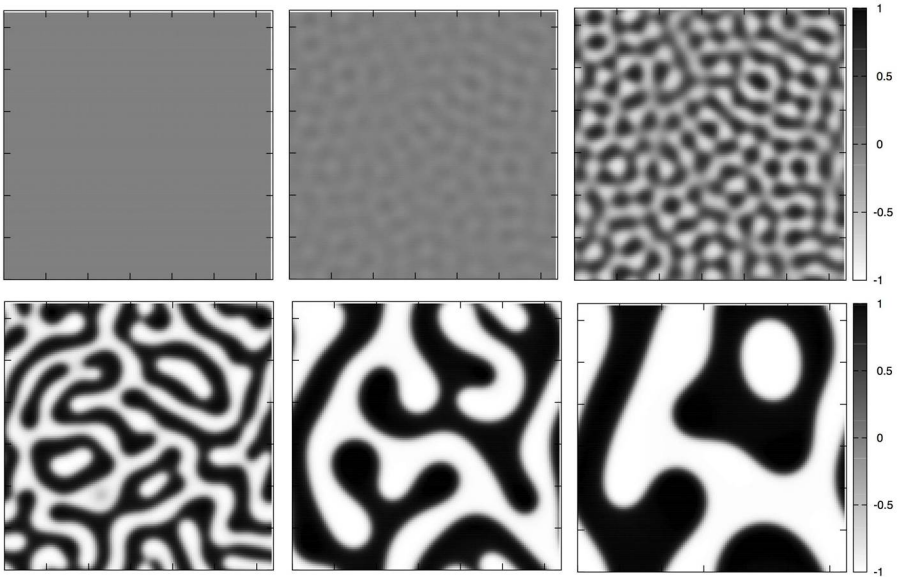


Figure 2.3: Numerical solution of Cahn-Hilliard equation, showing the process of spinodal decomposition.

2.4.3 Ostwald Ripening

If, instead of starting the solution of the Cahn-Hilliard equation at $\phi_0 = 0.5$, we start at a composition of $\phi_0 = 0.25$, the second derivative of the free energy, f'', is less than zero, and we see nucleation of the minority phase inside a matrix of the other phase, as in figure 2.4. However, since the free energy increases due to the increasing interfacial area, small nuclei tend to shrink and diffuse into the larger nuclei, so that the larger nuclei coarsen over time, in order to reduce the total interfacial area. This process is known as *Ostwald ripening*, after the German chemist, Wilhelm Ostwald [49].

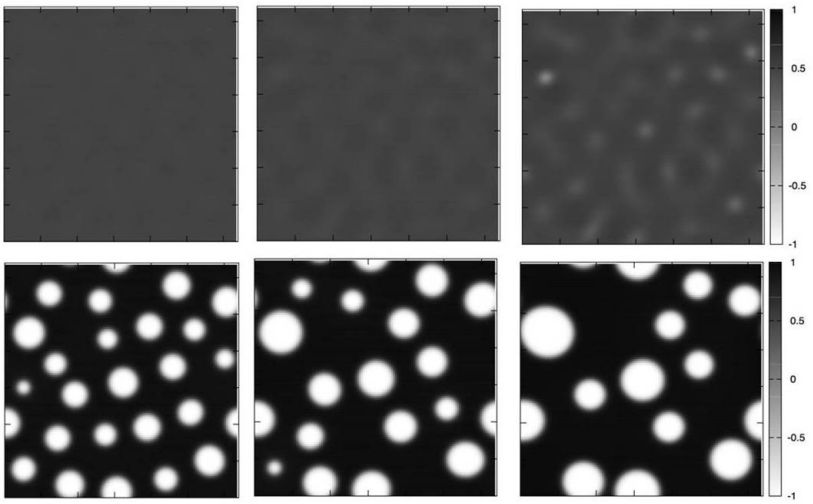


Figure 2.4: Numerical solution of Cahn-Hilliard equation, showing the process of Ostwald ripening.

2.5 Allen-Cahn equation

If we consider a non-conserved order parameter, ϕ, the continuity equation (equation (2.24)) is no longer satisfied, and we may instead write [45]

$$\begin{aligned} \frac{\partial \phi}{\partial t} &= -M \frac{\delta F}{\delta \phi} \\ &= M\left(\kappa \nabla^2 \phi - \frac{\partial f_0}{\partial \phi}\right). \end{aligned} \tag{2.54}$$

Equation (2.54) is the Allen-Cahn equation, and is also referred to as the time-dependent Ginzburg-Landau equation.

Chapter 3

MULTICOMPONENT SYSTEMS

3.1 Multiple order parameter phase-field models

Chen and Khachaturyan [50] were the first to use multiple order parameters to describe solid-state phase transformations. In their approach, the order parameters were used to describe the many possible phases of a single-component system, and the free energy functional for a system consisting of N phases, each of which is represented by an order parameter ϕ_i, is given by [45]

$$F[\{\phi_i\}] = \int_V \mathrm{d}V \left[f(\{\phi_i\}) + \sum_{i=1}^{N} \frac{\zeta_i^2}{2} |\nabla \phi_i|^2 \right], \tag{3.1}$$

where $\{\phi_i\}$ represents the set of all ϕ_i, ζ_i is a gradient energy coefficient and $f(\{\phi_i\})$ is the bulk free energy, which typically takes the form of a multi-well potential. A simple extension of the Allen-Cahn equation (equation (2.54)) for non-conserved order parameter fields, then gives us the following set of

equations which govern the dynamics of multiphase systems:

$$\frac{\partial \phi_i}{\partial t} = -M_i \left(\frac{\partial f(\{\phi_i\})}{\partial \phi_i} - \zeta_i^2 \nabla^2 \phi_i \right). \tag{3.2}$$

Wheeler, Boettinger and McFadden (WBM) [42] [51] developed a similar phase-field model to that of Khachaturyan et al., which is capable of simulating phase transitions in a two-component, two-phase system. The WBM free energy functional is given by

$$F[\{\phi_i\}, c] = \int_V \mathrm{d}V \left[f(\phi, c) + \frac{\zeta^2}{2} |\nabla \phi|^2 + \frac{\kappa^2}{2} |\nabla c|^2 \right], \tag{3.3}$$

where κ is the compositional gradient energy coefficient and c is the composition of one component, with the other component having composition $1-c$. $\phi = 0$ in the liquid phase and $\phi = 1$ in the solid phase. The bulk free energy, $f(\phi, c)$ used by Wheeler et al. is that of an ideal solution,

$$f(\phi, c) = c f_B(\phi) + (1-c) f_A(\phi) + k_B T \big[c \log c + (1-c) \log(1-c) \big], \tag{3.4}$$

where $f_A(\phi)$ and $f_B(\phi)$ are the free energy densities of pure A and B, and are represented by double-well functions with respect to the phase-field order parameter, ϕ. The system is then governed by an Allen-Cahn equation for the non-conserved order parameter, ϕ,

$$\frac{\partial \phi}{\partial t} = -M_1 \left(\frac{\partial f}{\partial \phi} - \zeta^2 \nabla^2 \phi \right), \tag{3.5}$$

and a Cahn-Hilliard type equation for the composition,

$$\frac{\partial c}{\partial t} = \nabla \cdot M_2 \left[c(1-c) \nabla \left(\frac{\partial f}{\partial c} - \kappa^2 \nabla^2 c \right) \right] . \tag{3.6}$$

Steinbach et al. [52], introduced the *multiphase-field method*, which is capable of treating an arbitrary number of phases. Each of the N phases is represented by a non-conserved volume fraction, ϕ_α, and hence, the system must obey the constraint,

$$\sum_{\alpha=1}^{N} \phi_\alpha = 1 \, , \tag{3.7}$$

or, equivalently

$$\sum_{\alpha=1}^{N} \frac{\partial \phi_\alpha}{\partial t} = 0 \, . \tag{3.8}$$

In order to account for the constraint on the volume fraction, the following term is added to the free energy functional [45]:

$$\int_V \mathrm{d}V \, \lambda \left(\sum_{\alpha=1}^{N} \phi_\alpha - 1 \right) , \tag{3.9}$$

where λ is an undetermined Lagrange multiplier.

3.2 Multicomponent Cahn-Hilliard equations

In the previous section, we have described some of the commonly used methods for treating multiple order parameters in the context of phase-field theory. However, the methods described are only suitable for the treatment of multiple *non-conserved* order parameters. We have therefore chosen to use the ternary Cahn-Hilliard system of equations to model the process of phase sep-

aration in bimetallic nanoparticles, with the three components in our ternary system corresponding to the two metallic components plus vacuum. To each component, i, corresponds an order parameter, ϕ_i, which represents the local composition of that component. The decision to have a ternary sytem is motivated by the fact that it removes the requirement to enforce boundary conditions on the surfaces of the particles. The shape of the particles is thus determined by the thermodynamics of the system, via the processes of spinodal decompositon and coarsening. The Cahn-Hilliard system has been chosen since the order parameters in our system are conserved. Moreover, it is the only phase-field method that is capable of modelling spinodal decomposition.

For a system composed of N components, let us define a set of order parameters, $\{\phi_i(\mathbf{x})\}$, corresponding to the local fraction of component i ($i = 1 \cdots N$) at point $\mathbf{x}$. Conservation of mass then implies that

$$\sum_{i=1}^{N} \phi_i(\mathbf{x}, t) = 1\,. \tag{3.10}$$

Thus, $N-1$ of the $\{\phi_i\}$ are independent. Analogously to equation (2.9), the free energy of a multicomponent system may be written, as [53, 54]

$$F = \int_V \left\{ f_0(\{\phi_i(\mathbf{x}, t)\}) + \sum_{i,j=1}^{N-1} \frac{\kappa_{ij}}{2} \nabla\phi_i \cdot \nabla\phi_j \right\} \mathrm{d}V\,, \tag{3.11}$$

where ζ_{ij} are the gradient energy coefficients. The flux of component i is

$$\mathbf{J}_i = -\sum_j M_{ij} \nabla \frac{\delta F}{\delta \phi_j}\,, \tag{3.12}$$

and the general form of the multicomponent Cahn-Hilliard equations is thus

$$\frac{\partial \phi_i}{\partial t} = \nabla \cdot \left(\sum_j M_{ij} \nabla \frac{\delta F}{\delta \phi_j} \right), \tag{3.13}$$

where the variational derivative is dependent on the specific form of the bulk free energy, f_0, which we are yet to define, and where M_{ij} are mobilities.

3.2.1 Ternary Cahn-Hilliard equations

Expanding equation (3.13) for a ternary system, we obtain the following set of coupled Cahn-Hilliard equations:

$$\begin{aligned}
\frac{\partial \phi_1}{\partial t} &= M_{11}\left[\nabla^2\left(\frac{\partial f_0}{\partial \phi_1} - \zeta_{11}\nabla^2\phi_1 - \frac{1}{2}(\zeta_{12}+\zeta_{21})\nabla^2\phi_2\right)\right] \\
&\quad + M_{12}\left[\nabla^2\left(\frac{\partial f_0}{\partial \phi_2} - \zeta_{22}\nabla^2\phi_2 - \frac{1}{2}(\zeta_{12}+\zeta_{21})\nabla^2\phi_1\right)\right] \\
\frac{\partial \phi_2}{\partial t} &= M_{21}\left[\nabla^2\left(\frac{\partial f_0}{\partial \phi_1} - \zeta_{11}\nabla^2\phi_1 - \frac{1}{2}(\zeta_{12}+\zeta_{21})\nabla^2\phi_2\right)\right] \\
&\quad + M_{22}\left[\nabla^2\left(\frac{\partial f_0}{\partial \phi_2} - \zeta_{22}\nabla^2\phi_2 - \frac{1}{2}(\zeta_{12}+\zeta_{21})\nabla^2\phi_1\right)\right].
\end{aligned} \tag{3.14}$$

From the Taylor expansion of the free energy for the ternary case, we obtain a 3×3 matrix of coefficients, k_{ij},

$$\begin{pmatrix} k_{11} & k_{12} & k_{13} \\ k_{21} & k_{22} & k_{23} \\ k_{31} & k_{32} & k_{33} \end{pmatrix} . \tag{3.15}$$

However, since only two of the ϕ_i are independent, we have the following gradient energy coefficients, ζ_{ij}, in our system:

$$\begin{pmatrix} \zeta_{11} & \zeta_{12} \\ \zeta_{21} & \zeta_{22} \end{pmatrix} , \tag{3.16}$$

where the relation between the two sets of coefficients is given by

$$\begin{aligned} \zeta_{11} &= k_{11} - 2k_{13} + k_{33} \\ \zeta_{12} &= k_{12} - k_{13} - k_{23} + k_{33} \\ \zeta_{22} &= k_{22} - 2k_{23} + k_{33} \, . \end{aligned} \tag{3.17}$$

We now note that the system must reduce to the two-component Cahn-Hilliard model in the absence of one of the phases. Hence, the ζ_{ij} are related

to the gradient energy coefficients in the binary Cahn-Hilliard model, κ_{ij}, by

$$\begin{aligned}
\kappa_{13} &= k_{11} - 2k_{13} + k_{33} = \zeta_{11} \\
\kappa_{23} &= k_{22} - 2k_{23} + k_{33} = \zeta_{22} \\
\kappa_{13} &= k_{11} - 2k_{12} + k_{22} = \kappa_{13} + \kappa_{23} - 2\zeta_{12}\,, \qquad (3.18)
\end{aligned}$$

and therefore

$$\zeta_{12} = \frac{1}{2}(\kappa_{13} + \kappa_{23} - \kappa_{12})\,. \qquad (3.19)$$

3.2.2 Ternary regular solution

Let us proceed to write down an explicit form for the bulk free energy, $f_0(\phi_1, \phi_2)$, of the ternary system:

$$\begin{aligned}
f_0 &= \sum_{i=1}^{3} \Big(\phi_i f_i^0 + \phi_i \log \phi_i \Big) + \sum_{i \neq j} \Omega_{ij} \phi_i \phi_j \\
&= \phi_1 f_1^0 + \phi_2 f_2^0 + \phi_3 f_3^0 + \phi_1 \log \phi_1 + \phi_2 \log \phi_2 + \phi_3 \log \phi_3 \\
&\quad + \Omega_{12}\phi_1\phi_2 + \Omega_{13}\phi_1\phi_3 + \Omega_{23}\phi_2\phi_3\,, \qquad (3.20)
\end{aligned}$$

where the Ω_{ij} are the binary regular solution parameters, and are related to the gradient energy coefficients via [32]

$$\kappa_{ij} = \Omega_{ij} a^2\,, \qquad (3.21)$$

where a is an interaction length, typically taken to be the interatomic distance. In general, there is a term of the form $\Omega_{123}\phi_1\phi_2\phi_3$ in equation (3.20); however, we neglect this, since the ternary regular solution parameter, Ω_{123}, is usually small.

Figure 3.1 shows a plot of the free energy, given by equation (3.20), as a function of composition, with all Ω_{ij} being equal. Figure 3.2 shows a series of snapshots from a numerical solution of the ternary Cahn-Hilliard equations, with the free energy given by the ternary regular solution model, and with $\Omega_{ij} = 3.5$ in reduced units, for all i, j. The initial conditions are $\phi_1 = \phi_2 = \phi_3 = 1/3$, so that we have an equal mixture of all three components. A random fluctuation is then added, and the system undergoes phase separation.

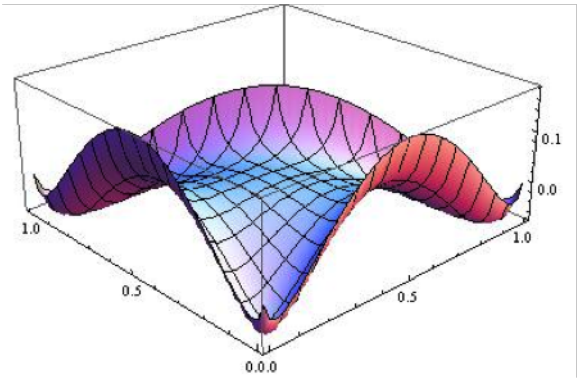


Figure 3.1: Plot of the free energy of a ternary regular solution. In this case, all Ω_{ij} are equal. The height represents the energy, while the other two axes represent the composition of two of the components.

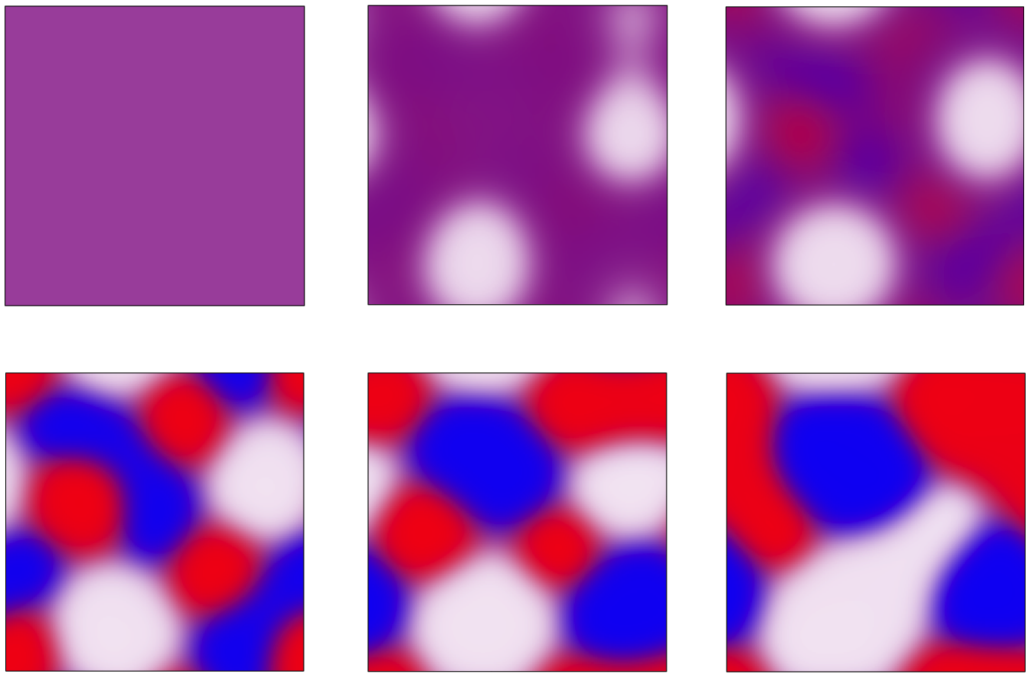


Figure 3.2: Numerical solution of the ternary Cahn-Hilliard equations, with the bulk free energy given by the ternary regular solution model; red, blue and white represent the three components.

3.2.3 Interfacial energy for a ternary system

Consider the three minimum points, P, Q and R, of the free energy (equation (3.1)) of a ternary system. The coordinates of these three minima are given by

$$P = (\phi_A^1, \phi_B^1, h^1) \tag{3.22}$$

$$Q = (\phi_A^2, \phi_B^2, h^2) \tag{3.23}$$

$$R = (\phi_A^3, \phi_B^3, h^3)\,, \tag{3.24}$$

where ϕ_A^i and ϕ_B^i $(i = 1, 2, 3)$ are the fractions of components A and B at each of the three minima, and where h^i is the height of the i^{th} minimum point (i.e. the value of the free energy at the i^{th} minimum). Let us now consider the plane connecting the three minima. The vectors $\vec{PQ}$ and $\vec{PR}$, which lie in the plane, are then

$$\begin{aligned} \vec{PQ} &= (\phi_A^2 - \phi_A^1)\hat{\mathbf{x}} + (\phi_B^2 - \phi_B^1)\hat{\mathbf{y}} + (h^2 - h^1)\hat{\mathbf{z}} && (3.25) \\ \vec{PR} &= (\phi_A^3 - \phi_A^1)\hat{\mathbf{x}} + (\phi_B^3 - \phi_B^1)\hat{\mathbf{y}} + (h^3 - h^1)\hat{\mathbf{z}}\,. && (3.26) \end{aligned}$$

Taking the cross product of $\vec{PQ}$ and $\vec{PR}$ gives us a vector that is orthogonal to the plane,

$$a\hat{\mathbf{x}} + b\hat{\mathbf{y}} + c\hat{\mathbf{z}}\,, \tag{3.27}$$

and the equation of the plane is thus

$$a(\phi_A - \phi_A^{\text{eq}}) + b(\phi_B - \phi_B^{\text{eq}}) + c(h - h^{\text{eq}}) = 0\,, \tag{3.28}$$

where $(\phi_A^{\text{eq}}, \phi_B^{\text{eq}})$ may be chosen to correspond to any one of the three minima, and where

$$\begin{aligned} a &= (\phi_B^2 - \phi_B^1)(h^3 - h^1) - (h^2 - h^1)(\phi_B^3 - \phi_B^1) \\ b &= (h^2 - h^1)(\phi_A^3 - \phi_A^1) - (\phi_A^2 - \phi_A^1)(h^3 - h^1) \\ c &= (\phi_A^2 - \phi_A^1)(\phi_B^3 - \phi_B^1) - (\phi_B^2 - \phi_B^1)(\phi_A^3 - \phi_A^1)\,. && (3.29) \end{aligned}$$

If we define d, such that

$$d = a\phi_A^{\mathrm{eq}} + b\phi_B^{\mathrm{eq}} + ch^{\mathrm{eq}}\,, \tag{3.30}$$

then

$$h^{\mathrm{eq}} = \frac{d - (a\phi_A^{\mathrm{eq}} + b\phi_B^{\mathrm{eq}})}{c}\,, \tag{3.31}$$

and $\Delta f(\phi_A, \phi_B)$ is given by

$$\Delta f(\phi_A, \phi_B) = f_0(\phi_A, \phi_B) - h^{\mathrm{eq}}(\phi_A, \phi_B)\,. \tag{3.32}$$

Analogously to equation (2.38), the contribution to the interfacial energy from the interface between components i and j is then

$$\sigma_{ij} = \int \left[\Delta f + \kappa_{ij}\nabla\phi_i\nabla\phi_j\right] \mathrm{d}\mathbf{x}\,. \tag{3.33}$$

Chapter 4

NUMERICAL METHODS FOR PHASE-FIELD EQUATIONS

The most widely used numerical method for solving phase-field equations is the explicit finite difference method. This is mainly due to the simplicity of the method and the relative ease with which it may be implemented. The Cahn-Hilliard equation, however, contains a fourth-order derivative term which renders the equation *stiff*. This means that the fourth-order term induces rapid variations in the solution which, in turn, require the use of prohibitively small time steps in order to guarantee numerical stability.

It is well known that the explicit finite difference method is susceptible to the stiffness in the Cahn-Hilliard equation, and it may be shown that the method is only numerically stable if the time step, Δt, satisfies the relation [45]

$$\Delta t \leq \frac{(\Delta x)^4}{32}\,, \tag{4.1}$$

where Δx is the grid spacing. This clearly poses severe problems for small Δx, and requires the use of extremely small Δt. The use of the explicit finite difference method is therefore not a particularly wise choice for solving the Cahn-Hilliard equation.

It is possible, through the use of implicit methods, to alleviate some of the constraints on the step size when solving the Cahn-Hilliard equation. Implicit methods, however, carry a significant disadvantage in that they require the solution of a linear system of equations at each time step. In this respect, a direct matrix inversion requires $\mathcal{O}(n^6)$ operations at each time step, while iterative methods require $\mathcal{O}(n^3)$ – $\mathcal{O}(n^4)$ operations (n is the size of the system).

Spectral methods have, in recent years, become a popular choice for the numerical solution of PDEs such as the Navier-Stokes equations. The advantage of spectral methods is that we may convert a PDE in real space into an ODE in Fourier space. Chen and Shen [55] have presented an application of spectral methods to the solution of the Allen-Cahn and Cahn-Hilliard equations. The method they used is a *semi-implicit* or *implicit-explicit* (IMEX) method. The stiffness arising from the fourth-order term in the Cahn-Hilliard equation is addressed by treating the term implicitly, while the nonlinear term, involving the derivative of the bulk free energy, is treated explicitly. This allows for an increase in Δt of 2–3 orders of magnitude compared to the explicit finite difference method.

A similar spectral method — the *exponential time-differencing* method — has been proposed by Cox and Matthews [56] for the solution of stiff PDEs. In this case, the linear fourth-order term is integrated exactly via the use of an integrating factor. What remains is to then find an approximation to the integral involving the nonlinear term.

Another approach to dealing with the problem of stiffness is to construct methods that are *unconditionally stable*. This means that the numerical solution does not become unstable, regardless of the step size chosen. Eyre [57] has presented implicit and semi-implicit methods, for the Cahn-Hilliard equation, that are unconditionally stable.

In the following sections, an outline of the main methods used in solving the Cahn-Hilliard equation are presented. The advantages and disadvantages of each method are also considered.

4.1 Finite difference method

Consider the Taylor series of a function, f, about the point x,

$$f(x + \Delta x) = f(x) + f'(x)\Delta x + \frac{f''(x)}{2!}\Delta x^2 + \cdots . \tag{4.2}$$

Truncating the series at first order in Δx, we obtain an approximation for the first derivative:

$$f'(x) \approx \frac{f(x + \Delta x) - f(x)}{\Delta x} , \tag{4.3}$$

which is exact in the limit $\Delta x \to 0$. Equation (4.3) is the *forward* finite difference method which uses function values at x and $x + \Delta x$ to evaluate an approximation to the first derivative. It is convenient to use the subscript i to represent the i^{th} gridpoint in the x direction, thus

$$f'(x) \approx \frac{f_{i+1} - f_i}{\Delta x} \,. \tag{4.4}$$

If, on the other hand, the derivative is evaluated in the opposite direction on the grid, we obtain the *backward* finite difference method:

$$f'(x) \approx \frac{f_i - f_{i-1}}{\Delta x} \,. \tag{4.5}$$

Similarly, we may use the adjacent cells to evaluate the derivative via the *central* difference approximation,

$$f'(x) \approx \frac{f_{i+1} - f_{i-1}}{2\Delta x} \,. \tag{4.6}$$

Both the forward and backward difference approximations are accurate to first order in Δx, while the central difference approximation is second order accurate.

In order to obtain approximations to the second derivative, $f''(x)$, we may apply the approximations given above for $f'(x)$ twice. The forward difference approximation for $f''(x)$ is thus

$$f''(x) \approx \frac{f_{i+2} - 2f_{i+1} + f_i}{(\Delta x)^2} \,. \tag{4.7}$$

Similarly, the backward difference approximation is

$$f''(x) \approx \frac{f_i - 2f_{i-1} + f_{i-2}}{(\Delta x)^2} \,. \tag{4.8}$$

The most common choice for evaluating $f''(x)$ is perhaps the central difference approximation, given by

$$f''(x) \approx \frac{f_{i+1} - 2f_i + f_{i-1}}{(\Delta x)^2} \,. \tag{4.9}$$

Of course, it is also possible to combine the forward, backward and central difference operators in other ways, to obtain various other approximations for $f''(x)$.

In two dimensions, the central difference approximation for $\nabla^2 f(x, y)$ is given by

$$\begin{aligned} \nabla^2 f(x,y) \;\; &\approx \;\; \frac{f_{i+1,j} - 2f_{i,j} + f_{i-1,j}}{(\Delta x)^2} \\ &\quad + \frac{f_{i,j+1} - 2f_{i,j} + f_{i,j-1}}{(\Delta y)^2} \,, \end{aligned} \tag{4.10}$$

where the subscript j is used to represent the y direction. This approximation for the Laplacian in 2D uses the value of the function at five points – the point at which it is being calculated along with four neighbouring points. Various other approximations can also be used. If, for example, a more accurate calculation is required, then we may use the nine-point finite-difference stencil shown in figure 4.1. In this case, an appropriate formula for the Laplacian is

given by [45, 58]

$$\nabla^2 f(x,y) \approx \frac{1}{(\Delta x)^2}\Big[\frac{1}{2}\big(f_{i+1,j}+f_{i-1,j}+f_{i,j+1}+f_{i,j-1}\big) + \frac{1}{4}\big(f_{i+1,j+1}+f_{i-1,j+1}+f_{i+1,j-1}+f_{i-1,j-1}\big) - 3f_{i,j}\Big], \tag{4.11}$$

where we have assumed that $\Delta x = \Delta y$.

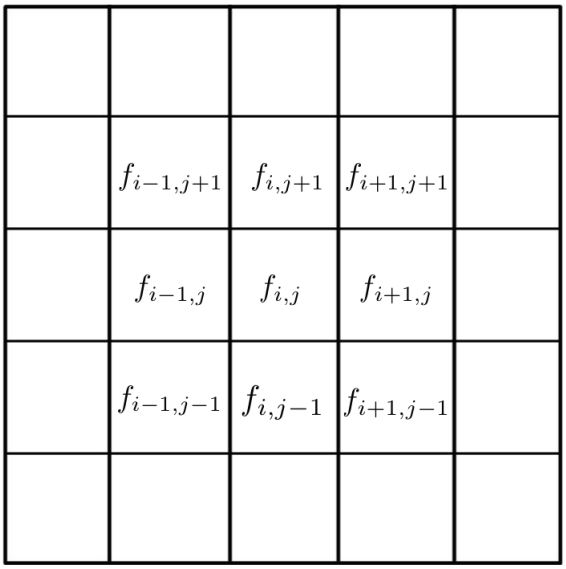


Figure 4.1: 9-point stencil used for calculating the finite difference approximation of the Laplacian in 2D.

4.1.1 Boundary conditions

Since the finite-difference approximation of a derivative requires function values at neighbouring nodes, the approximation cannot be carried out for nodes

along the edges of the domain, as some of the neighbouring nodes required for the calculation do not exist. In order to overcome this, the implementation of boundary conditions may be carried out by using a set of *ghost nodes* along the boundary, as shown in figure 4.2 (the interior nodes constitute the domain on which the equation is to be solved, while the surrounding yellow nodes are the ghost nodes). The ghost nodes are then given appropriate values, in order to satisfy the boundary conditions.

For example, for zero-flux boundary conditons, the ghost nodes on the left and right boundaries are chosen to take the same value as the cells two places directly to the right and left respectively, so that the first derivative in the horizontal direction is zero at the boundary. Similarly, the ghost nodes located at the upper and lower boundaries are given the same values as the cells two places directly below and above respectively, in order that the first derivative in the vertical direction is zero.

For periodic boundary conditions, the ghost nodes on each edge are set to be the same as the actual nodes on the opposite edge, so that the grid effectively wraps round on itself.

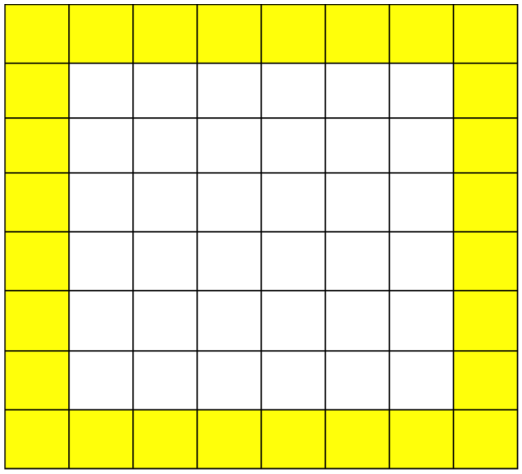


Figure 4.2: *Ghost nodes* are in yellow.

4.2 Time discretization

4.2.1 Explicit methods

Consider a time-dependent partial differential equation of the form

$$\frac{\partial}{\partial t} f(\mathbf{x}, t) = u(\mathbf{x}, t)\,. \tag{4.12}$$

If we use the forward Euler method to discretize the temporal derivative, then

$$\frac{f(\mathbf{x}, t + \Delta t) - f(\mathbf{x}, t)}{\Delta t} \approx u(\mathbf{x}, t)\,, \tag{4.13}$$

and we may rewrite this as

$$f(\mathbf{x}, t + \Delta t) = f(\mathbf{x}, t) + u(\mathbf{x}, t)\Delta t\,. \tag{4.14}$$

Equation (4.14) is an *explicit* scheme — at each time step, the function f is calculated using only information from the previous time step.

As an example, let us consider the Cahn-Hilliard equation in the following form:

$$\frac{\partial \phi}{\partial t} = M \nabla^2 \mu \,, \tag{4.15}$$

with μ given by

$$\mu = \frac{\partial f_0}{\partial \phi} - \kappa \nabla^2 \phi \,. \tag{4.16}$$

In order to solve equation (4.15) using the explicit finite difference method (equation (4.14)) for the time derivative, along with equation (4.10) for the Laplacian, we may follow the procedure outlined here:

1. Discretize ϕ and μ on a grid with N_x cells in the x direction and N_y cells in the y directiion. As discussed previously, additional *ghost* cells are required for the implementation of boundary conditions. The total number of cells will therefore be $(N_x + 2) \times (N_y + 2)$.

2. Initialise ϕ.

3. **for** $t = 0 \longrightarrow t = t_{total}$:

    - Enforce boundary conditions on ϕ.
    - Calculate $\nabla^2 \phi$ at each interior gridpoint using equation (4.10) or (4.11). Use this to calculate μ at each gridpoint.
    - Calculate $\nabla^2 \mu$ at each gridpoint, and use this to update ϕ via

equation (4.14):

$$\phi_{i,j}^{n+1} = \phi_{i,j}^{n} M \Delta t \nabla^2 \mu$$

end for

Here, the superscript, n, refers to time, t, while n+1 refers to time, t+Δt. The simplicity of this method makes it a popular choice for phase-field models; however, as metioned previously, the method has a severe restriction on the size of Δt (equation 4.1), when applied to the Cahn-Hilliard equation, owing to the presence of the fourth-order derivative.

4.2.2 Implicit methods

Implicit methods find a solution to a given problem by solving a system of equations that involves the current state of the system as well as its state at a later time. For example, at time $t + \Delta t$, the Cahn-Hilliard equation (equation (4.15)) may be discretized in time using the backward difference operator, while the space discretization may be carried out using the central difference operator. The resulting finite difference scheme is given by

$$\begin{aligned} \frac{\phi^{n+1} - \phi^{n}}{\Delta t} &= M \left[\frac{\mu_{i+1,j}^{n+1} - 2\mu_{i,j}^{n+1} + \mu_{i-1,j}^{n+1}}{(\Delta x)^2} \right. \\ &\quad \left. + \frac{\mu_{i,j+1}^{n+1} - 2\mu_{i,j}^{n+1} + \mu_{i,j-1}^{n+1}}{(\Delta y)^2} \right]. \end{aligned} \tag{4.17}$$

We are therefore required to solve a linear system of equations,

$$\mathbf{A}\vec{\phi}^{n+1} = \mathbf{b}(\vec{\phi}^{n}), \tag{4.18}$$

at each time step.

Although implicit methods offer greater numerical stability compared to explicit methods, the requirement to solve a linear system of equations at each time step can outweigh the benefits of using a larger step size. Direct matrix inversion can take $\mathcal{O}(N^6)$ operations, while iterative methods generally require $\mathcal{O}(N^3)$ – $\mathcal{O}(N^4)$ operations [45]. For more details on implicit methods, the reader is referred to ref. [59].

4.3 Spectral methods

In order to alleviate the time step constraints imposed by explicit methods and at the same time avoid costly matrix inversion incurred when using implicit methods, Chen and Shen [55] presented a *semi-implicit* Fourier spectral method for solving the Cahn-Hilliard and Allen-Cahn equations. The method treats the fourth-order term implicitly and the nonlinear term explicitly, and allows an increase of 2-3 orders of magnitude compared to the explicit Euler method for the Cahn-Hilliard equation, while requiring $O(N^2)$ steps (where N is the size of the system), thus greatly improving efficiency.

Consider the forward Fourier Transform of a function,

$$\tilde{f}(k) = \int_{-\infty}^{\infty} f(x) \mathrm{e}^{-ikx} \, \mathrm{d}x \,, \tag{4.19}$$

and its inverse,

$$f(x) = \int_{-\infty}^{\infty} \tilde{f}(k) \mathrm{e}^{ikx} \, \mathrm{d}x \, . \tag{4.20}$$

Taking the Fourier transform of the derivative, $f'(x)$, we obtain

$$\begin{aligned} \int_{-\infty}^{\infty} f'(x) \mathrm{e}^{-ikx} \, \mathrm{d}x &= \left[\mathrm{e}^{-ikx} f(x) \right]_{-\infty}^{\infty} - \int_{-\infty}^{\infty} -ikf(x) \mathrm{e}^{-ikx} \, \mathrm{d}x \\ &= ik \int_{-\infty}^{\infty} f(x) \mathrm{e}^{-ikx} \, \mathrm{d}x \\ &= ik\tilde{f}(k) \, . \end{aligned} \tag{4.21}$$

This result — namely, that the Fourier transform of the derivative of a function is simply the Fourier transform of the function itself multiplied by ik — greatly simplifies the calculation of derivatives in Fourier space. Thus, the Cahn-Hilliard equation,

$$\frac{\partial \phi}{\partial t} = M\nabla^2 \left(\frac{\partial f_0}{\partial \phi} - \kappa \nabla^2 \phi \right) \tag{4.22}$$

may be written as

$$\frac{\partial \tilde{\phi}(k,t)}{\partial t} = -Mk^2 \left\{ \frac{\partial f_0}{\partial \phi} \right\}_k - M\kappa^2 k^4 \tilde{\phi}(k,t) \, , \tag{4.23}$$

after taking the Fourier transform. The algorithm for the semi-implicit Fourier spectral method is as follows:

1. Calculate Discrete Fourier Transforms of ϕ and $\frac{\partial f_0}{\partial \phi}$;

2. Update the Fourier transform, $\tilde{\phi}_k$, of ϕ, treating the nonlinear term

explicitly and the fourth-order term implicitly,

$$\begin{aligned} \frac{\tilde{\phi}^{n+1} - \tilde{\phi}^n}{\Delta t} &= -k^2 \left\{ \frac{\partial f_0}{\partial \phi} \right\}_k^n - \kappa^2 k^4 \tilde{\phi}^{n+1} \\ \longrightarrow \tilde{\phi}^{n+1} &= \frac{\tilde{\phi}^n - \Delta t k^2 \left\{ \frac{\partial f_0}{\partial \phi} \right\}_k^n}{1 + \Delta t \kappa^2 k^4}, \end{aligned} \tag{4.24}$$

where the superscript, n, refers to the current time step, and $n+1$ refers to the next one.

3. Take the inverse transform to obtain ϕ^{n+1}.

4. Repeat steps 1-3 with the updated values of ϕ (i.e. set $\phi^n = \phi^{n+1}$ on the whole domain, and go to step 1).

4.4 Exponential Time-Differencing

Consider equation (4.23), the Fourier transform of the Cahn-Hilliard equation, and let us rewrite it as

$$\frac{\partial \tilde{\phi}(k,t)}{\partial t} = \hat{L}\tilde{\phi} + \hat{N}\,, \tag{4.25}$$

where the linear operator, $\hat{L} = -M\kappa k^4$, and $\hat{N} = -Mk^2 \left\{ \frac{\partial f_0}{\partial \phi} \right\}_k$ is a non-linear function of $\tilde{\phi}$. Multiplying through by the integrating factor, $\mathrm{e}^{-\hat{L}t}$, we obtain

$$\frac{\partial}{\partial t}\left(\tilde{\phi} \mathrm{e}^{-\hat{L}t} \right) = \mathrm{e}^{-\hat{L}t} \hat{N}(t)\,. \tag{4.26}$$

Integrating the equation over one time-step, from t to $t + \Delta t$, we obtain

$$\begin{aligned}\int_t^{t+\Delta t} \frac{\partial}{\partial \tau}\left(\tilde{\phi} \mathrm{e}^{-\hat{L}\tau}\right) \mathrm{d}\tau &= \tilde{\phi}(k, t+\Delta t)\mathrm{e}^{-\hat{L}(t+\Delta t)} - \tilde{\phi}(k,t)\mathrm{e}^{-\hat{L}t} \\ &= \int_t^{t+\Delta t} \mathrm{e}^{-\hat{L}\tau}\hat{N}\,\mathrm{d}\tau\,, \end{aligned} \tag{4.27}$$

where τ is a dummy variable. Thus, after rearranging, we arrive at an expression for $\tilde{\phi}(k, t + \Delta t)$:

$$\begin{aligned}\tilde{\phi}(k, t+\Delta t) &= \mathrm{e}^{\hat{L}\Delta t}\tilde{\phi}(k,t) + \mathrm{e}^{\hat{L}\Delta t}\int_t^{t+\Delta t} \mathrm{e}^{-\hat{L}\tau}\hat{N}(\tau)\,\mathrm{d}\tau \\ &= \mathrm{e}^{\hat{L}\Delta t}\tilde{\phi}(k,t) + \mathrm{e}^{\hat{L}\Delta t}\int_0^{t+\Delta t} \mathrm{e}^{-\hat{L}\tau}\hat{N}(t+\tau)\,\mathrm{d}\tau\,. \end{aligned} \tag{4.28}$$

Equation (4.28) is exact, and no approxmations or assumptions have been made so far. Hence, the essence of the exponential time-differencing method is to integrate the linear term *exactly*, thus removing any stiffness associated with it from the problem. What remains is to then find an approximation to the integral involving nonlinear terms, and these approximations may take several forms. Cox and Matthews [56] provide details of various numerical schemes for the solution of the nonlinear integral, including explicit Euler methods and Runge-Kutta methods of varying order of accuracy. They found that, in general, their proposed fourth order Runge-Kutta scheme (ETDRK4) has the largest region of stability compared to the explicit Euler schemes and to the lower order Runge-Kutta schemes, ETDRK2 and ETDRK3 (of order two and three respectively). They also conducted a comparison of numerical simulations of stiff PDEs using other implicit-explicit methods and integrating factor methods, and found ETDRK4 to be consistently among the

most superior schemes in terms of both accuracy and its stability properties. Kassam and Trefethen [60], however, have shown ETDRK4 to be an unstable scheme, due to rounding errors induced when calculating the Runge-Kutta coefficients. In order to circumvent this problem, Kassam and Trefethen modified the scheme, and proposed a contour integral based approach to the calculation of the coefficients. Other modifications have also been proposed, such as using the truncated Taylor Series for each coefficient.

4.5 Unconditionally gradient-stable algorithms

Several unconditionally stable schemes for the solution of the Cahn-Hilliard equation with a polynomial form of the free energy have been proposed in recent years. The general idea behind such schemes is to develop an algorithm that guarantees that the free energy cannot increase from one time step to another, independent of how large the time step may be. Eyre [57] has shown that if the free energy can be split into a convex and concave part, then we may construct a numerical scheme for the Cahn-Hilliard equation that has no stability constraint on the step size; the time step is then limited by accuracy constraints alone.

Using the polynomial form of the free energy, given by

$$f_0 = \frac{\phi^4}{4} - \frac{\phi^2}{2}\,, \tag{4.29}$$

we may write the Cahn-Hilliard equation as

$$\frac{\partial \phi}{\partial t} = M\nabla^2\Big(\phi^3 - \phi - \kappa\nabla^2\phi\Big). \tag{4.30}$$

For each of the three terms inside the brackets, let us now add and subtract the corresponding term multiplied by a constant factor a_i $(i = 1, 2, 3)$. Thus, we may rewrite equation (4.30) as

$$\begin{aligned}\frac{\partial \phi}{\partial t} &= M\nabla^2\Big(a_1\phi^3 + (1-a_1)\phi^3 - a_2\phi - (1-a_2)\phi \\ &\qquad -a_3\kappa\nabla^2\phi - (1-a_3)\kappa\nabla^2\Big). \end{aligned}\tag{4.31}$$

From this we may construct a semi-implicit splitting in which the coefficients, a_i, determine whether a term is calculated explicitly, implicitly or as a mixture of the two:

$$\begin{aligned}\phi(\mathbf{x}, t+\Delta t) &- M\Delta t\nabla^2\Big[(1-a_1)\phi^3(\mathbf{x}, t+\Delta t) - (1-a_2)\phi(\mathbf{x}, t+\Delta t) \\ &\qquad -(1-a_3)\kappa\nabla^2\phi(\mathbf{x}, t+\Delta t)\Big] \\ &= \phi(\mathbf{x}, t) + M\Delta t\nabla^2\Big[(a_1\phi^3(\mathbf{x}, t) - a_2\phi(\mathbf{x}, t) \\ &\qquad -a_3\kappa\nabla^2\phi(\mathbf{x}, t)\Big]. \end{aligned}\tag{4.32}$$

For $\kappa = 1$ and $M = 1$, and if $a_1 = 1$, that is, if the ϕ^3 term is treated explicitly, then it has been shown that this scheme is unconditionally stable

for $a_2 < 0.5$ and $a_3 > 2$ [61, 62].

Similarly, for the logarithmic form of the free energy,

$$f_0 = \phi \ln \phi + (1-\phi)\ln(1-\phi) + \Omega\phi(1-\phi)\,, \tag{4.33}$$

we have

$$\begin{aligned}
\frac{\partial \phi}{\partial t} &= M\nabla^2\Bigg(a_1 \ln\left(\frac{\phi}{1-\phi}\right) + (1-a_1)\ln\left(\frac{\phi}{1-\phi}\right) \\
&\qquad +a_2\Omega(1-2\phi) + (1-a_2)\Omega(1-2\phi) \\
&\qquad -a_3\kappa\nabla^2\phi - (1-a_3)\kappa\nabla^2\phi\Bigg)\,,
\end{aligned} \tag{4.34}$$

which may be solved using the following scheme

$$\begin{aligned}
\phi(\mathbf{x}, t+\Delta t) &+ M\Delta t\nabla^2\Bigg[-(1-a_2)\Omega(1-2\phi(\mathbf{x},t+\Delta t)) \\
&\qquad -(1-a_1)\ln\left(\frac{\phi(\mathbf{x},t+\Delta t)}{1-\phi(\mathbf{x},t+\Delta t)}\right) \\
&\qquad +(1-a_3)\kappa\nabla^2\phi(\mathbf{x},t+\Delta t)\Bigg] \\
&= \phi(\mathbf{x},t) + M\Delta t\nabla^2\Bigg[a_1\ln\left(\frac{\phi(\mathbf{x},t)}{1-\phi(\mathbf{x},t+\Delta t)}\right) \\
&\qquad +a_2\Omega(1-2\phi) - a_3\kappa\nabla^2\phi(\mathbf{x},t)\Bigg]\,.
\end{aligned} \tag{4.35}$$

If we set $a_1 = 1$, such that the logarithm term is treated explicitly, this scheme is unconditionally stable, for example, if $a_2 = 3$ and $a_3 = 0$, with $\Omega = 3.5$, $\kappa = 1$ and $M = 1$.

4.6 Adaptive time step

Solutions of the Cahn-Hilliard equation display greatly varying temporal scales. If we start with a homogeneous mixture and apply a fluctuation, the initial process of spinodal decomposition occurs on a much shorter timescale than the subsequent process of coarsening. For such situations, efficiency can be significantly increased if, instead of using a fixed time step, we use a variable time step.

For example, a commonly used algorithm for varying the time-step is as follows:

- Calculate $\phi^{n+1} \equiv \phi(t + \Delta t)$ from $\phi^n \equiv \phi(t)$ in two steps, using a time-step of size $\Delta t/2$;
- Calculate $\hat{\phi}^{n+1}$ from ϕ^n in one step of size Δt;
- The error is then: $e = ||\phi^{n+1} - \hat{\phi}^{n+1}|| = \left[\sum_i \sum_j (\phi_{ij}^{n+1} - \hat{\phi}_{ij}^{n+1})^2 \right]^{1/2}$
- If the error is less than the desired maximum error, $e_{\max}$, then let $\Delta t \longrightarrow \left(\frac{e_{\text{tol}}}{e} \right)^{1/2} \Delta t$;
- Otherwise, discard the solution and try $\Delta t \longrightarrow \Delta t/2$.

As noted by Söderlind and Wang [63], it is often necessary to take limiting cases into account when using such an algorithm, in order to prevent too large a step being taken. As a result, this can lead to numerical instabilities. Söderlind and Wang have instead proposed an algorithm for adjusting the time-step based on control theory:

$$(\Delta t)^{n+1} = \left(\frac{\epsilon}{\hat{r}^n}\right)^{\beta_1} \left(\frac{\epsilon}{\hat{r}^{n-1}}\right)^{\beta_2} \left(\frac{(\Delta t)^n}{(\Delta t)^{n-1}}\right)^{-\alpha_2} (\Delta t)^n \,. \tag{4.36}$$

Here, β_1, β_2 and α_2 are model parameters that can be found in ref. [63], ϵ is a fraction of the tolerance, and $\hat{r}^n$ is a local error estimator.

4.7 Discussion

By testing the numerical methods outlined in this chapter, it is clear that the semi-implicit spectral methods — the method of Chen and Shen [55] (section 4.3) and the Exponential Time Differencing method of Cox and Matthews [56] (section 4.4) — are distinctly more efficient than the finite difference methods. However, despite the fact that ETD methods are considered to have a greater region of stability than the semi-implicit method of Chen and Shen, we found that when using large regular solution parameters, the difference in efficiency between the methods is negligible, and that the solution requires very small time steps in all cases. Indeed, in many cases, we found that the method of Chen and Shen allows the use of a larger time step than the ETDRK2 and ETDRK4 methods. Moreover, we found that the unconditionally stable algorithms, that have been described in section 4.5, are

only unconditionally stable in the case of small regular solution parameters, and additionally, in the case of the ternary Cahn-Hilliard equations, if all of the regular solution parameters are equal. Since we require the use of large regular solution parameters in our simulations, we have chosen to use the method of Chen and Shen which has been described in section 4.3. In terms of using an adaptive step size, we note that, when using large regular solution parameters, the methods described in section 4.6 become unstable, and that the method of Söderlind and Wang is not suitable for this scenario. Thus, in order to avoid the overhead involved with the time-adpative strategies, a fixed time step is used for all simulations presented in this work.

Chapter 5

ELASTIC EFFECTS CAUSED BY LATTICE MISMATCH

For systems, such as CuAg, in which there is a considerable lattice mismatch (approximately 12%) between elements, elastic effects must be taken into account. In order to do this, an elastic energy term, E^{el}, is added to the free energy functional, and the stress and strain and/or the elastic constants are expressed in terms of the order parameters.

Consider the displacement of a material resulting from a deformation, as shown in figure 5.1. In order to quantify the deformation, we choose the *reference state* to be the state of the material prior to deformation — in other words, the *undeformed* state. The displacement of the material is then considered relative to the undeformed state.

Let the position vectors of an element of material in the deformed and undeformed states be $\mathbf{x}$ and $\mathbf{x}'$ respectively. The *displacement vector* is then the

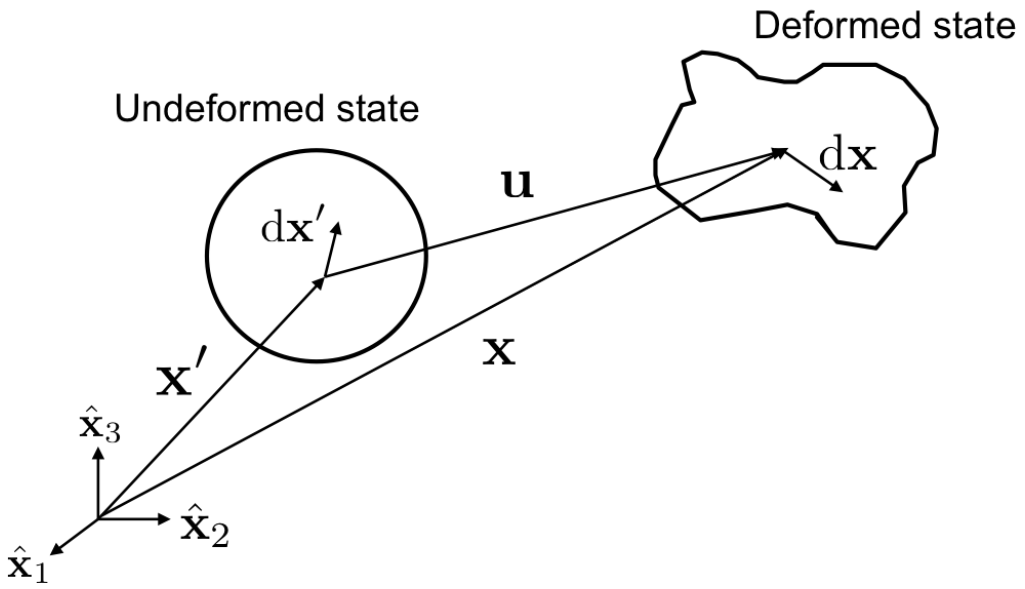


Figure 5.1: Material in the undeformed, reference state undergoes a deformation which displaces the material from $\mathbf{x}'$ to $\mathbf{x}$.

vector that connects the same element in both states, and is given by [64]

$$\mathbf{u} = \mathbf{x} - \mathbf{x}' \,, \tag{5.1}$$

or, for the individual components of the vector represented by the index i,

$$u_i = x_i - x_i' \,. \tag{5.2}$$

An infinitesimally small vector, $\mathrm{d}\mathbf{x}'$, in the reference state, is deformed into the vector $\mathrm{d}\mathbf{x}$ in the deformed state. The relationship between the two may be deduced by the chain rule [64]:

$$\mathrm{d}x_i = \frac{\partial x_i}{\partial x_j'} \mathrm{d}x_j' \,, \tag{5.3}$$

where we have used the Einstein summation convention, in which repeated indices are summed over, so that equation (5.3) implies

$$\mathrm{d}x_1 = \frac{\partial x_1}{\partial x'_1}\mathrm{d}x'_1 + \frac{\partial x_1}{\partial x'_2}\mathrm{d}x'_2 + \frac{\partial x_1}{\partial x'_3}\mathrm{d}x'_3\,, \tag{5.4}$$

and similarly for $i = 2$ and $i = 3$.

The quantity $\frac{\partial x_i}{\partial x'_j}$ is a measure of the deformation, and is known as the *deformation gradient tensor*, F_{ij} [64]:

$$F_{ij} = \frac{\partial x_i}{\partial x'_j}\,. \tag{5.5}$$

Hence,

$$\mathrm{d}x_i = F_{ij}\mathrm{d}x'_j\,. \tag{5.6}$$

In order to relate the deformation gradient tensor to the displacement, let us rewrite equation (5.2) as

$$x_i = u_i + x'_i\,, \tag{5.7}$$

and then differentiate with respect to x'_j, to obtain

$$\frac{\partial x_i}{\partial x'_j} = \frac{\partial u_i}{\partial x'_j} + \frac{\partial x'_i}{\partial x'_j}\,. \tag{5.8}$$

The term on the left hand side in equation (5.8) is simply the deformation gradient tensor, F_{ij}. The second term on the right is equal to one when $i = j$

and is zero for $i \neq j$. Hence, rewriting equation (5.8), we obtain

$$F_{ij} = \frac{\partial u_i}{\partial x'_j} + \delta_{ij}\,, \tag{5.9}$$

where δ_{ij} is the Kronecker delta.

In order to define the strain, let us consider the stretching of the material in going from the reference state to the deformed state. Let the lengths of the vectors $\mathrm{d}\mathbf{x}$ and $\mathrm{d}\mathbf{x}'$ be $\mathrm{d}s$ and $\mathrm{d}s'$ respectively. Taking the dot product of $\mathrm{d}\mathbf{x}$ with itself, we have [64]

$$(\mathrm{d}s)^2 = \mathrm{d}\mathbf{x}\cdot\mathrm{d}\mathbf{x} = \mathrm{d}x_i\mathrm{d}x_i\,. \tag{5.10}$$

Now, from equation (5.6), we have that

$$\begin{aligned} \mathrm{d}x_i\mathrm{d}x_i &= F_{ij}\mathrm{d}x'_jF_{ik}\mathrm{d}x'_k \\ &= \mathrm{d}x'_jF_{ij}F_{ik}\mathrm{d}x'_k\,. \end{aligned} \tag{5.11}$$

In the reference state, we have

$$(\mathrm{d}s')^2 = \mathrm{d}x'_j\mathrm{d}x'_j = \mathrm{d}x'_j\delta_{jk}\mathrm{d}x'_k\,, \tag{5.12}$$

and therefore, the stretch may be measured by the difference:

$$\begin{aligned}(\mathrm{d}s)^2 - (\mathrm{d}s')^2 &= \mathrm{d}x'_j F_{ij} F_{ik} \mathrm{d}x'_k - \mathrm{d}x'_j \delta_{jk} \mathrm{d}x'_k \\ &= \mathrm{d}x'_j \big(F_{ij}F_{ik} - \delta_{jk}\big)\mathrm{d}x'_k \\ &= 2\mathrm{d}x'_j E_{jk} \mathrm{d}x'_k \,, \end{aligned} \tag{5.13}$$

where E_{jk} is the Lagrangian strain tensor [64], defined as

$$E_{jk} = \frac{1}{2}\big(F_{ij}F_{jk} - \delta_{jk}\big) \,. \tag{5.14}$$

Using equation (5.9) for F_{ij}, we may rewrite the strain tensor as

$$\begin{aligned} E_{jk} &= \frac{1}{2}\left[\left(\frac{\partial u_i}{\partial x'_j} + \delta_{ij}\right)\left(\frac{\partial u_j}{\partial x'_k} + \delta_{jk}\right)\right] \\ &= \frac{1}{2}\left[\frac{\partial u_j}{\partial x'_k} + \frac{\partial u_k}{\partial x'_j} + \frac{\partial u_i}{\partial x'_j}\frac{\partial u_i}{\partial x'_k}\right] . \end{aligned} \tag{5.15}$$

If we consider small deformations only, then the third term,

$$\frac{\partial u_i}{\partial x'_j}\frac{\partial u_i}{\partial x'_k} \,, \tag{5.16}$$

may be neglected. In this case, we obtain the *small strain tensor*, ϵ_{jk}

$$\epsilon_{jk} = \frac{1}{2}\left[\frac{\partial u_j}{\partial x'_k} + \frac{\partial u_k}{\partial x'_j}\right] . \tag{5.17}$$

Equation (5.17) gives the total strain, and is the sum of the elastic and misfit strains, $\epsilon_{jk}^{\text{el}}$ and $\epsilon_{jk}^{\text{misfit}}$, respectively:

$$\epsilon_{ij} = \epsilon_{ij}^{\text{el}} + \epsilon_{ij}^{\text{misfit}} \,. \tag{5.18}$$

5.1 Stress

In linear elasticity theory, the stress is given by Hooke's Law,

$$\sigma_{ij} = C_{ijkl}\epsilon_{kl}^{\text{el}} \,, \tag{5.19}$$

where C_{ijkl} is the elastic moduli tensor. Using equations (5.18), (5.17) and (5.19), the stress is given by

$$\sigma_{ij} = C_{ijkl}\frac{1}{2}\left[\frac{\partial u_k}{\partial x_l} + \frac{\partial u_l}{\partial x_k}\right] . \tag{5.20}$$

In the absence of an external force, the equations of mechanical equilibrium are [64]

$$\frac{\partial \sigma_{ij}}{\partial x_j} = 0 \,. \tag{5.21}$$

Applying this equation to equation (5.20), we obtain the *Navier-Lamé* equations of elasticity:

$$\frac{\partial}{\partial x_j}\left\{C_{ijkl}\left[\frac{1}{2}\left(\frac{\partial u_k}{\partial x_l} + \frac{\partial u_l}{\partial x_k}\right) - \epsilon_{kl}^{0}\right]\right\} = 0 \,. \tag{5.22}$$

5.2 The stiffness tensor, C_{ijkl}

In the general, three-dimensional case, the fourth-rank stiffness tensor, C_{ijkl}, has $3^4 = 81$ components. For a crystal lattice, however, the number of independent components is significantly reduced due to the inherent symmetries of the system. For an anisotropic material, there are at most 21 independent components to the stiffness tensor. On the other hand, an isotropic material may be characterized by just 2 independent quantities, such that [64]

$$C_{ijkl} = \lambda\delta_{ij}\delta_{kl} + \mu(\delta_{ik}\delta_{jl} + \delta_{il}\delta_{jk})\,, \tag{5.23}$$

where λ and μ are referred to as Lamé's constants.

At this point we may simplify the fourth-rank stiffness tensor, by transforming it into a matrix, using the *Voigt notation*, in which $C_{ijkl} \longrightarrow C_{ab}$, in the following way

ij	11	22	33	23, 32	13, 31	12, 21
a	1	2	3	4	5	6

For a cubic material, we may then write

$$C_{ijkl} = C_{12}\delta_{ij}\delta_{kl} + C_{44}(\delta_{ik}\delta_{jl} + \delta_{il}\delta_{jk}) + (C_{11} - C_{12} - 2C_{44})\delta_{ijkl}\,. \tag{5.24}$$

In the isotropic case, we have

$$\begin{aligned} C_{11} &= C_{12} + 2C_{44} \\ C_{12} &= \lambda \\ C_{44} &= \mu\,. \end{aligned} \tag{5.25}$$

5.3 Coupling with the Cahn-Hilliard equation

In order to couple elastic effects with the Cahn-Hilliard equation, we must add an elastic energy term to the free energy functional (equation (2.9)), such that [65, 66, 67, 68]

$$F[\phi, T] = \int_V \left(f_0(\phi, T) + \frac{\kappa}{2}(\nabla\phi)^2 + E^{\mathrm{el}} \right) \mathrm{d}V\,. \tag{5.26}$$

Applying equation (2.27), we then obtain

$$\begin{aligned} \frac{\partial\phi}{\partial t} &= \nabla \cdot \left(M\nabla\frac{\delta F}{\delta\phi} \right) \\ &= M\nabla^2\left(\frac{\partial f_0}{\partial\phi} + \frac{\partial E^{\mathrm{el}}}{\partial\phi} - \kappa\nabla^2\phi \right). \end{aligned} \tag{5.27}$$

Elastic effects are included by connecting the order parameter, ϕ, with the elastic moduli tensor and the misfit strain, so that $C_{ijkl} = C_{ijkl}(\phi)$ and

$\epsilon^{\text{misfit}} = \epsilon^{\text{misfit}}(\phi)$. More specifically [66, 67, 68],

$$C_{ijkl}(\phi) = C^0_{ijkl} + \chi(\phi)\Delta C_{ijkl}\,, \tag{5.28}$$

where C^0_{ijkl} is the elastic moduli tensor of one phase, $\chi(\phi)$ is an interpolating function and ΔC_{ijkl} is given by

$$\Delta C_{ijkl} = C^\beta_{ijkl} - C^\alpha_{ijkl}\,, \tag{5.29}$$

with C^α_{ijkl} and C^β_{ijkl} being the elastic moduli tensors for the α and β phases respectively. Similarly, the misfit strain is also interpolated between the two phases. If, for example, we take the undeformed lattice of the α phase to be the reference state, then the misfit strain will be zero in the α phase, and it will attain its maximum value, ϵ^T, in the β phase. Thus

$$\epsilon^{\text{misfit}}_{ij} = \gamma^T(\phi)\delta_{ij}\,, \tag{5.30}$$

where

$$\gamma^T(\phi) = \begin{cases} \epsilon^T & \phi = 1 \\ \tilde{\gamma}(\phi)\epsilon^T & 0 < \phi < 1 \\ 0 & \phi = 0 \end{cases}$$

with $\tilde{\gamma}(\phi)$ interpolating between the two phases. The maximum value of the transformation strain, ϵ^T, is given by

$$\epsilon^T = \frac{a^\beta - a^\alpha}{a^\alpha}\,, \tag{5.31}$$

where a^α and a^β are the lattice parameters of the pure α and β phases respectively.

5.3.1 Elastic energy

In order to calculate the elastic energy, we first solve the Navier-Lamé equations for the displacements. This allows us to then calculate the stress and elastic strain, from which we may obtain the elastic energy, E^{el}, via [66, 67, 68]

$$E^{\text{el}} = \frac{1}{2}\sigma_{ij}\epsilon_{ij}^{\text{el}}\,, \tag{5.32}$$

Using equations (5.19) and (5.18), we may write the elastic energy as

$$E^{\text{el}} = \frac{1}{2}(\epsilon_{ij} - \epsilon_{ij}^{\text{misfit}})C_{ijkl}(\epsilon_{kl} - \epsilon_{kl}^{\text{misfit}})\,. \tag{5.33}$$

To solve the elastic Cahn-Hilliard equation, we must calculate the derivative of $E^{\text{el}}(\phi)$ with respect to the order parameter, ϕ, at each time step as follows [66, 67, 68]

$$\begin{aligned}\frac{\partial E^{\text{el}}}{\partial \phi} &= \frac{1}{2}\frac{\partial}{\partial \phi}(\epsilon_{ij} - \epsilon_{ij}^{\text{misfit}})C_{ijkl}(\epsilon_{kl} - \epsilon_{kl}^{\text{misfit}}) \\ &\quad + \frac{1}{2}(\epsilon_{ij} - \epsilon_{ij}^{\text{misfit}})\frac{\partial}{\partial \phi}C_{ijkl}(\epsilon_{kl} - \epsilon_{kl}^{\text{misfit}}) \\ &\quad + \frac{1}{2}(\epsilon_{ij} - \epsilon_{ij}^{\text{misfit}})C_{ijkl}\frac{\partial}{\partial \phi}(\epsilon_{kl} - \epsilon_{kl}^{\text{misfit}})\,.\end{aligned} \tag{5.34}$$

We may now substitute for C_{ijkl} using equations (5.28) and (5.29) to obtain

$$\begin{aligned}
\frac{\partial E^{\mathrm{el}}}{\partial \phi} &= -\frac{1}{2}\epsilon^T \delta_{ij} \frac{\partial \tilde{\gamma}(\phi)}{\partial \phi} C_{ijkl}(\epsilon_{kl} - \epsilon^T_{kl}\tilde{\gamma}(\phi)\delta_{kl}) \\
&\quad + \frac{1}{2}(\epsilon_{ij} - \epsilon^T \tilde{\gamma}(\phi)\delta_{ij})\Delta C_{ijkl} \frac{\partial \chi(\phi)}{\partial \phi}(\epsilon_{kl} - \epsilon^T \tilde{\gamma}(\phi)\delta_{kl}) \\
&\quad + -\frac{1}{2}(\epsilon_{ij} - \epsilon^T_{ij}\tilde{\gamma}(\phi)\delta_{ij}) C_{ijkl}\epsilon^T_{kl}\delta_{kl} \frac{\partial \tilde{\gamma}(\phi)}{\partial \phi} \\
&= \frac{1}{2}\frac{\partial \chi(\phi)}{\partial \phi}\Delta C_{ijkl}(\epsilon_{ij} - \epsilon^{\mathrm{misfit}}_{ij})(\epsilon_{kl} - \epsilon^{\mathrm{misfit}}_{kl}) \\
&\quad - \frac{\partial \tilde{\gamma}(\phi)}{\partial \phi}\epsilon^T \delta_{ij} C_{ijkl}(\epsilon_{kl} - \epsilon^{\mathrm{misfit}}_{kl}) \qquad (5.35)
\end{aligned}$$

5.4 Numerical solution

In order to solve the Navier-Lamé equations, we use an iterative procedure in Fourier space [66, 67, 68] . Using equations (5.28) and (5.29) and substituting into equation (5.22), we may write the Navier-Lamé equations as

$$\frac{\partial}{\partial x_j}\left\{\left(C^0_{ijkl} + \chi(\phi)\Delta C_{ijkl}\right)\left(\frac{\partial u_l}{\partial x_k} - \epsilon^T \delta_{kl}\tilde{\gamma}(\phi)\right)\right\} = 0\,. \qquad (5.36)$$

To start the iteration, we assume that the elastic constants are the same in both phases, so that

$$C^{\alpha}_{ijkl} = C^{\beta}_{ijkl}\,, \qquad (5.37)$$

and therefore

$$\Delta C_{ijkl} = 0\,. \qquad (5.38)$$

We may then solve the Navier-Lamé equations, in the following form, directly in Fourier space:

$$C^0_{ijkl}\frac{\partial^2 u_l}{\partial x_j \partial x_k} = C^0_{ijkl}\epsilon^T \delta_{kl}\frac{\partial \tilde{\gamma}(\phi)}{\partial x_j}\,. \tag{5.39}$$

For the purpose of simplifying the equation, let us define a "misfit stress", σ^T_{ij}, via Hooke's law, such that

$$\sigma^T_{ij} = C^0_{ijkl}\epsilon^T \delta_{kl}\,. \tag{5.40}$$

We may then rewrite equation (5.39) as

$$C^0_{ijkl}\frac{\partial^2 u_l}{\partial x_j x_k} = \sigma^T_{ij}\frac{\partial \tilde{\gamma}(\phi)}{\partial x_j}\,. \tag{5.41}$$

Taking the Fourier transform of this equation, we obtain

$$\tilde{u}^0_l(\mathbf{q}) = -iq_j G_{il}\sigma^T_{ij}\tilde{\gamma}(\mathbf{q})\,, \tag{5.42}$$

where we have defined $\mathbf{q}$ as the wave vector and where

$$G^{-1}_{il} = C_{ijkl}q_j q_k\,. \tag{5.43}$$

Equation (5.42) may be solved directly in Fourier space. We may then drop the assumption that $\Delta C_{ijkl} = 0$, and use the solution we have to calculate the next iteration using

$$\tilde{u}^n_l(\mathbf{q}) = -iq_j G_{il}\sigma^T_{ij}\Lambda^{n-1}_{ij}\,, \tag{5.44}$$

where

$$\Lambda_{ij}^{n-1} = \sigma_{ij}^{T}\tilde{\gamma}(\mathbf{q}) + \Delta C_{ijrs}\epsilon^{T}\delta_{rs}\{\chi(\phi)\tilde{\gamma}(\phi)\}_{\mathbf{q}} - \Delta C_{ijrs}\left\{\chi(\phi)\frac{\partial u_m^{n-1}}{\partial x_n}\right\}_{\mathbf{q}}. \quad (5.45)$$

Here, the superscript, n, refers to the current solution and $n-1$ refers to the previous solution. The iteration is allowed to continue until convergence.

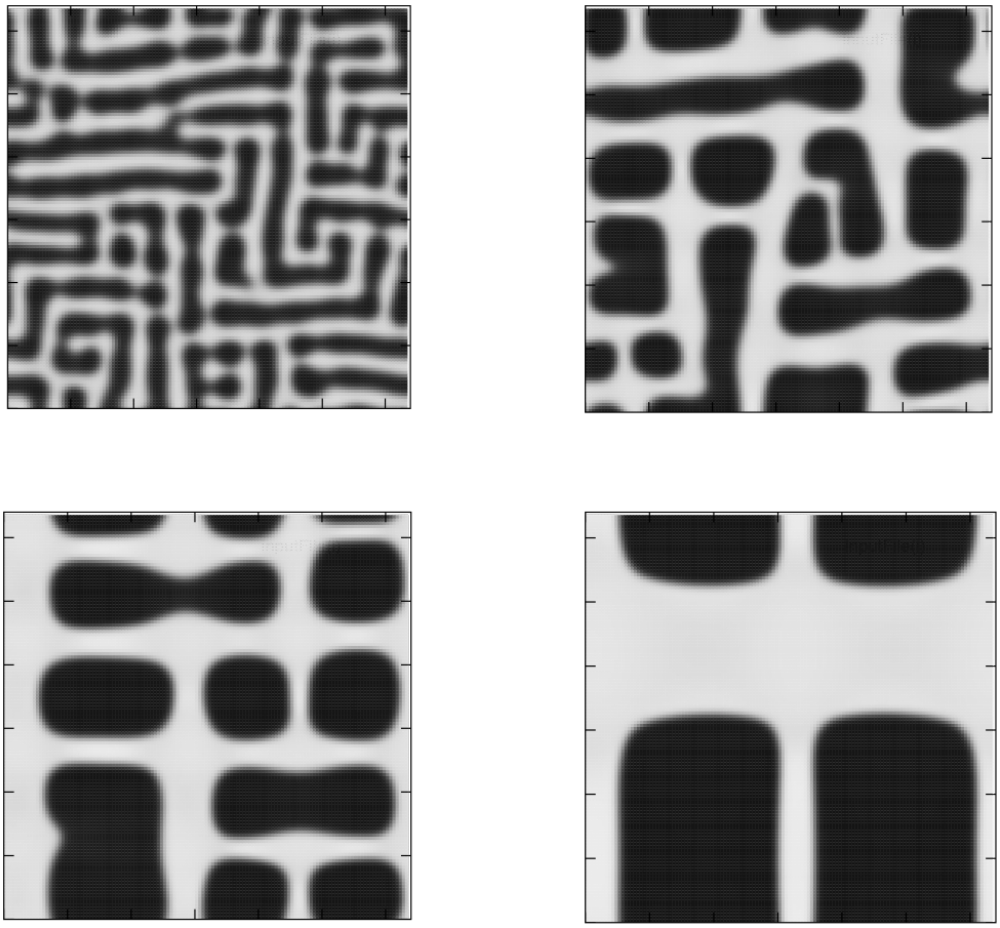


Figure 5.2: Numerical solution of the binary Cahn-Hilliard equation with elastic effects included.

Chapter 6

SIMULATIONS

In this chapter, results obtained from the numerical solution of the ternary Cahn-Hilliard equations are presented. Simulations are carried out using the semi-implicit Fourier spectral method of Chen and Shen [55], which has been described in section 4.3. An outline of the structure of the code used to implement the method is displayed in figure 6.1.

The initial conditions for each simulation are set such that we have a uniform mixture of composition $(\phi_1^0, \phi_2^0, \phi_3^0)$, where ϕ_1^0, ϕ_2^0 and ϕ_3^0 represent the overall fraction of components 1, 2 and 3 present. At each gridpoint, therefore, $\phi_1 = \phi_1^0$, $\phi_2 = \phi_2^0$ and $\phi_3 = \phi_3^0$. A small, random fluctuation is then applied, and the system is allowed to evolve.

In the following sections, the effect, on particle morphology, of varying regular solution parameters, varying particle composition, varying particle size and the addition of elastic effects (via a coupling with the Navier-Lamé equations) are studied. Results of simulations of the CuAg system are also presented.

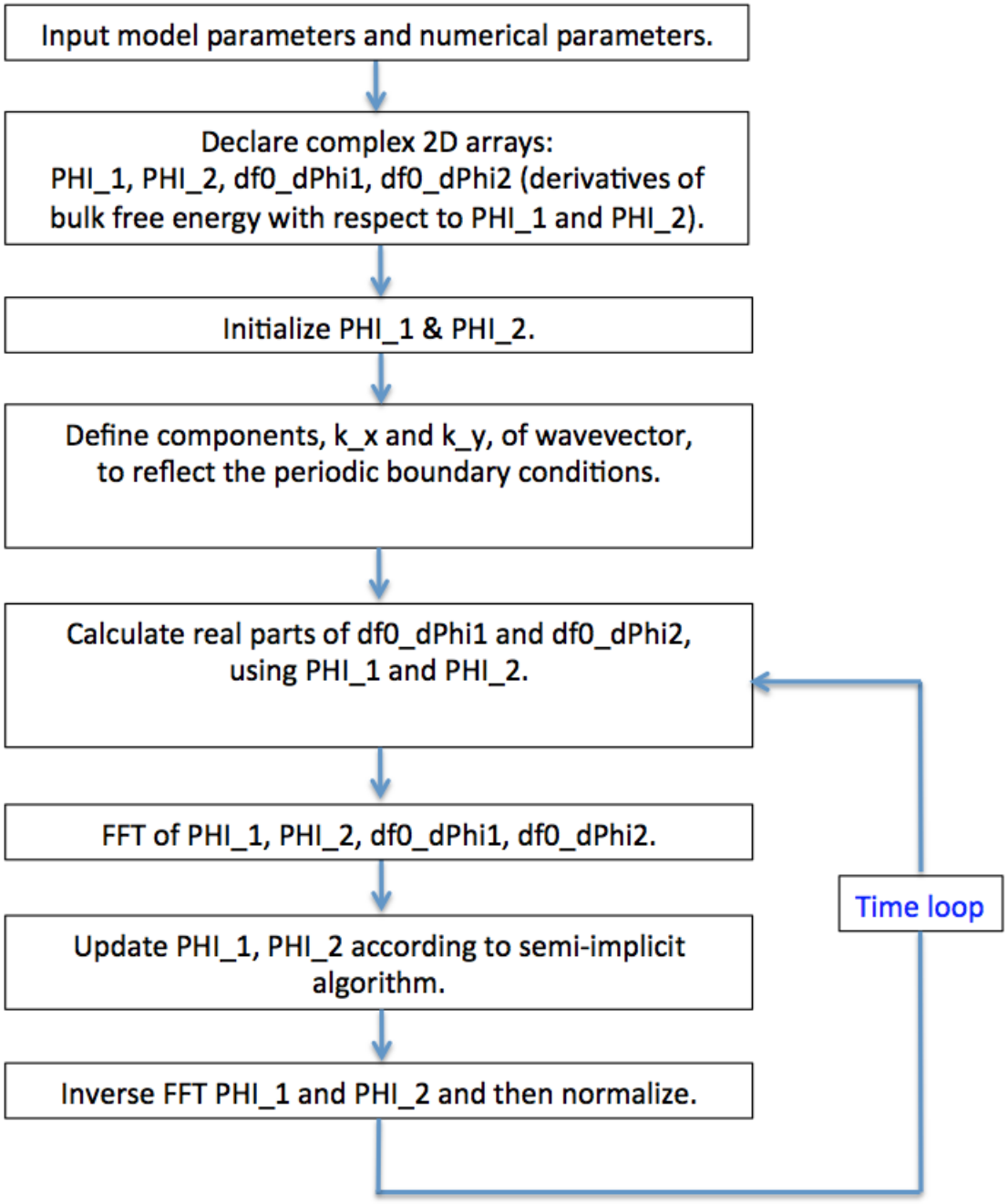


Figure 6.1: Structure of the code.

Unless stated otherwise, we begin each simulation with $\phi^0_{\text{blue}} = \phi^0_{\text{red}} = 0.15$ and $\phi^0_{\text{white}} = 0.7$, so that the red and blue components together occupy 30% of the domain. This allows us to observe the formation of particles, as opposed to the "snake-like" structures typically observed in solutions of the Cahn-Hilliard equation when the overall fractions of the components are similar to each other.

6.1 Dimensionless form of the Cahn-Hilliard equation

All simulations are carried out using the dimensionless form of the Cahn-Hilliard equations [68, 69]. Energy is scaled by a characteristic energy of $k_B T$, where k_B is the Boltzmann constant and T is the temperature. Thus,

$$\tilde{E} = \frac{E}{k_B T}\,, \tag{6.1}$$

where E is the energy, and $\tilde{E}$ is the dimensionless energy. Similarly, the dimensionless length, $\tilde{x}$, and dimensionless time, $\tilde{t}$, are given by

$$\tilde{x} = \frac{x}{l^*} \tag{6.2}$$

and

$$\tilde{t} = \frac{t}{t^*}\,, \tag{6.3}$$

respectively. Here, l^* is a characteristic length and t^* is a characteristic time. We may then rewrite equation 2.9 as

$$\tilde{F} = l^{*3} \int_V \left(\tilde{f}_0 + \frac{\kappa}{2k_B T} (\nabla \phi)^2 \right) \mathrm{d}\tilde{V} \,, \tag{6.4}$$

where a tilde appearing above a variable represents the dimensionless form of that variable. Similarly, the general form of the Cahn-Hilliard equation (equation 2.29) may be written as

$$\frac{\partial \phi}{\partial \tilde{t}} = \tilde{M} \tilde{\nabla}^2 \left(\frac{\partial f_0(\phi)}{\partial \phi} - \tilde{\kappa} \tilde{\nabla}^2 \phi \right) , \tag{6.5}$$

where

$$\tilde{\kappa} = \frac{\kappa}{2k_b T l^{*2}} \tag{6.6}$$

and

$$\tilde{M} = \frac{M t^* k_b T}{l^{*2}} \,, \tag{6.7}$$

are the dimensionless gradient energy coefficient and mobility respectively. Setting $\tilde{M} = 1$, the characteristic time, t^*, is then

$$t^* = \frac{M l^{*2}}{k_B T} \,. \tag{6.8}$$

The dimensionless regular solution parameter, $\tilde{\Omega}$, is given by

$$\tilde{\Omega} = \frac{\Omega}{k_B T} \,, \tag{6.9}$$

and is related to the gradient energy coefficient through the relation [32],

$$\tilde{\kappa} = \tilde{\Omega}\tilde{a}^2\,, \tag{6.10}$$

where $\tilde{a} = a/l^*$ is the dimensionless form of a, which is an interaction length, typically taken to be the interatomic distance [32]. We choose the characteristic length, $l^* = 1\text{nm}$. Unless stated otherwise, the length, l, of our square simulation domain is $2\sqrt{2}\pi\text{nm} \approx 8.9\text{nm}$. This is varied in section 6.6, to study the effect of an increased system size. In the following sections, for convenience, we drop the convention of using a tilde to denote a non-dimensional quantity.

6.2 Classification of particles

In order to quantitatively distinguish between centred and off-centred cores in our simulations of binary particles, we may calculate the positions of the centres of mass of the two constituent components using the following equa-

tions:

$$\begin{aligned}
\bar{x}_1 &= \frac{\sum_{i,j} \phi_1^{i,j} x^i}{\sum_{i,j} \phi_1^{i,j}} \\
\bar{y}_1 &= \frac{\sum_{i,j} \phi_1^{i,j} y^j}{\sum_{i,j} \phi_1^{i,j}} \\
\bar{x}_2 &= \frac{\sum_{i,j} \phi_2^{i,j} x^i}{\sum_{i,j} \phi_2^{i,j}} \\
\bar{y}_2 &= \frac{\sum_{i,j} \phi_2^{i,j} y^j}{\sum_{i,j} \phi_2^{i,j}} \,,
\end{aligned} \tag{6.11}$$

where $(\bar{x}_1, \bar{y}_1)$ and $(\bar{x}_2, \bar{y}_2)$ are the coordinates of the centres of mass of components 1 and 2 respectively, and where i and j represent the gridpoints in the x and y directions respectively. Using equation (6.11), we may then calculate the distance, d_{CM} between the centres of mass,

$$d_{\mathrm{CM}} = \sqrt{(\bar{y}_2 - \bar{y}_1)^2 + (\bar{x}_2 - \bar{x}_1)^2} \,, \tag{6.12}$$

along with the gradient, m_{CM}, of the line connecting the centres of mass of the two components:

$$m_{\mathrm{CM}} = \frac{\bar{y}_2 - \bar{y}_1}{\bar{x}_2 - \bar{x}_1} \,. \tag{6.13}$$

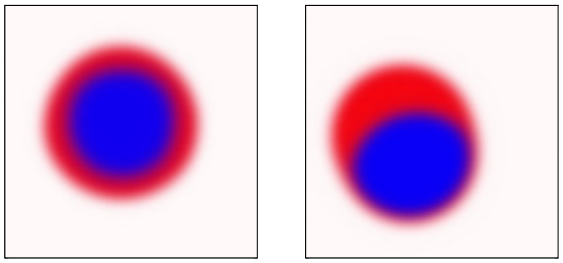
From this, we are able to calculate the length of the particle by extending the line connecting the centres of mass to opposite edges of the particle. The ratio of the distance between the centres of mass to the length of the particle then provides us with a suitable measure of how off-centred the core of the

particle is.

Let us define the parameter, $\delta_{\mathrm{off-centre}}$, such that

$$\delta_{\mathrm{off-centre}} = \frac{d_{\mathrm{CM}}}{L_{\mathrm{particle}}}\,, \tag{6.14}$$

where L_{particle} is the length of the particle. For a perfect, centred core-shell particle, $\delta_{\mathrm{off-centre}} = 0$, whereas for a fully off-centred core, $\delta_{\mathrm{off-centre}} = 0.5$. Figure 6.2 shows a core-shell and quasi-Janus particle with $\delta_{\mathrm{off-centre}} = 0.0683$ and $\delta_{\mathrm{off-centre}} = 0.0454$ respectively.



$\delta_{\mathrm{off-centre}} = 0.0683$ $\delta_{\mathrm{off-centre}} = 0.454$

Figure 6.2: $\delta_{\mathrm{off-centre}}$ for a core-shell and quasi-Janus particle.

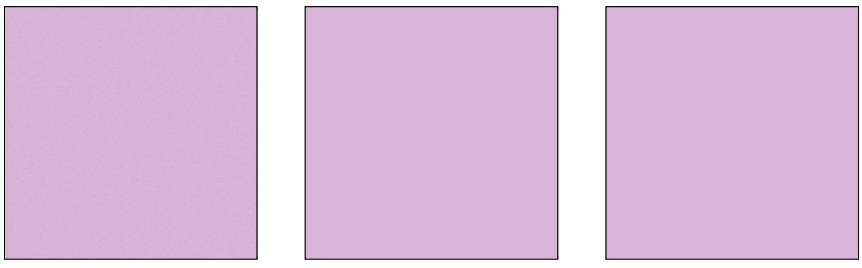
6.3 Varying regular solution parameters, Ω_{ij}

In the results presented in this chapter, components 1, 2 and 3 are represented by the colours blue, red and white respectively. In the case of the CuAg simulations, blue represents Cu, and red represents Ag, with white representing vacuum. It is thus convenient to refer to Ω_{12}, Ω_{23} and Ω_{13} as

$\Omega_{\text{blue-red}}$, $\Omega_{\text{red-white}}$ and $\Omega_{\text{blue-white}}$ respectively.

If all of the regular solution parameters, Ω_{ij}, are chosen to be below a certain value, phase separation will not occur, and the system will remain in its initial steady state. This is shown In figure 6.3, in which all of the Ω_{ij} are equal to 3.0, and phase separation is not seen. Similarly, if any one of the Ω_{ij} are too small, then phase separation between components i and j will not occur. This is shown in figure 6.4, in which $\Omega_{\text{blue-red}} = 2.0$, $\Omega_{\text{red-white}} = 3.5$ and $\Omega_{\text{blue-white}} = 3.5$, and separation between the red and blue components is not seen. On the other hand, if we set all Ω_{ij} equal to 3.5, then separation between all components is seen, and the steady-state shape of the final particle obtained is a dumbbell/Janus particle. This is shown in figure 6.5.

For the CuAg system, $\Omega_{\text{Cu-Ag}} < \Omega_{\text{Ag-Vac}} < \Omega_{\text{Cu-Vac}}$, i.e. the CuAg interfacial



$t = 0$ $t = 1.0$ $t = 10.0$

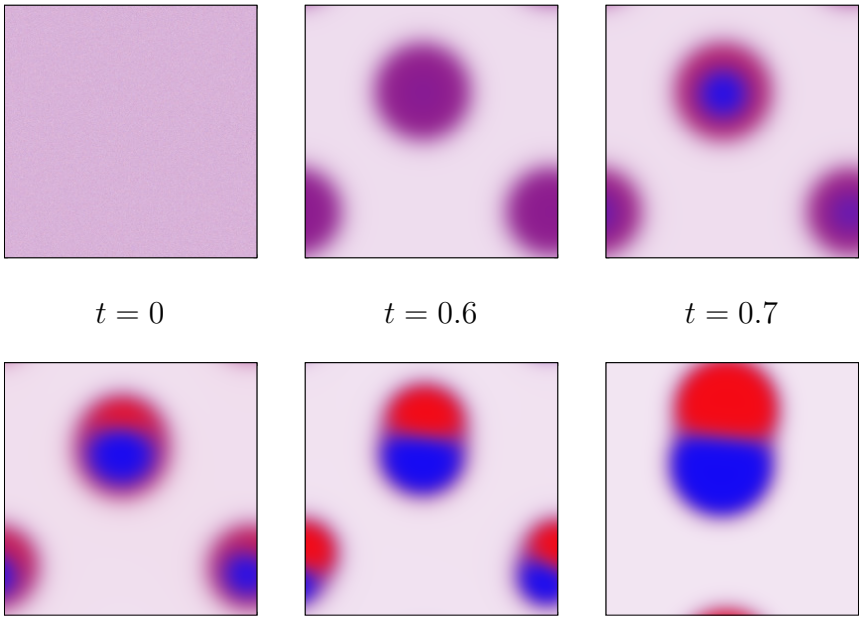
Figure 6.3: Numerical solution of the ternary Cahn-Hilliard equations with $\Omega_{\text{blue-red}} = 3.0, \Omega_{\text{red-white}} = 3.0, \Omega_{\text{blue-white}} = 3.0$, grid size: 128x128, $\Delta t = 1 \times 10^{-4}$.

energy is less than the surface energy of Ag, which is less than the surface



$t = 0$ $t = 0.5$ $t = 10.0$

Figure 6.4: Numerical solution of the ternary Cahn-Hilliard equations with $\Omega_{\text{blue}-\text{red}} = 2.0, \Omega_{\text{red}-\text{white}} = 3.5, \Omega_{\text{blue}-\text{white}} = 3.5$, grid size: 128x128, $\Delta t = 1 \times 10^{-4}$.



$t = 0$ $t = 0.6$ $t = 0.7$

$t = 0.8$ $t = 0.9$ $t = 10$

Figure 6.5: Numerical solution of the ternary Cahn-Hilliard equations with $\Omega_{\text{blue}-\text{red}} = 3.5, \Omega_{\text{red}-\text{white}} = 3.5, \Omega_{\text{blue}-\text{white}} = 3.5$, grid size: 256×256, $\Delta t = 1 \times 10^{-4}$.

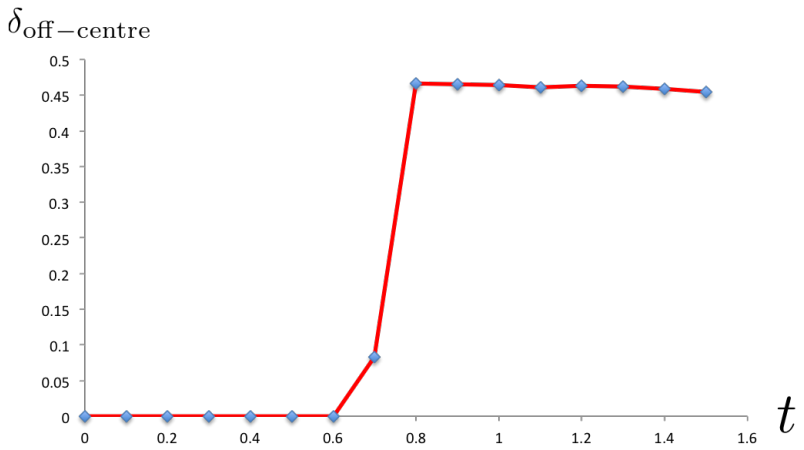


Figure 6.6: Variation of $\delta_{\text{off}-\text{centre}}$ with dimensionless time, t. The graph corresponds to the simulation shown in figure 6.5.

energy of Cu. In order to simulate core-shell particles, we therefore choose $\Omega_{\text{blue}-\text{red}} < \Omega_{\text{red}-\text{white}} < \Omega_{\text{blue}-\text{white}}$. $\Omega_{\text{blue}-\text{red}}$ is chosen to be large enough to induce phase separation between the blue and red components. Choosing higher $\Omega_{\text{blue}-\text{red}}$ while maintaining the same ratios, $\Omega_{\text{blue}-\text{white}} : \Omega_{\text{blue}-\text{red}}$ and $\Omega_{\text{red}-\text{white}} : \Omega_{\text{blue}-\text{red}}$, leads to qualitatively similar results. The problem, however, with using higher regular solution parameters is that it amplifies the stiffness in the numerical solution caused by the *nonlinear* term. It therefore becomes necessary to use significantly smaller time steps, and simulations take a long time to reach the steady state.

Figure 6.7 shows snapshots from a simulation in which the dimensionless regular solution parameters are given by $\Omega_{\text{blue}-\text{red}} = 3.0$, $\Omega_{\text{red}-\text{white}} = 3.5$ and $\Omega_{\text{blue}-\text{white}} = 4.0$. In the initial stages of the simulation, the white component separates from the red and blue components due to the fact that $\Omega_{\text{blue}-\text{white}}$ and $\Omega_{\text{red}-\text{white}}$ are greater than $\Omega_{\text{blue}-\text{red}}$. This leads to the formation of par-

ticles containing a mixture of blue and red components. Following on from this, the blue and red components separate, forming core-shell particles. The blue component occupies the core, since $\Omega_{\text{blue-white}} > \Omega_{\text{red-white}}$, and the red component, therefore, has a lower surface energy than the blue component. With increasing time, we see the Ostwald ripening phenomenon taking place, whereby larger particles grow at the expense of smaller ones. Finally, as the particles coarsen and coalesce to form a single large particle in the steady state, we see a transition from small core-shell structures to a larger quasi-Janus structure. A thin layer of red is observed on the outside of the blue side of the particle.

Figure 6.8 shows the steady-state solutions obtained for varying $\Omega_{\text{blue-white}}$, while $\Omega_{\text{blue-red}} = 3.0$ and $\Omega_{\text{red-white}} = 4.0$ are fixed. In figure 6.8a, $\Omega_{\text{blue-white}} = 4.0$, and the steady-state solution is a quasi-Janus particle. Owing to the fact that $\Omega_{\text{blue-white}} = \Omega_{\text{red-white}}$, we see a flat red-blue interface. As $\Omega_{\text{blue-white}}$ is steadily increased through figures 6.8b– 6.8e, however, we see that the red-blue interface becomes curved, and that its curvature increases with increasing $\Omega_{\text{blue-white}}$. Figures 6.8b and 6.8c, in which $\Omega_{\text{blue-white}}$ is 4.5 and 5.0 respectively, show that a quasi-Janus particle is still the lowest energy configuration. For $\Omega_{\text{blue-white}} = 5.5$ (figure 6.8d), however, quasi-Janus particles are not observed, and the final particle obtained is core-shell. Moreover, if we increase $\Omega_{\text{blue-white}}$ further, as in figures 6.8e and 6.8f, where $\Omega_{\text{blue-white}}$ is 6.0 and 6.5 respectively, while keeping $\Omega_{\text{red-white}}$ and $\Omega_{\text{red-blue}}$ fixed, we obtain similar results, with a core-shell arrangement as the lowest energy configuration. This is to be expected, since increasing $\Omega_{\text{blue-white}}$ increases

the surface energy of the blue component, and it is therefore less likely to migrate towards the surface.

Figure 6.9 shows the variation of $\delta_{\text{off-centre}}$ with $\Omega_{\text{blue-white}}$ for the steady-state solutions shown in figure 6.8. A series of snapshots of the simulations used to obtain the steady-state solutions in figure 6.8 are shown in figures 6.10, 6.11, 6.12, 6.13, 6.14 and 6.15, corresponding to $\Omega_{\text{blue-white}} = 4.0$, $\Omega_{\text{blue-white}} = 4.5$, $\Omega_{\text{blue-white}} = 5.0$, $\Omega_{\text{blue-white}} = 5.5$, $\Omega_{\text{blue-white}} = 6.0$ and $\Omega_{\text{blue-white}} = 6.5$ respectively.

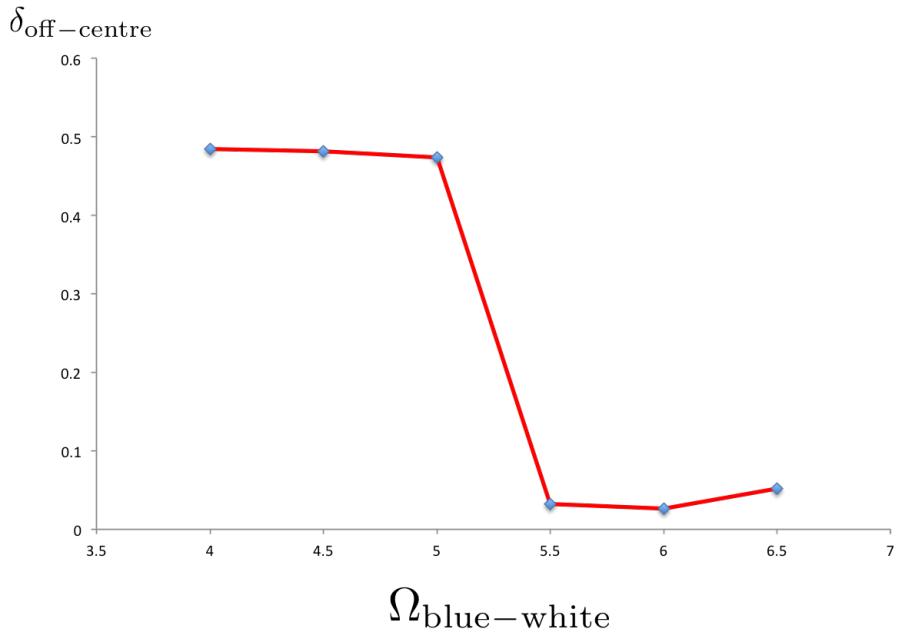


Figure 6.9: Variation of $\delta_{\text{off-centre}}$ with $\Omega_{\text{blue-white}}$ for fixed $\Omega_{\text{blue-red}} = 3.0$ and $\Omega_{\text{red-white}} = 4.0$.

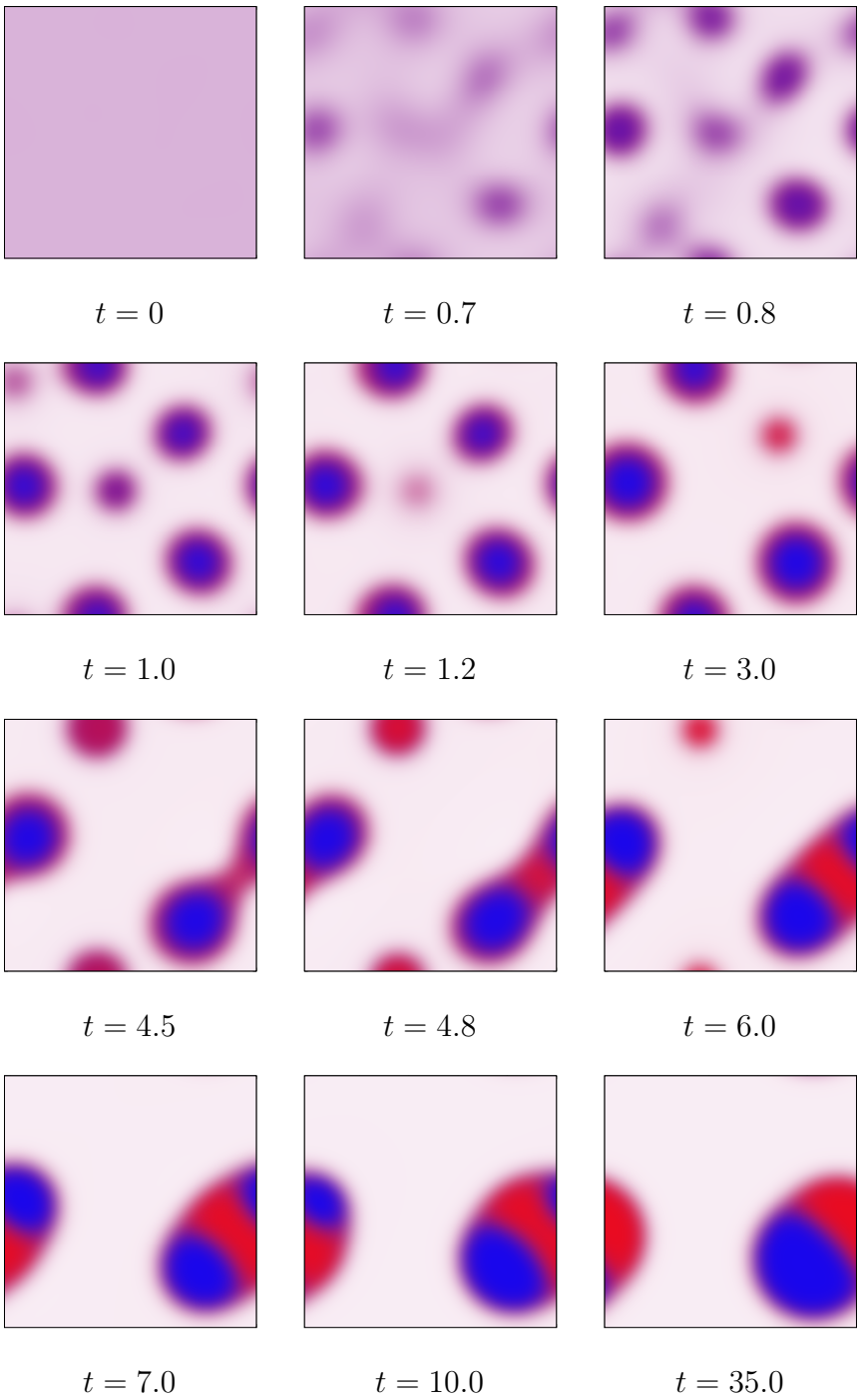
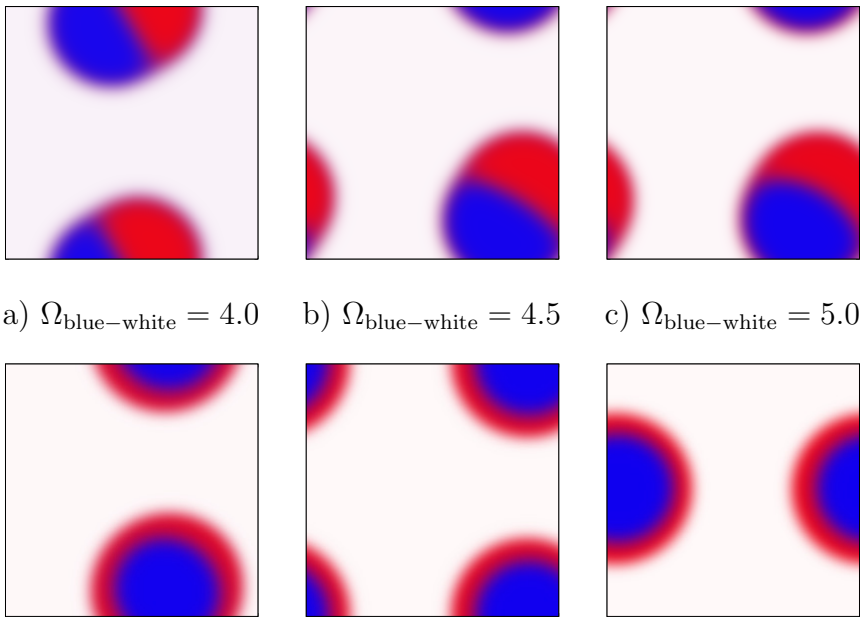


Figure 6.7: Numerical solution of the ternary Cahn-Hilliard equations with $\Omega_{\text{blue}-\text{red}} = 3.0, \Omega_{\text{red}-\text{white}} = 3.5, \Omega_{\text{blue}-\text{white}} = 4.0$, grid size: 256×256, $\Delta t = 1 \times 10^{-5}$.



a) $\Omega_{\text{blue}-\text{white}} = 4.0$ b) $\Omega_{\text{blue}-\text{white}} = 4.5$ c) $\Omega_{\text{blue}-\text{white}} = 5.0$

d) $\Omega_{\text{blue}-\text{white}} = 5.5$ $\Omega_{\text{blue}-\text{white}} = 6.0$ $\Omega_{\text{blue}-\text{white}} = 6.5$

Figure 6.8: Steady-state solutions obtained for $\Omega_{\text{blue}-\text{red}} = 3.0$ and $\Omega_{\text{red}-\text{white}} = 4.0$, while increasing $\Omega_{\text{blue}-\text{white}}$ from fig. a) to fig. f)

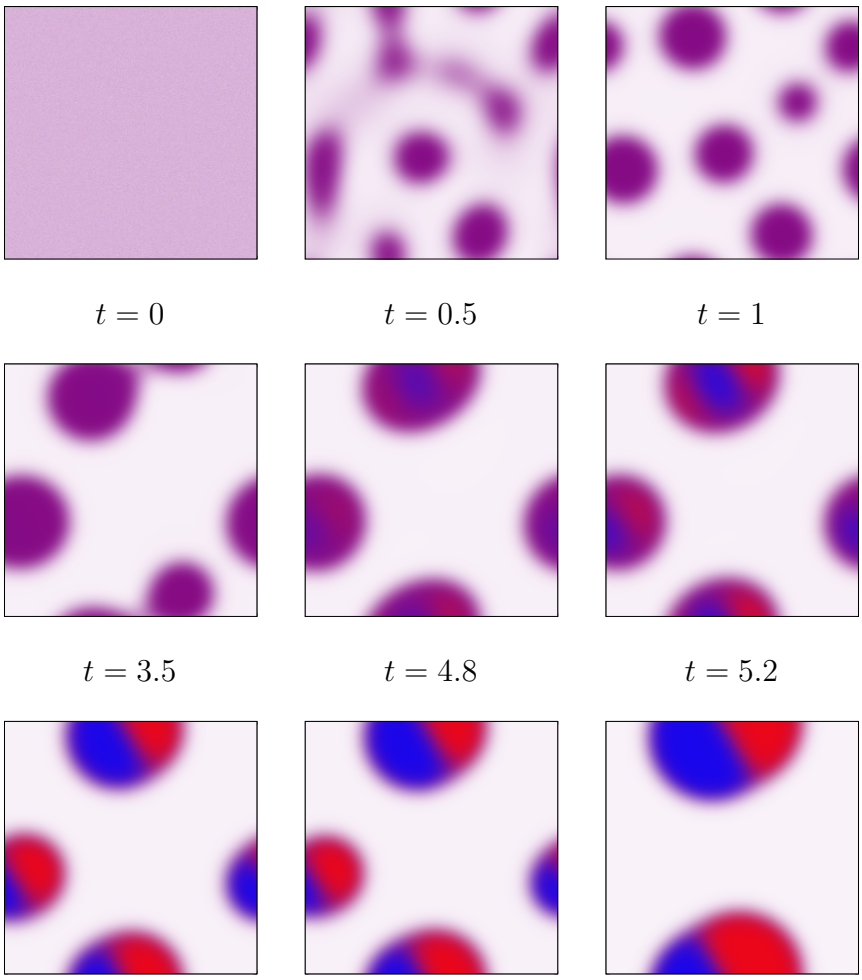


Figure 6.10: Numerical solution of the ternary Cahn-Hilliard equations with $\Omega_{\text{blue}-\text{red}} = 3.0, \Omega_{\text{red}-\text{white}} = 4.0, \Omega_{\text{blue}-\text{white}} = 4.0$, grid size: 256×256, $\Delta t = 1 \times 10^{-5}$.

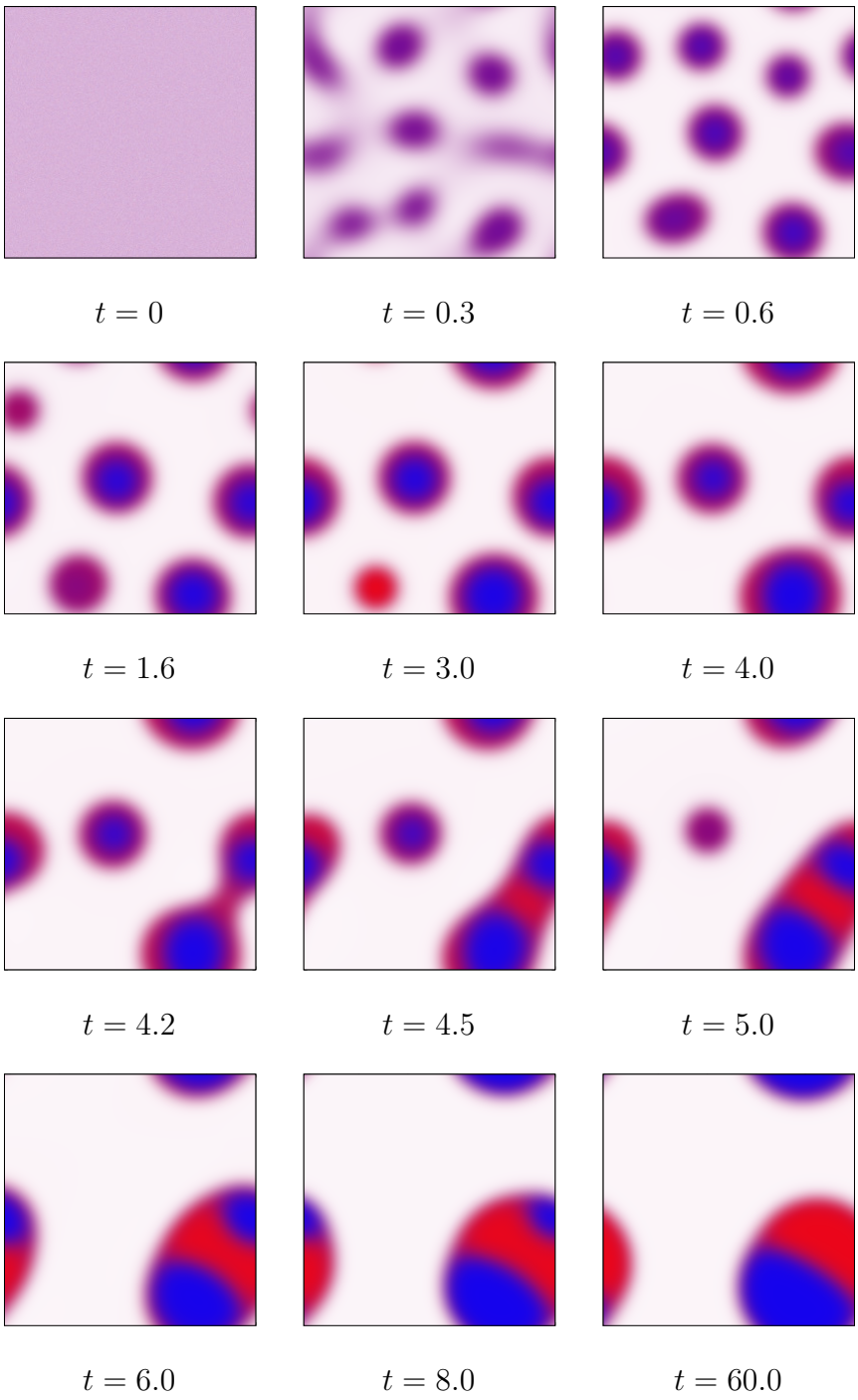


Figure 6.11: Numerical solution of the ternary Cahn-Hilliard equations with $\Omega_{\text{blue}-\text{red}} = 3.0, \Omega_{\text{red}-\text{white}} = 4.0, \Omega_{\text{blue}-\text{white}} = 4.5$, grid size: 256×256, $\Delta t = 1 \times 10^{-5}$.

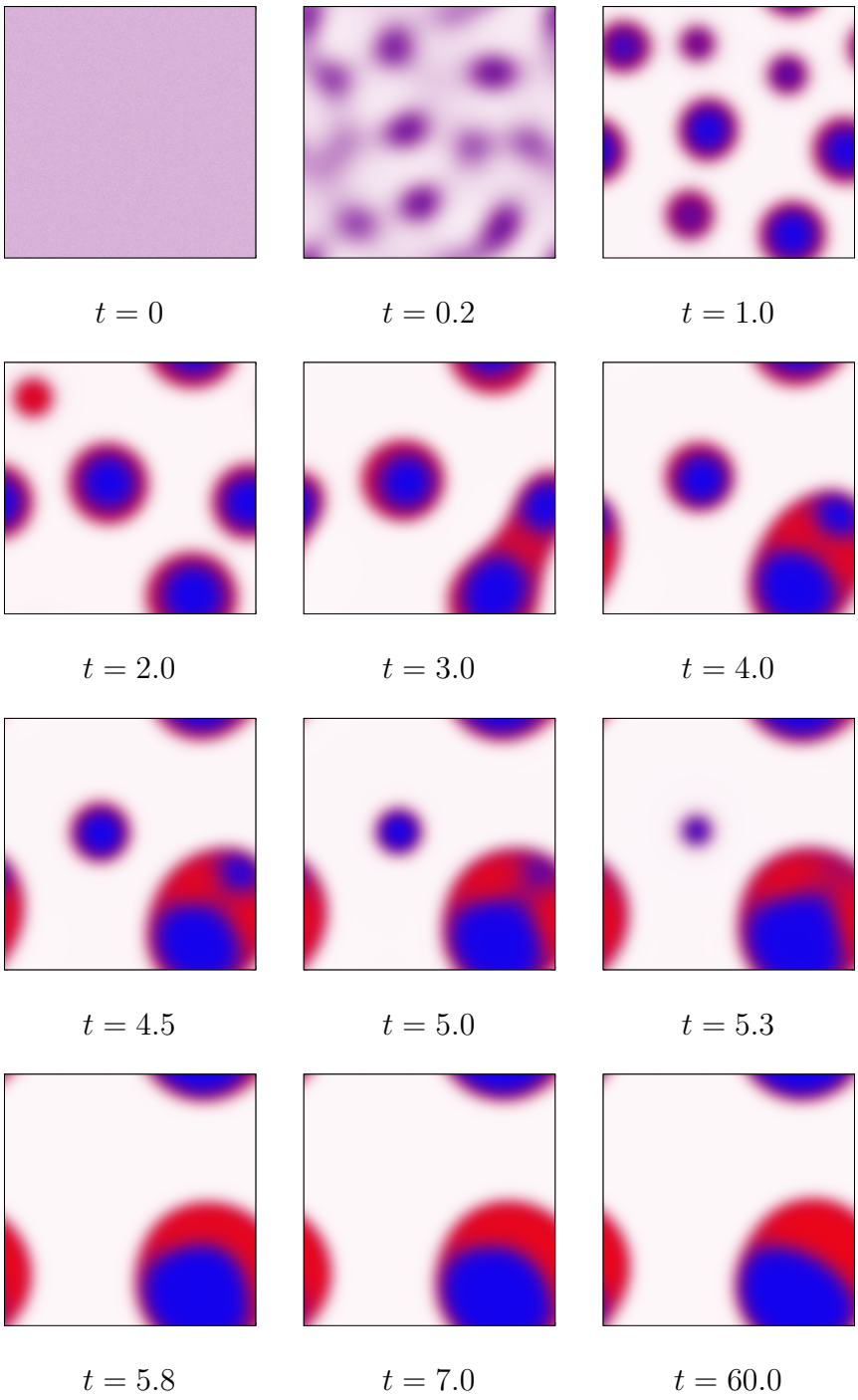


Figure 6.12: Numerical solution of the ternary Cahn-Hilliard equations with $\Omega_{\text{blue}-\text{red}} = 3.0, \Omega_{\text{red}-\text{white}} = 4.0, \Omega_{\text{blue}-\text{white}} = 5.0$, grid size: 256×256, $\Delta t = 1 \times 10^{-5}$.

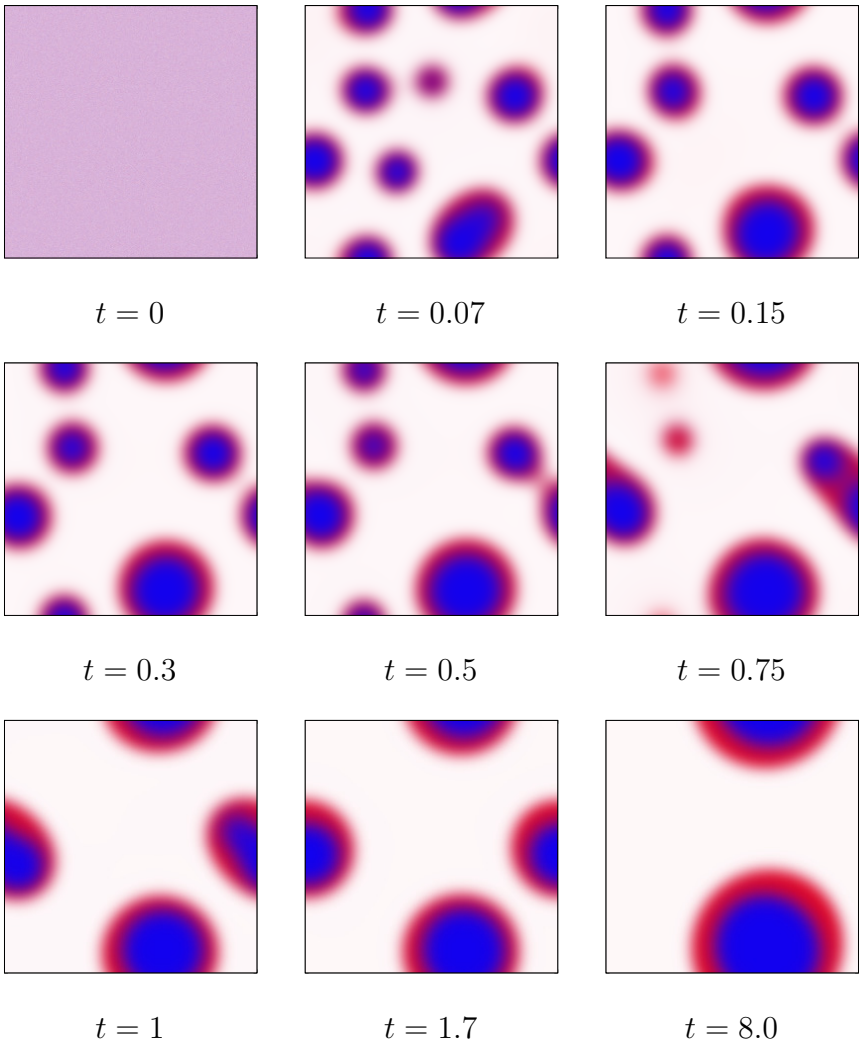


Figure 6.13: Numerical solution of the ternary Cahn-Hilliard equations with $\Omega_{\text{blue}-\text{red}} = 3.0, \Omega_{\text{red}-\text{white}} = 4.0, \Omega_{\text{blue}-\text{white}} = 5.5$, grid size: 256×256, $\Delta t = 1 \times 10^{-6}$.

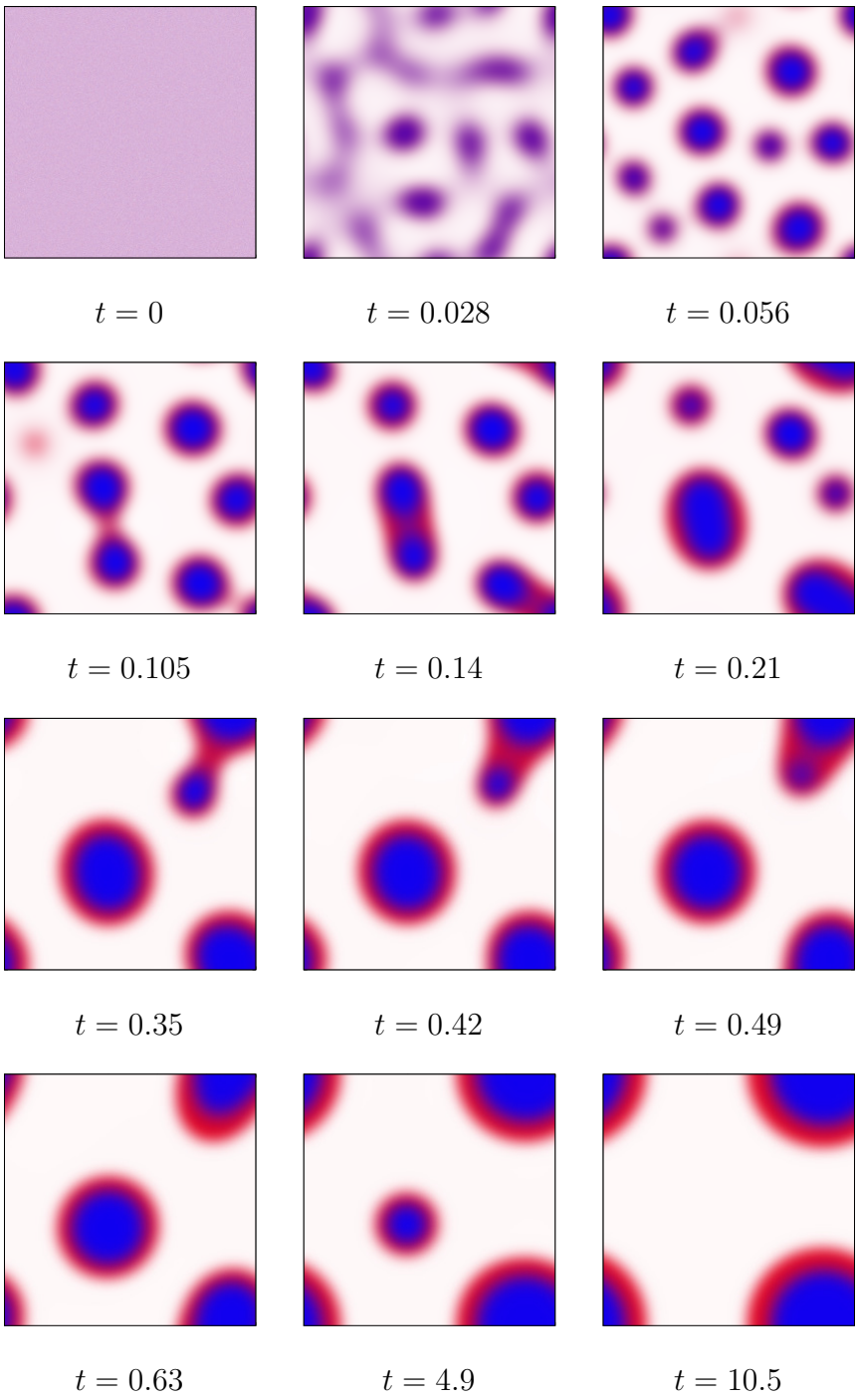


Figure 6.14: Numerical solution of the ternary Cahn-Hilliard equations with $\Omega_{\text{blue}-\text{red}} = 3.0, \Omega_{\text{red}-\text{white}} = 4.0, \Omega_{\text{blue}-\text{white}} = 6.0$, grid size: 256×256, $\Delta t = 7 \times 10^{-7}$.

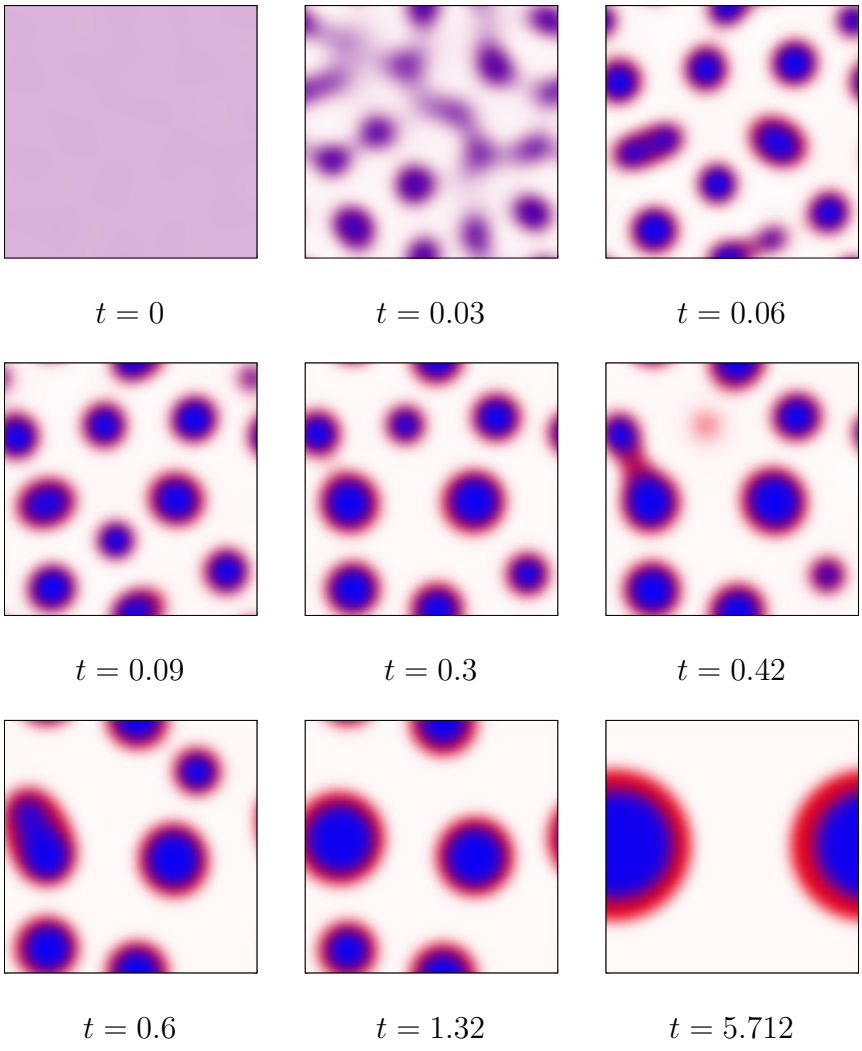


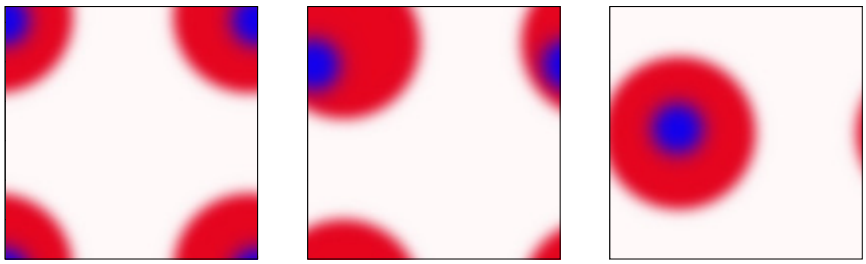
Figure 6.15: Numerical solution of the ternary Cahn-Hilliard equations with $\Omega_{\text{blue}-\text{red}} = 3.0, \Omega_{\text{red}-\text{white}} = 4.0, \Omega_{\text{blue}-\text{white}} = 6.5$, grid size: 256×256, $\Delta t = 6 \times 10^{-7}$.

6.4 Varying composition

It has been shown, in experiments [11] and simulations [28, 29], that the size of the core has an effect on the morphology of the particles obtained. Figure 6.16 shows steady-state solutions obtained using a decreased core size, such that the blue : red particle composition ratio is 20 : 80. All other parameters are fixed, and we use $\Omega_{\text{blue}-\text{red}} = 3.0$, $\Omega_{\text{red}-\text{white}} = 4.0$ and $\Omega_{\text{blue}-\text{white}} = 6.0$, as in figure 6.14, in which case it has already been shown that, for a 50 : 50 blue : red ratio, a core-shell particle is the most stable structure. Figures 6.16 a), 6.16 b) and 6.16 c) show that the placement of the core is, in fact, random, with $\delta_{\text{off}-\text{centre}} = 0.072$, $\delta_{\text{off}-\text{centre}} = 0.336$ and $\delta_{\text{off}-\text{centre}} = 0.039$ respectively. The corresponding dimensionless, total interfacial energies are equal to 3.570, 3.56324 and 3.5692 respectively, suggesting that these structures are energetically equivalent.

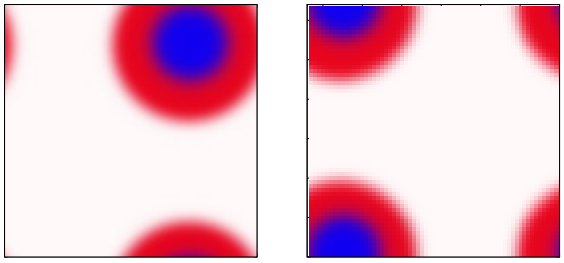
Similar results to those shown in figure 6.16 are shown in figures 6.17 – 6.20, in which the blue : red composition ratio is increased from 30 : 70 through to 60 : 40. In each case, the core remains fully contained within a shell of the red component, while the position of the core is random. As the shell thickness decreases, the particles become more centred.

Let us now consider the simulation shown in figure 6.12 for $\Omega_{\text{blue}-\text{red}} = 3.0$, $\Omega_{\text{red}-\text{white}} = 4.0$, $\Omega_{\text{blue}-\text{white}} = 5.0$. In this case, the steady-state solution is a quasi-Janus particle. By varying the blue : red composition ratio, we find that a quasi-Janus particle is obtained as the steady-state solution in each



a) $\delta_{\text{off}-\text{centre}} = 0.072$ b) $\delta_{\text{off}-\text{centre}} = 0.336$ c) $\delta_{\text{off}-\text{centre}} = 0.039$

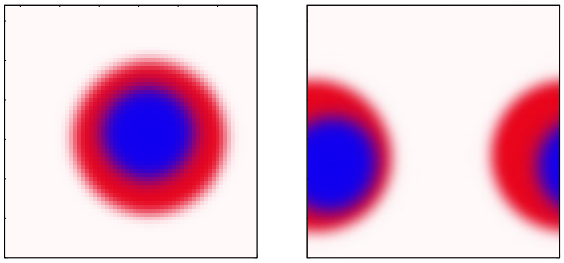
Figure 6.16: Steady-state solutions obtained for a blue : red ratio of 20 : 80. $\Omega_{\text{blue}-\text{red}} = 3.0$, $\Omega_{\text{red}-\text{white}} = 4.0$, $\Omega_{\text{blue}-\text{white}} = 6.0$.



a) $\delta_{\text{off}-\text{centre}} = 0.031$ b) $\delta_{\text{off}-\text{centre}} = 0.065$

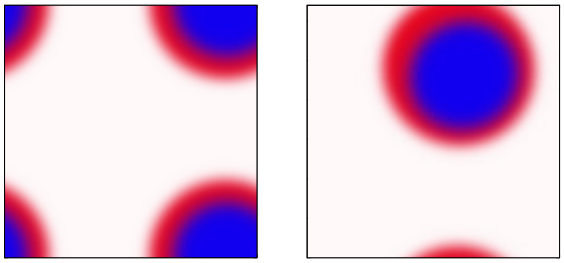
Figure 6.17: Steady-state solutions obtained for a blue : red ratio of 30 : 70. $\Omega_{\text{blue}-\text{red}} = 3.0$, $\Omega_{\text{red}-\text{white}} = 4.0$, $\Omega_{\text{blue}-\text{white}} = 6.0$.

case, except when the shell of the particle becomes too thin, in which case, core-shell particles are observed. steady-state solutions for varying blue : red ratios are shown in figure 6.21. The results we obtain are in accordance with experimental evidence [12] which suggests that Janus particles are not observed if the shell of the particle is too thin.



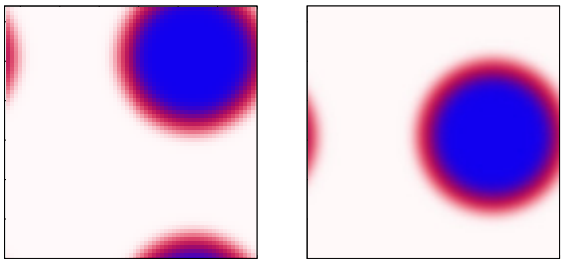
a) $\delta_{\text{off}-\text{centre}} = 0.083$ b) $\delta_{\text{off}-\text{centre}} = 0.335$

Figure 6.18: Steady-state solutions obtained for a blue : red ratio of 40 : 60. $\Omega_{\text{blue}-\text{red}} = 3.0$, $\Omega_{\text{red}-\text{white}} = 4.0$, $\Omega_{\text{blue}-\text{white}} = 6.0$.



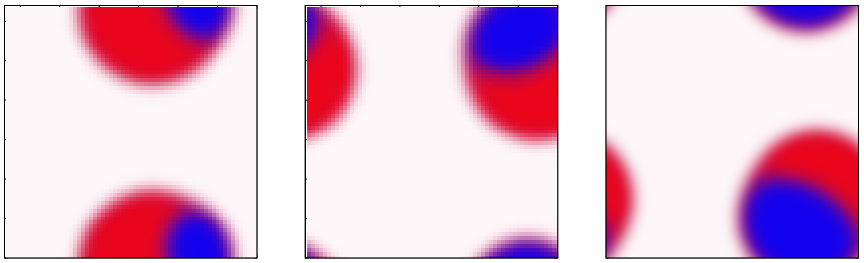
a) $\delta_{\text{off}-\text{centre}} = 0.063$ b) $\delta_{\text{off}-\text{centre}} = 0.196$

Figure 6.19: Steady-state solutions obtained for a blue : red ratio of 50 : 50. $\Omega_{\text{blue}-\text{red}} = 3.0$, $\Omega_{\text{red}-\text{white}} = 4.0$, $\Omega_{\text{blue}-\text{white}} = 6.0$.



a) $\delta_{\text{off-centre}} = 0.008$ b) $\delta_{\text{off-centre}} = 0.002$

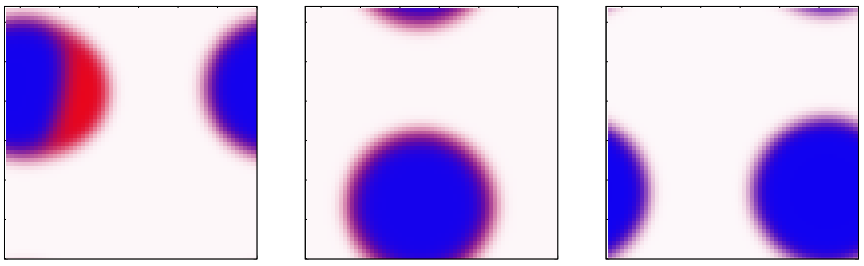
Figure 6.20: Steady-state solutions obtained for a blue : red ratio of 60 : 40. $\Omega_{\text{blue-red}} = 3.0$, $\Omega_{\text{red-white}} = 4.0$, $\Omega_{\text{blue-white}} = 6.0$.



a) 30 : 70
$\delta_{\text{off-centre}} = 0.437$

b) 40 : 60
$\delta_{\text{off-centre}} = 0.434$

c) 50 : 50
$\delta_{\text{off-centre}} = 0.447$



d) 60 : 40
$\delta_{\text{off-centre}} = 0.457$

e) 70 : 30
$\delta_{\text{off-centre}} = 0.004$

f) 80 : 20
$\delta_{\text{off-centre}} = 0.003$

Figure 6.21: steady-state solutions obtained for varying blue : red ratios, going from 30 : 70 in a) to 80 : 20 in f). Blue and red together occupy 30% of the system. $\Omega_{\text{blue-red}} = 3.0$, $\Omega_{\text{red-white}} = 4.0$, $\Omega_{\text{blue-white}} = 5.0$.

6.5 Elastic effects

The elastic effects caused by a lattice mismatch between the constituent components of a particle are included in the model via a coupling of the ternary Cahn-Hilliard equations with the Navier-Lamé equations of elasticity (see section 5). In the ternary systems that are simulated, elastic effects are only considered between the blue and red components.

Figures 6.22—6.25 show the effect of misfit strain on the core-shell to quasi-Janus particle transition. The blue:red composition ratio is 50:50, and $\Omega_{\text{red-blue}} = 3.0$, $\Omega_{\text{blue-white}} = 4.0$ and $\Omega_{\text{red-white}} = 6.0$. Thus, apart from the addition of elastic effects, all parameters are the same as those used to obtain figure 6.14. As seen previously, this set of parameters leads to the formation of core-shell particles, but does not lead to the formation of Janus/quasi-Janus particles.

For the simulations presented in this section, we use the elastic constants of the CuAg system, and vary the misfit. For Ag, $C_{11} = 132$GPa, $C_{12} = 97$GPa and $C_{44} = 51$GPa, whereas for Cu, we have $C_{11} = 176$GPa, $C_{12} = 125$GPa and $C_{44} = 82$GPa [70]. In figures 6.22, 6.23 and 6.25, the lattice misfit is 5%, 10% and 15% respectively. For 5% misfit, we see that the results are not dissimilar to those obtained without elasticity (figure 6.14), and the effects of elasticity are not visible. When the misfit is increased to 10%, however, the elastic effects are more pronounced. In the initial stages of the simulation, small core-shell particles are observed. However, as the simulation progresses, the particle core becomes off-centred, and we eventually see a

transition from core-shell structure to quasi-Janus particle structure. In the case of 15% lattice mismatch, quasi-Janus structures are observed even at small particle sizes, and there is a large deformation in the shapes of the particles as they coarsen.

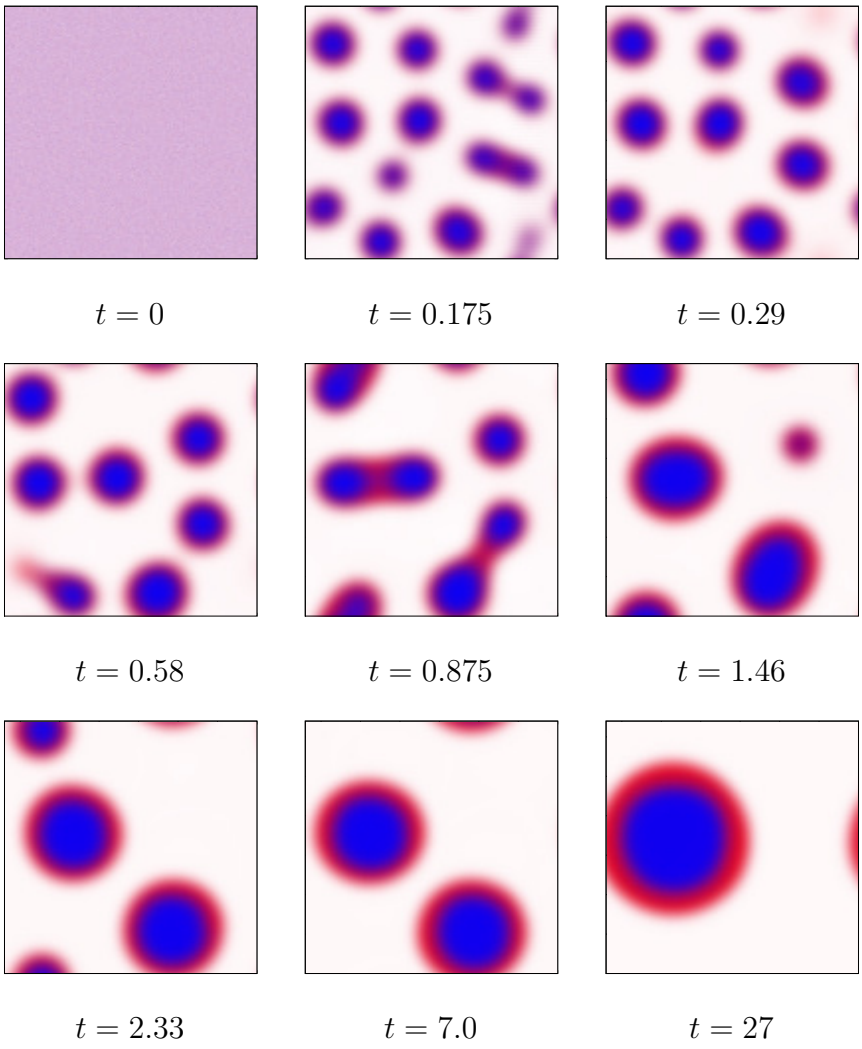


Figure 6.22: Simulation with 5% lattice mismatch included; $\Omega_{\text{blue}-\text{red}} = 3.0, \Omega_{\text{red}-\text{white}} = 4.0, \Omega_{\text{blue}-\text{white}} = 6.0$; grid size: 128×128, $\Delta t = 5 \times 10^{-7}$.

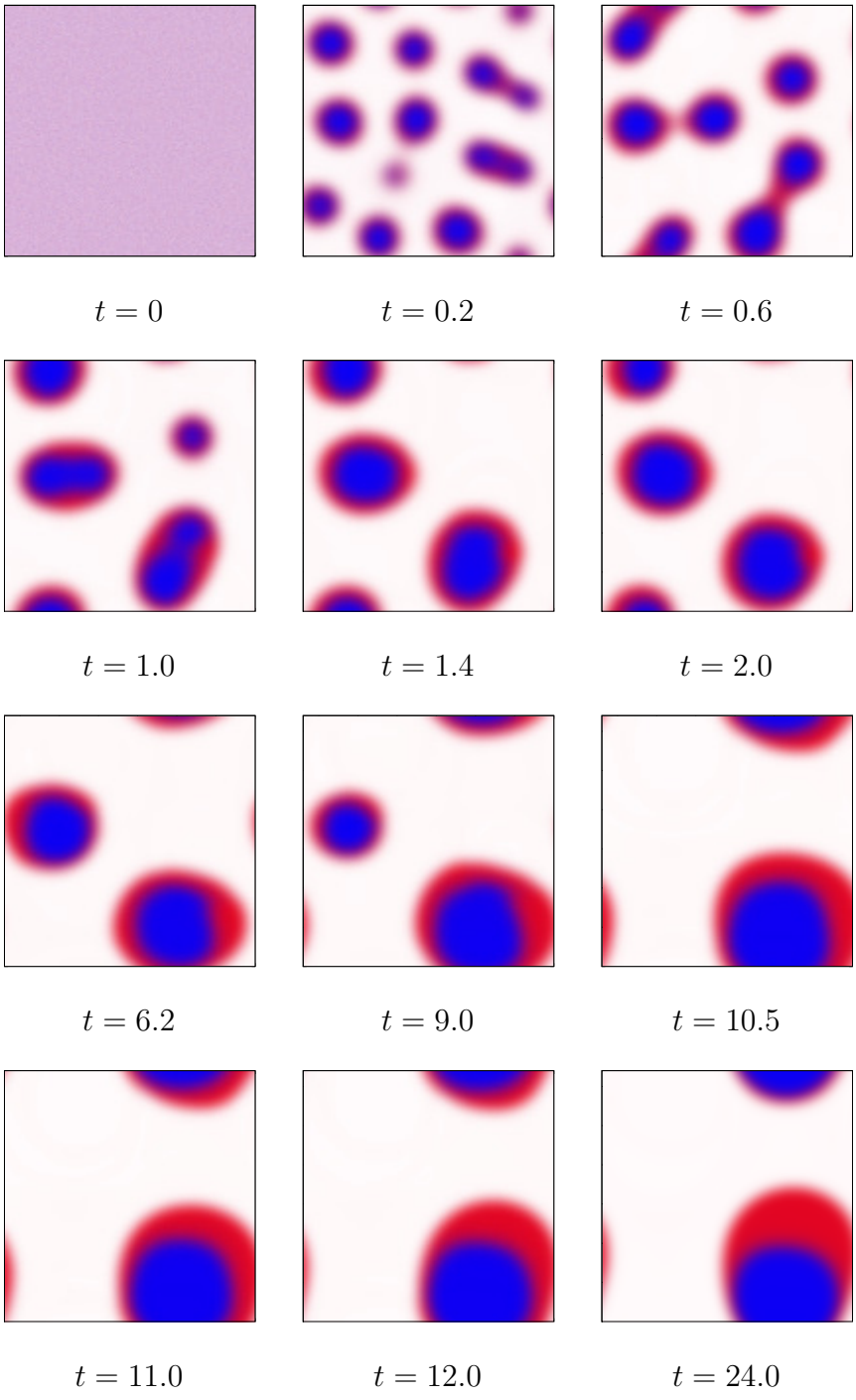
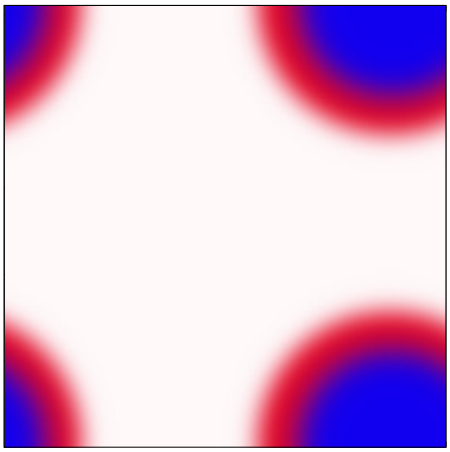
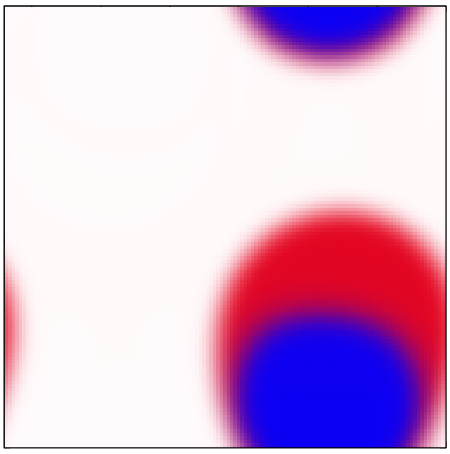


Figure 6.23: Simulation with 10% lattice mismatch included; $\Omega_{\text{blue}-\text{red}} = 3.0, \Omega_{\text{red}-\text{white}} = 4.0, \Omega_{\text{blue}-\text{white}} = 6.0$; grid size: 128×128, $\Delta t = 5 \times 10^{-7}$.



a) Without misfit



b) 10% misfit

Figure 6.24: Comparison of steady-state solutions obtained for $\Omega_{\text{blue}-\text{red}} = 3.0, \Omega_{\text{red}-\text{white}} = 4.0, \Omega_{\text{blue}-\text{white}} = 6.0$, a) without elasticity, b) with 10% misfit.

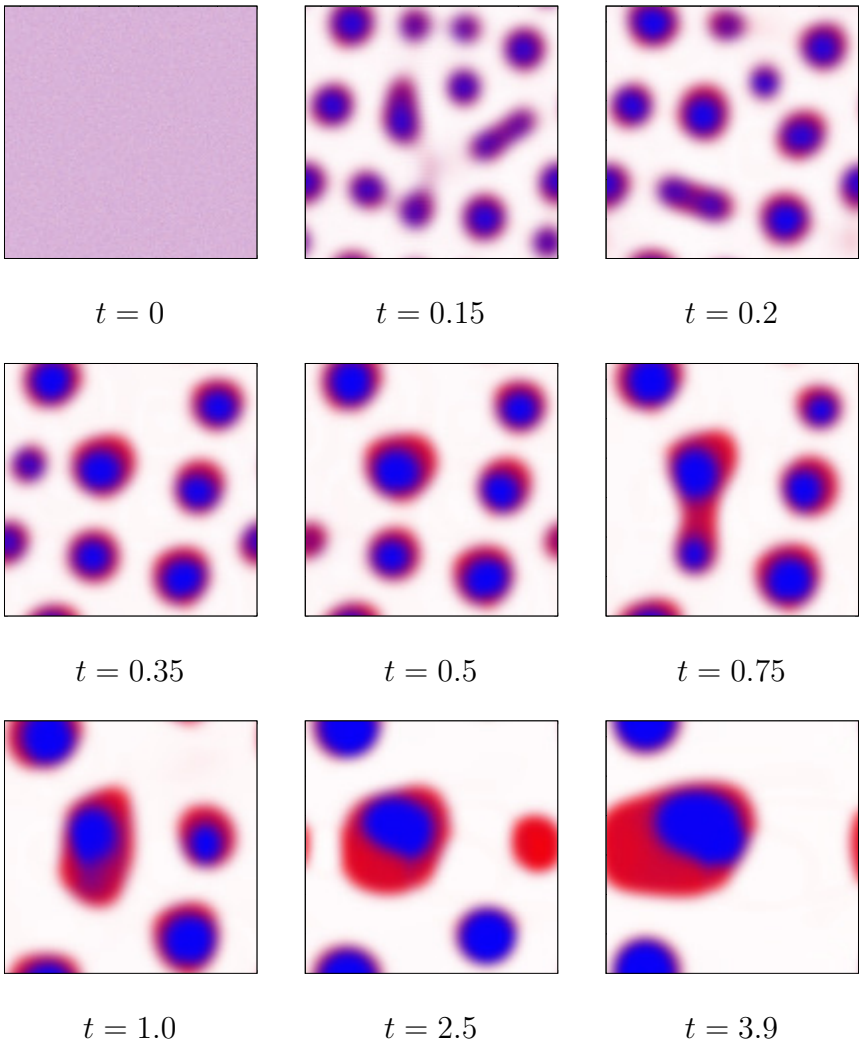


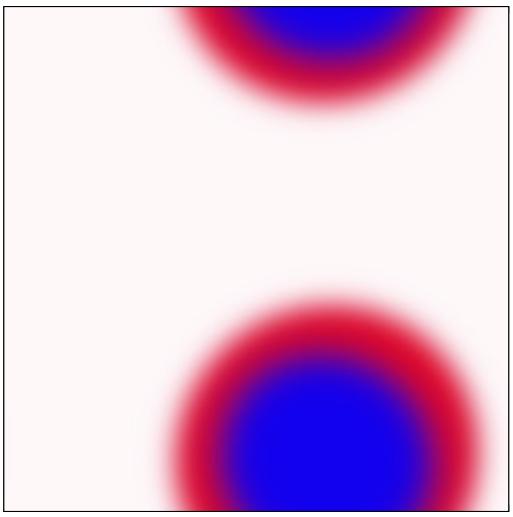
Figure 6.25: Simulation with 15% lattice mismatch included; $\Omega_{\text{blue}-\text{red}} = 3.0, \Omega_{\text{red}-\text{white}} = 4.0, \Omega_{\text{blue}-\text{white}} = 6.0$; grid size: 128×128, $\Delta t = 1 \times 10^{-8}$.

6.6 Varying size

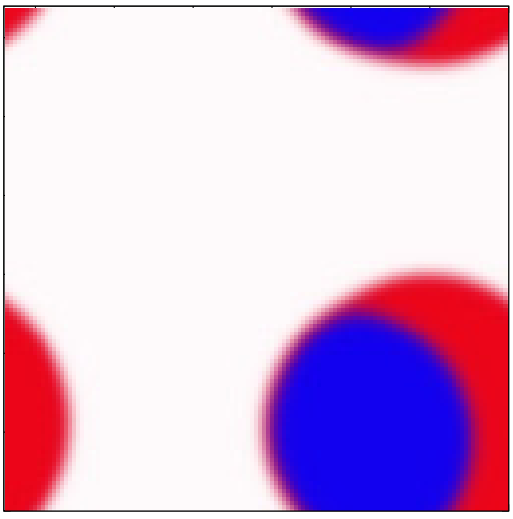
For bimetallic nanoparticles of weakly miscible metals, such as CuAg, it has been observed in experiments [12, 11, 14] and computer simulations [12, 28, 29] that, as the size of the nanoparticle increases, there is a transition from core-shell structures to quasi-Janus particle structures. We have already seen this effect in the simulation results that have been presented thus far in this chapter, with the initial stages of simulations showing core-shell particles, while Janus particles are seen in the latter stages, as the particles grow. In figure 6.13, however, a core-shell particle is obtained in the steady-state.

In figure 6.26 a), a steady-state solution is shown for the case of $\Omega_{\text{blue}-\text{red}} = 3.0$, $\Omega_{\text{red}-\text{white}} = 4.0$ and $\Omega_{\text{blue}-\text{white}} = 5.5$, as in figure 6.13, with the final particle morphology being core-shell. However, in figure 6.26 b), the length of the square simulation domain is increased by a factor of two, such that the length is changed from $2\sqrt{2}\pi$nm to $4\sqrt{2}\pi$nm. In this case, the emergence of quasi-Janus particles is seen, both during the evolution and in the steady-state. The time evolution of the system is shown in figure 6.27.

Conversely, if $\Omega_{\text{blue}-\text{red}} = 3.0$, $\Omega_{\text{red}-\text{white}} = 4.0$ and $\Omega_{\text{blue}-\text{white}} = 5.0$, we have seen, in figure 6.12, that quasi-Janus particles are preferred. However, if we decrease the system by a factor of two in each dimension, Janus/quasi-Janus particles are not seen, and core-shell is the most stable configuration, as shown in figure 6.28.



a) Domain length = $2\sqrt{2}\pi$nm = 8.89nm



b) Domain length = $4\sqrt{2}\pi$nm = 17.77nm

Figure 6.26: steady-state solutions for $\Omega_{\text{blue}-\text{red}} = 3.0, \Omega_{\text{red}-\text{white}} = 4.0, \Omega_{\text{blue}-\text{white}} = 5.5$. The domain length in b) is double that in a).

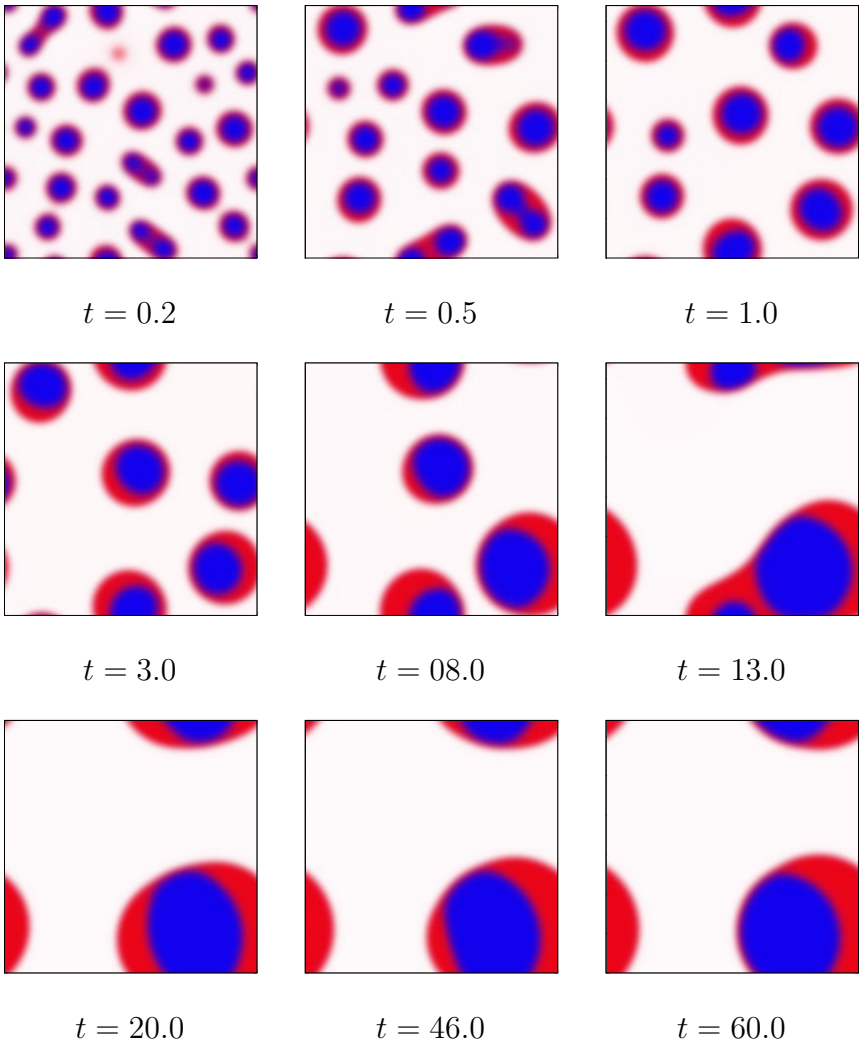


Figure 6.27: $\Omega_{\text{blue}-\text{red}} = 3.0, \Omega_{\text{red}-\text{white}} = 4.0, \Omega_{\text{blue}-\text{white}} = 5.5$, domain length $= 4\sqrt{2}\pi$nm (double that used in figure 6.13); grid size $= 256 \times 256$, $\Delta t = 1 \times 10^{-6}$.

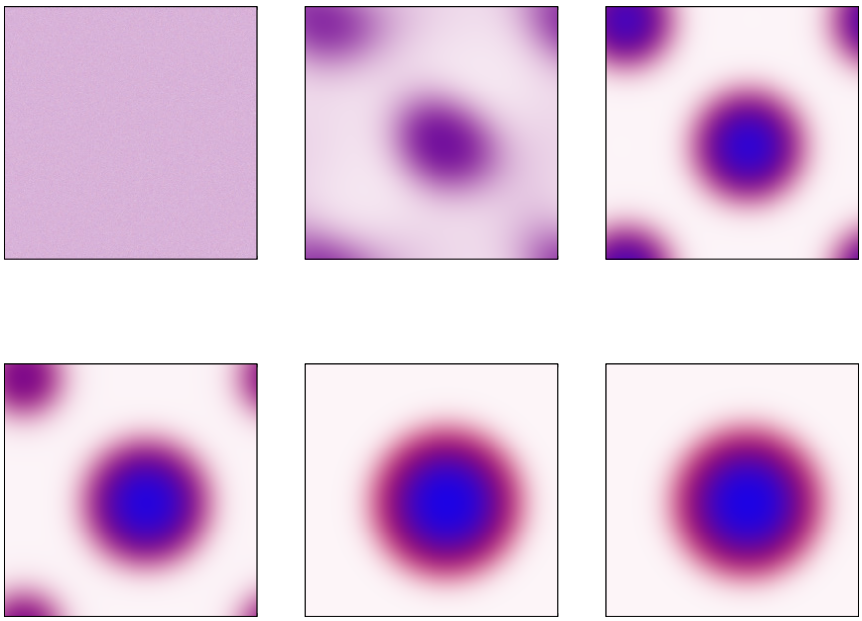


Figure 6.28: $\Omega_{\text{blue}-\text{red}} = 3.0, \Omega_{\text{red}-\text{white}} = 4.0, \Omega_{\text{blue}-\text{white}} = 5.0$, domain length $= \sqrt{2}\pi$nm, i.e. half the length of the simulation box used in figure 6.12.

6.7 CuAg system

Atanasov [71] has carried out Monte Carlo calculations using the Gupta potential in order to obtain the dissolution energies of Cu in Ag and of Ag in Cu, which were found to be 0.276 eV and 0.396 eV respectively. The average of these values, 0.336 eV, is taken as the regular solution parameter $\Omega_{\mathrm{Cu-Ag}}$. The non-dimensional $\Omega_{\mathrm{Cu-Ag}}$ is then equal to $3896/T$, where T is the temperature. To calculate the other two regular solution parameters, $\Omega_{\mathrm{Ag-Vac}}$ and $\Omega_{\mathrm{Cu-Vac}}$, we use the surface energies of Cu ($2.166\mathrm{Jm}^{-2}$) and Ag ($1.210\mathrm{Jm}^{-2}$) [72]. The regular solution parameters may then be calculated using the following equation for the interfacial energy, σ,

$$\sigma = \frac{N_v\sqrt{\kappa\Omega}(\phi_\beta - \phi_\alpha)^3}{3\sqrt{2}}\,, \tag{6.15}$$

which has been derived in ref. [48] for an interface in equilibrium. ϕ_α and ϕ_β are the compositions of the α and β phases respectively, and N_v is the number of atoms per unit volume. Using this equation, we obtain $\Omega_{\mathrm{Ag-Vac}} = 16103/T$ and $\Omega_{\mathrm{Cu-Vac}} = 21742/T$ for the non-dimensional regular solution parameters. At a temperature of 673K, we therefore have $\Omega_{\mathrm{Cu-Ag}} = 5.79$, $\Omega_{\mathrm{Ag-Vac}} = 23.93$ and $\Omega_{\mathrm{Cu-Vac}} = 32.31$.

As has been mentioned earlier, the use of large regular solution parameters leads to numerical instabilities, and as a result, the use of small time steps is required. In the CuAg system, $\Omega_{\mathrm{Cu-Vac}}$ and $\Omega_{\mathrm{Ag-Vac}}$ are signifcantly larger than $\Omega_{\mathrm{Cu-Ag}}$. Because of this, it becomes paractically impossible to

use $\Omega_{\mathrm{Cu-Vac}}$ and $\Omega_{\mathrm{Ag-Vac}}$ as their actual values, and doing so would require extremely small step sizes to maintain stability, making the simulation unfeasible. However, a way of overcoming this problem is to note that the interfacial energy is proportional to $\sqrt{\kappa\Omega}$. Thus, if we scale κ by a factor $\xi\,(\xi > 1)$ and scale Ω by $1/\xi$, the interfacial energy remains unchanged in the model [73, 74]. This means that Ω is reduced, so the instability caused by using large Ω decreases, and we may use larger time steps. It should also be noted that increasing κ leads to more diffuse interfaces.

Figures 6.29 and 6.30 show results from simulations of the CuAg system with $\xi = 5$ and $\xi = 4$ respectively. In all simulations, we let T=673K. The results obtained in the two cases are qualitatively similar, with core-shell particles emerging in the early stages of the simulations and then coarsening to adopt a quasi-Janus configuration. Note that only Ω_{Cu-Vac} and Ω_{Ag-Vac} are scaled — Ω_{Cu-Ag} is left as it is.

Figure 6.31 shows steady-state configurations for particles with varying Cu:Ag ratios. As discussed in section 6.4, particles with thin shells tend to adopt core-shell configurations. This is seen in the 80% Cu case (compare with figure 6.21.

In figures 6.32, 6.33, 6.34 and 6.35, the size of the system is increased by a factor of 3, 10, 20 and 40 respectively (giving a domain length of $6\sqrt{2}\pi$nm, $20\sqrt{2}\pi$nm, $40\sqrt{2}\pi$nm and $80\sqrt{2}\pi$nm respectively). In each case, we observe a transition from core-shell structures to quasi-Janus structures as the particles

grow. In order to simulate larger systems, the nuber of gridpoints used must also be increased. This leads to the requirement to use smaller time steps in order to maintain stability in larger systems. It should also be noted that the initial stages of spinodal decomposition occur on a much shorter timescale than the later stages of particle coarsening. Simulations of the Cahn-Hilliard equation have been shown to display a "freezing" behaviour, whereby the system almost comes to a standstill for the vast majority of the simulation. It can thus be a difficult task to reach the last stage of a simulation, when we are left with just one particle. The simulation shown in figure 6.33, for example, has taken several months to evolve into one particle. Increasing the size of the system further, as we have done to obtain the results shown in figure 6.34 and 6.35 requires even longer simulation times due to the large number of gridpoints required to resolve the interface, and hence the requirement to use smaller time steps.

Finally, figure 6.36 shows a simulation of the CuAg system coupled with elastic effects. The domain length of the system in this case is $10\sqrt{2}\pi$nm.

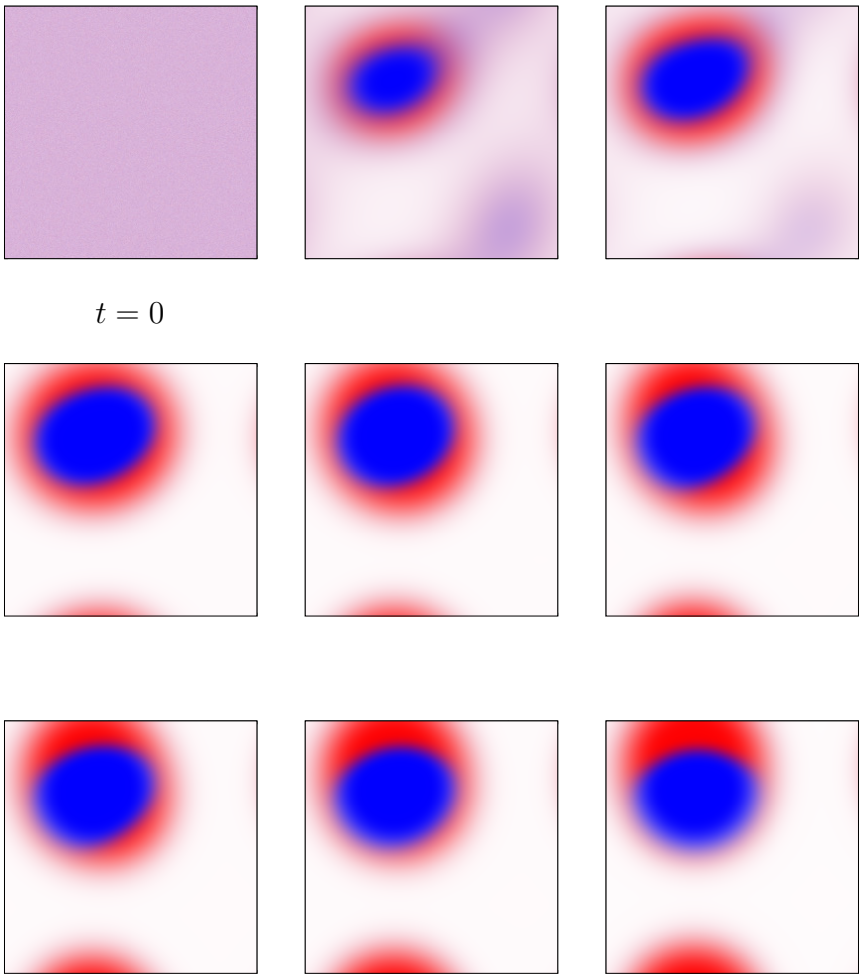


Figure 6.29: Simulation of CuAg system, $\xi = 5$; grid size $= 256 \times 256$, $\Delta t = 1 \times 10^{-}6$.

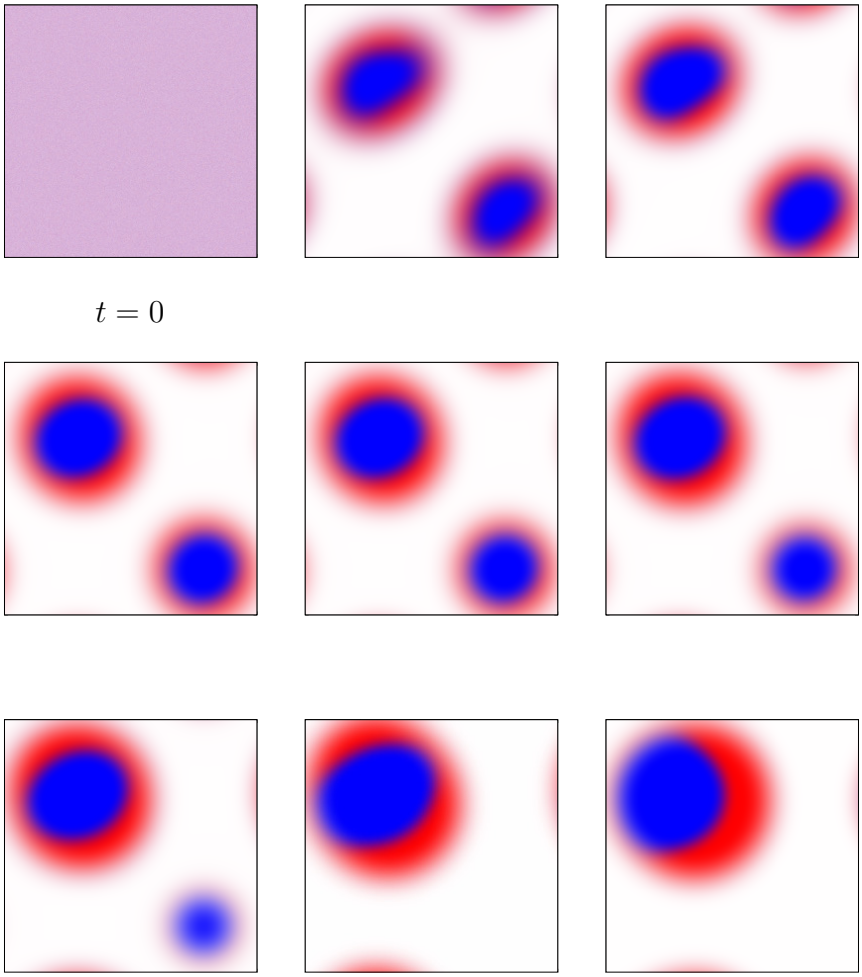
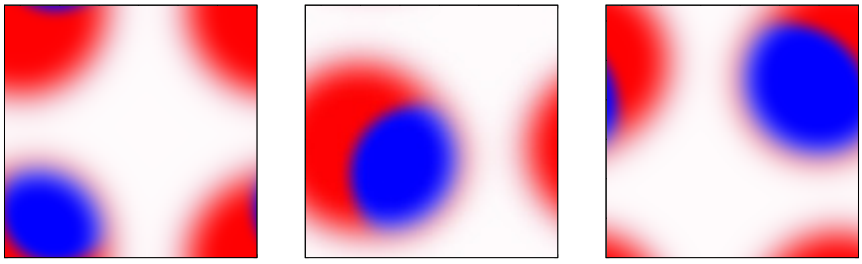
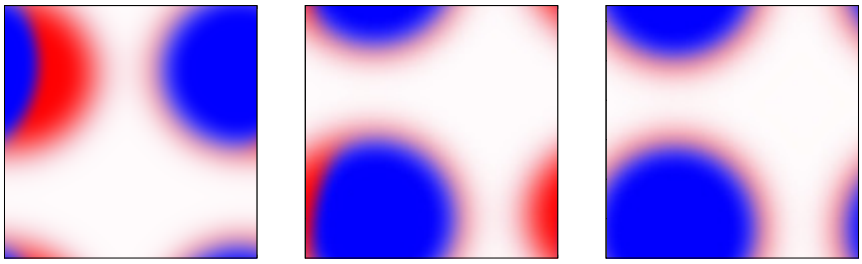


Figure 6.30: Simulation of CuAg system, $\xi = 4$; grid size $= 256 \times 256$, $\Delta t = 3 \times 10^{-8}$.

Varying composition



a) 30 : 70 b) 40 : 60 c) 50 : 50



d) 60 : 40 e) 70 : 30 f) 80 : 20

Figure 6.31: steady-state solutions for CuAg system, with blue : red composition ratios varying from 30 : 70 to 80 : 20. The particle accounts for 40% of the system size. Grid size = 256×256; $\Delta t = 1 \times 10^{-6}$.

Varying size

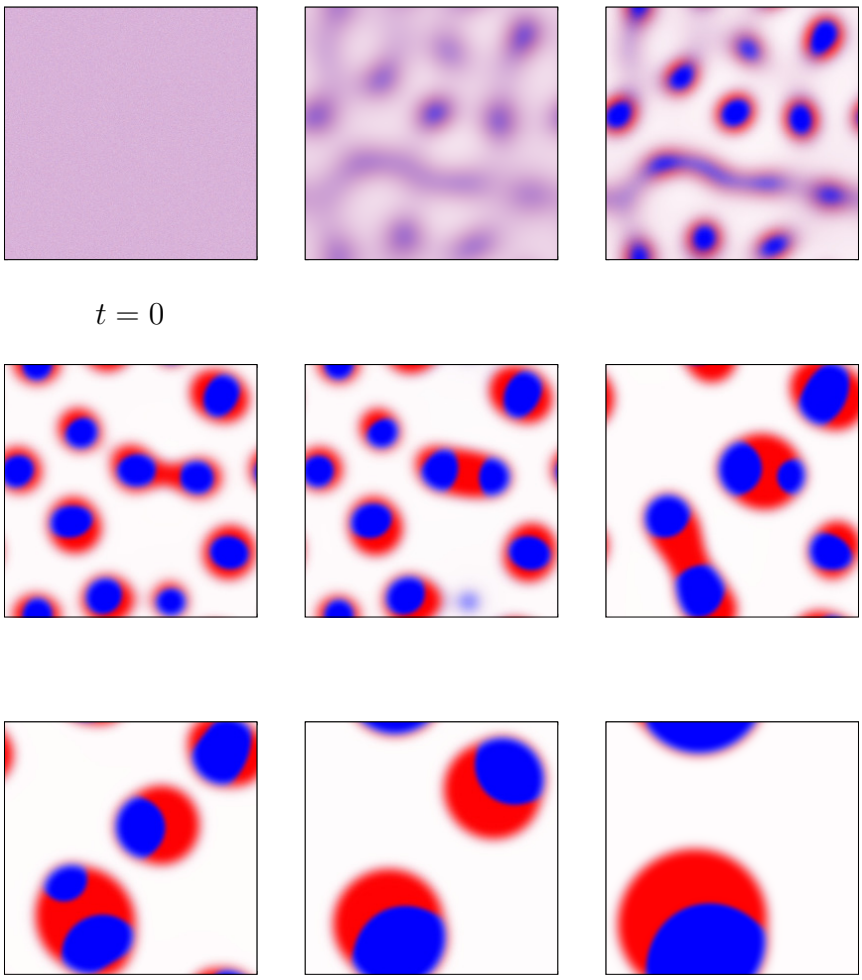


Figure 6.32: Simulation of CuAg system, $\xi = 5$, domain length $= 6\sqrt{2}\pi$nm.

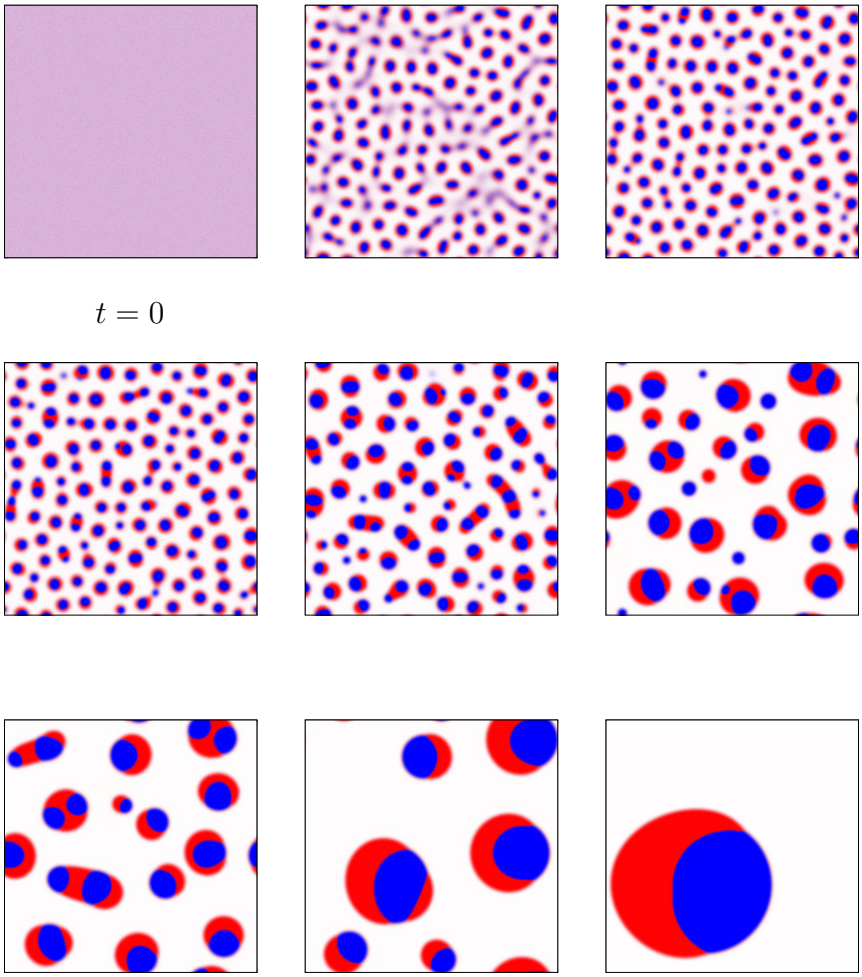


Figure 6.33: Simulation of CuAg system, $\xi = 5$, domain length $= 20\sqrt{2}\pi$nm.

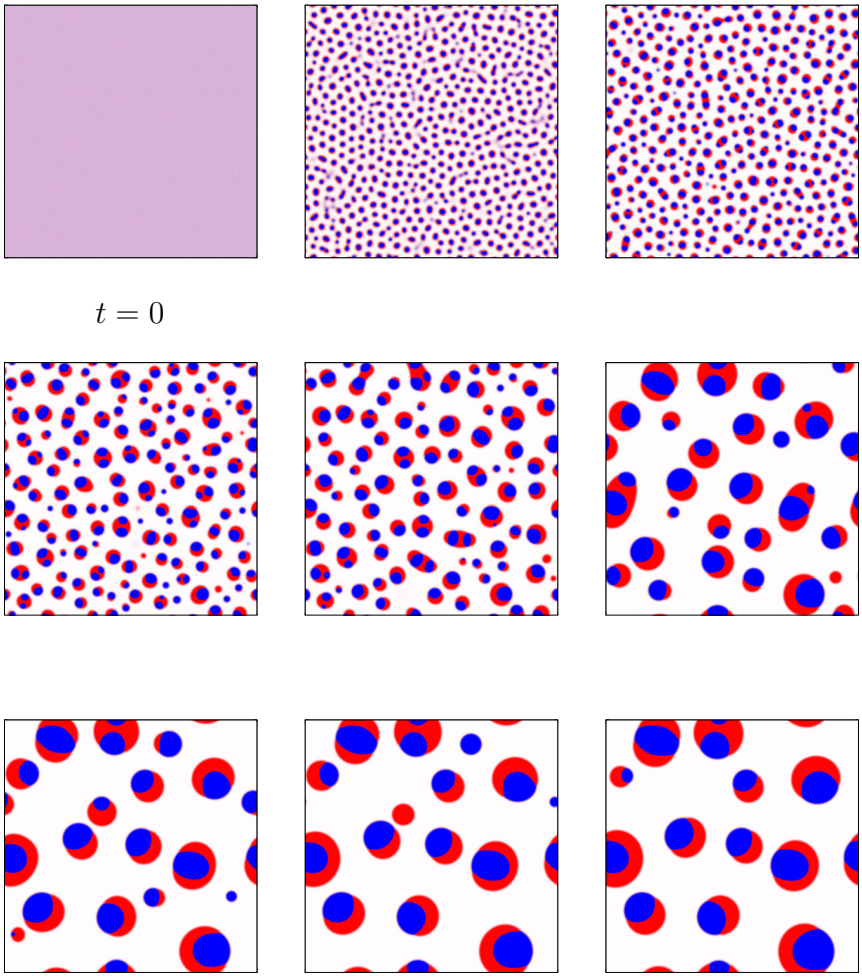


Figure 6.34: Simulation of CuAg system, $\xi = 5$, domain length $= 40\sqrt{2}\pi$nm.

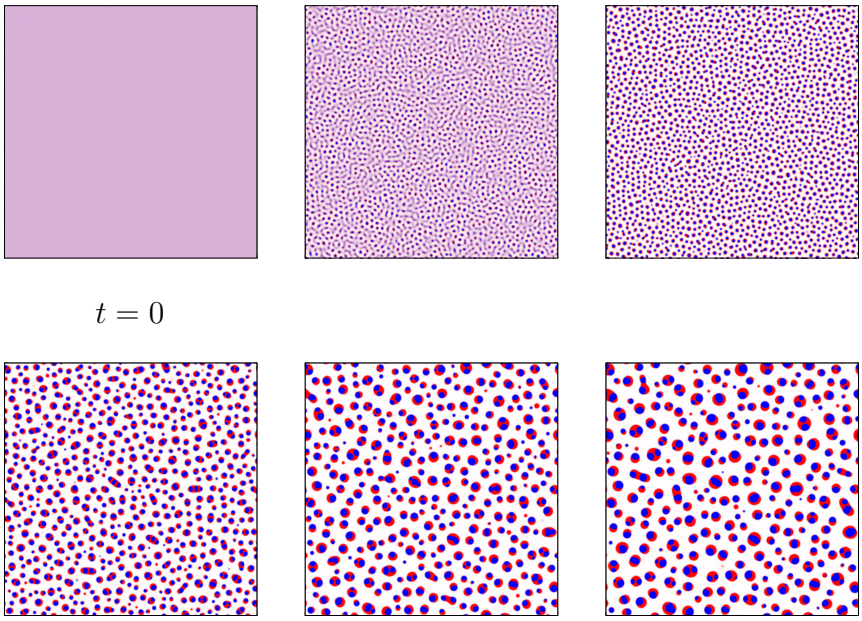


Figure 6.35: CuAg system, $\xi = 5$, domain length $= 80\sqrt{2}\pi$nm, grid size $= 800 \times 800$, $\Delta t = 3 \times 10^{-9}$.

Addition of elastic effects

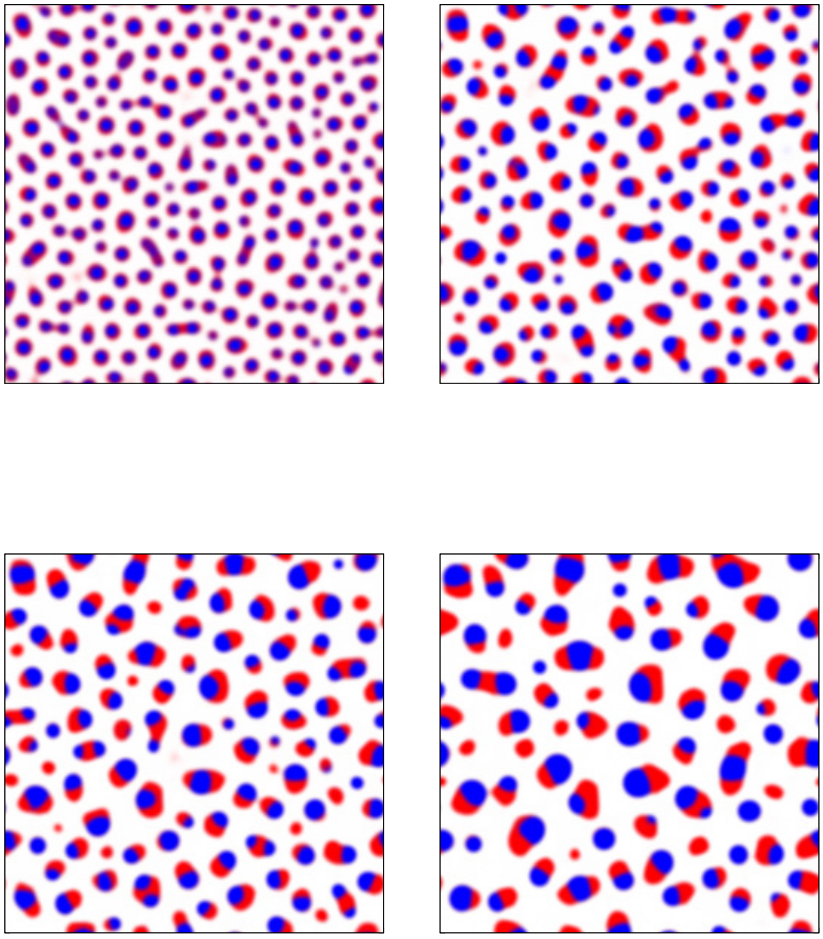


Figure 6.36: CuAg system, with elastic effects included, $\xi = 5$, domain length $= 10\sqrt{2}\pi$nm.

6.8 Discussion

We have used the ternary Cahn-Hilliard equations to model bimetallic nanoparticles in vacuum. By choosing appropriate values for the overall composition of the system, such that the metallic components account for 30–40% of the system, we are able to see the process of spinodal decomposition, leading to the formation, and subsequent coarsening, of particles. It has been shown, in section 6.3, that, by varying the three binary regular solution parameters of the system, we are able to generate core-shell, Janus and quasi-Janus particles. The formation of Janus/quasi-Janus particles begins, in each case, with the formation of core-shell particles which coarsen and coalesce to form Janus particles as the size of the particles increases (section 6.3). Moreover, for cases in which the lowest energy configuration is a core-shell particle, we have demonstrated that, if the size of the system is increased, a transition from core-shell to quasi-Janus particles is observed (section 6.6). The same effects are seen, in section 6.7, for the CuAg system, and our results are in agreement with both experimental findings [12, 11, 14] and previous atomistic simulations [12, 28, 29] in which it has been shown that there is a transition from core-shell to quasi-Janus particles at larger sizes.

In section 6.4, the size of the core has been varied while keeping the overall particle size the same. We have found that, for core-shell particles, the placement of the core varies according to the random fluctuation applied to the initial conditons of each simulation, with $\delta_{\mathrm{off-centre}}$ lying in the range 0 to 0.35. For quasi-Janus particles, we see similar quasi-Janus structures, with

$\delta_{\mathrm{off-centre}} > 0.4$, when the size of the core is varied. However, in all cases, as the core size is increased beyond a certain amount (while maintaining the same size of the particle overall), core-shell particles are preferred. This effect has been demonstrated experimentally in ref. [12], in which it was shown that the thickness of the shell plays an important role in determining whether or not Janus particles are observed, with Janus particles not being seen when the thickness of the Ag shell of the nanoparticle was less than 4nm.

In section 6.5, we have presented simulations in which the ternary Cahn-Hilliard equations are coupled to the Navier-Lamé equations, in order to model the effect of a lattice mismatch between the two metallic components. It is seen that the addition of elastic effects increases significantly the tendency of the nanoparticle core to migrate towards the surface, and that quasi-Janus particles are formed in situations that do not give rise to quasi-Janus particles without elasticity.

In order to see the effects of interfacial energy on the core-shell to Janus particle transition, let us compare the results obtained in section 6.3 to those obtained using a simple analytical model that has been developed by Atanasov [75]. The model approximates a Janus particle as consisting of three spherical caps with volumes, V_i $(i = 1, 2, 3)$, surface areas, S_i, and heights, x_i, as shown in figure 6.37. The three spherical caps share a common circular base, of radius, a. The radii of the spherical caps are then given by

$$r_i = \frac{a^2 + x_i^2}{2x_i} \,. \tag{6.16}$$

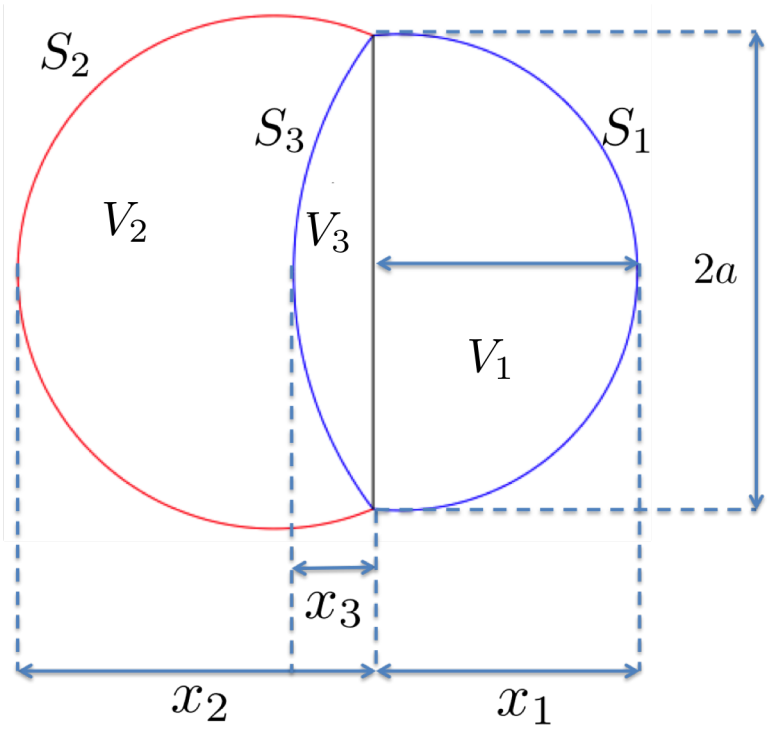


Figure 6.37: Spherical cap model for Janus nanoparticles.

The corresponding volumes are

$$V_i = \frac{\pi x_i^2}{3}\left[2\frac{a^2 + x_i^2}{2x_i} - x_i\right], \tag{6.17}$$

and the surface areas of the caps are

$$S_i = \pi(a^2 + x_i^2)\,. \tag{6.18}$$

In order to obtain the optimal configuration for given interfacial energy densities, σ_{12}, σ_{23} and σ_{13}, we minimise the total interfacial energy, E^{int},

$$E^{\text{int}} = \sigma_{13}S_1 + \sigma_{23}S_2 + \sigma_{12}S_3\,, \tag{6.19}$$

with respect to x_1, x_2, x_3 and a, subject to fixed volumes, V_i. Figure 6.38

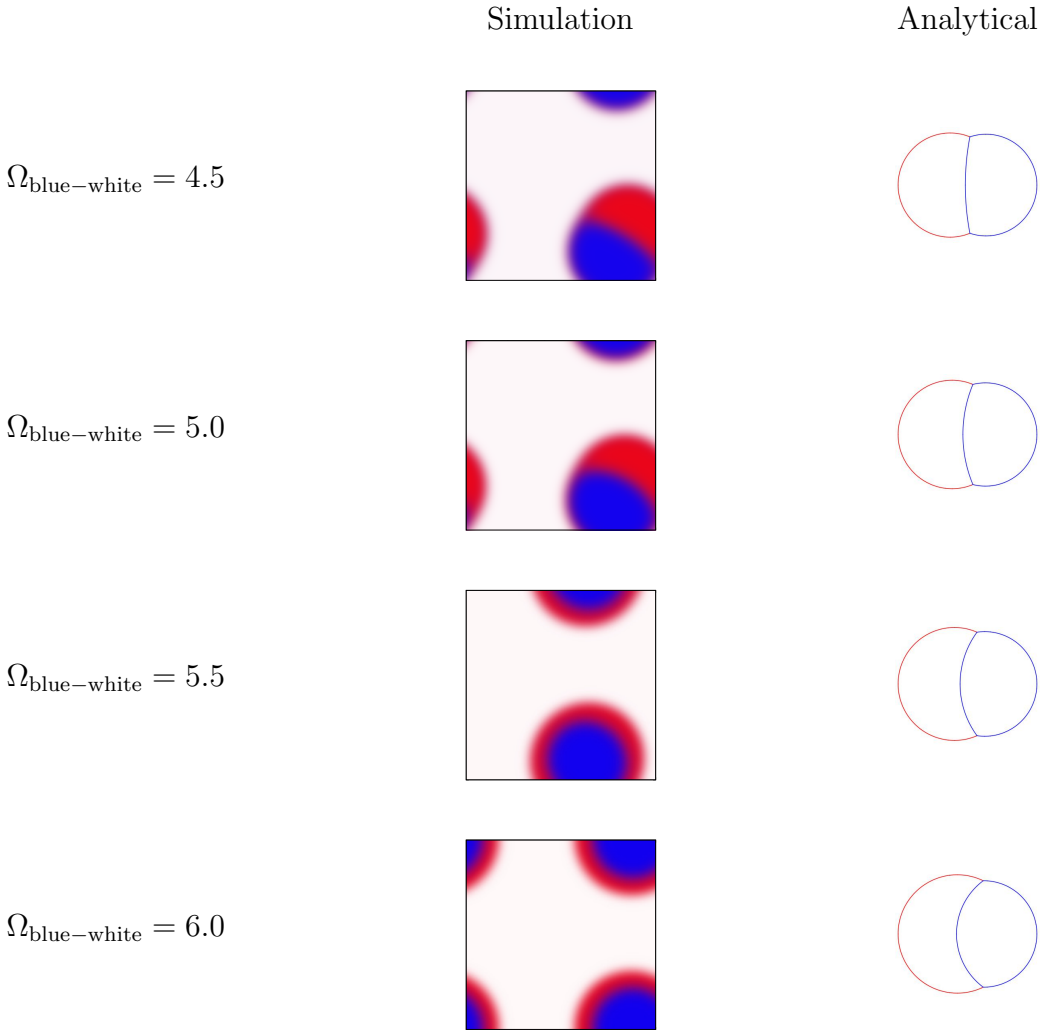


Figure 6.38: Comparison of simulation results with an analytical model. $\Omega_{\text{red-blue}} = 3.0$ and $\Omega_{\text{red-white}} = 4.0$ in each case, while $\Omega_{\text{blue-white}}$ is varied.

shows a comparison between some results obtained in section 6.3 with the analytical model described in this section. In each case $\Omega_{\text{red-blue}} = 3.0$ and $\Omega_{\text{red-white}} = 4.0$, while $\Omega_{\text{blue-white}}$ is varied. Notice how the dihedral angles change as $\Omega_{\text{blue-white}}$ increases, giving a more curved red-blue interface. Ac-

cording to the analytical model, ball-and-cup particles are the lowest energy configurations if $\Omega_{\text{blue-white}} > \Omega_{\text{red-white}} > \Omega_{\text{blue-red}}$, as long as $\Omega_{\text{blue-white}} < \Omega_{\text{red-white}} + \Omega_{\text{blue-red}}$. If, on the other hand, $\Omega_{\text{blue-white}} > \Omega_{\text{red-white}} + \Omega_{\text{blue-red}}$, we obtain a core-shell particle as the lowest energy configuration, as shown in figure 6.39. This follows from Neumann's Law, which states that any one of the interfacial energies in a ternary system cannot exceed the sum of the other two, in order for a triple point to exist. The problem with the ana-

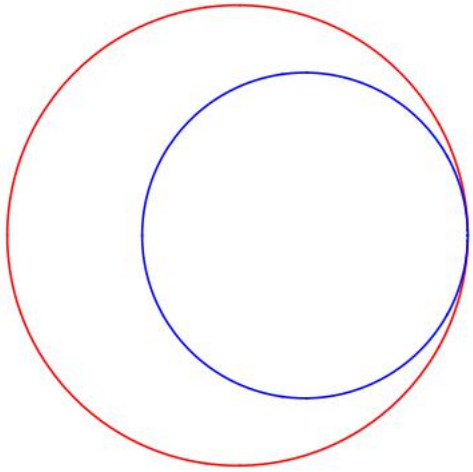


Figure 6.39: Core-shell particles are seen in the analytical model when $\Omega_{\text{blue-white}} > \Omega_{\text{red-white}} + \Omega_{\text{blue-red}}$. Although the core is off-centred, it is beneath the surface, and hence equivalent to a centred core-shell particle in the analytical model.

lytical model is that size effects are not taken into account, and the results obtained are independent of the size of the particle. For the simulations shown in figure 6.38, when $\Omega_{\text{blue-white}} = 5.5$, we obtain a core-shell particle as the steady-state solution. However, when the size of the system is increased, we obtain a Janus particle, as shown in figure 6.27. The analytical

model is therefore not adequate in describing the core-shell to Janus particle transition observed in bimetallic nanoparticles.

One effect that is missing from the analytical model is that of strain. It is generally agreed upon that the main cause of the core-shell to Janus particle transition, in systems such as CuAg, is the presence of strain at the atomic level [28, 29]. It is interesting to note, however, that the transition is observed both with and without the inclusion of elastic effects in our model. This leads us to believe that, in the Cahn-Hilliard model, there must be an influence of curvature on the interfacial energy, which leads to Janus particles being observed at larger sizes while core-shell particles prevail at smaller sizes.

Tolman [76] proposed a first order curvature correction to the surface tension of a spherical droplet in 1949. He assumed that the surface tension, σ, may be related to σ_0, the surface tension of a flat interface, via the relation

$$\sigma = \sigma_0 \left(1 - \frac{2\delta_T}{R_s} \right), \tag{6.20}$$

where R_s is the position of the *surface of tension*, and δ_T is the *Tolman length*, which is defined as the distance between the *equimolar surface* and the *surface of tension* [76, 77, 78]. To this day, however, there is still controversy over both the sign of the Tolman length and its magnitude [79]. Gránásy et al. [80] have studied the Tolman length in the context of Cahn-Hilliard theory and have found that δ_T itself is strongly size-dependent. Related to the concept of the Tolman length is the concept of *bending energy*, which has

been used to study the shape of lipid bilayers and the processes of budding and fusion in biological membranes [81, 82, 83, 84]. The study of the effects of curvature and the concept of the Tolman length in the context of the ternary Cahn-Hilliard model presented in this work is left as a future endeavour.

Chapter 7

FUTURE WORK

Although we have been able to model the core-shell to quasi-Janus particle transition in bimetallic nanoparticles, using a ternary Cahn-Hilliard system of equations, several challenges need to be faced in order to extend this work significantly. The most important of these is, perhaps, the challenge in applying the method presented in this work *quantitatively* to real systems, such as the CuAg nanoparticle system. The main problem in doing so is the inherent stiffness associated with the Cahn-Hilliard equations. Although much work has been devoted to tackling the issue of stiffness arising due to the linear term in the Cahn-Hilliard equation (see chapter 4), there has been little work in the way of addressing the stiffness caused by the nonlinear term. Indeed, this stiffness is amplified by the use of large regular solution parameters, and prohibitively small time step sizes are subsequently required to quantitatively model real systems using the ternary Cahn-Hilliard equations. Moreover, when coupling the Cahn-Hilliard equations with elasticity, at each time step, the majority of computational time is spent on the solution of the Navier-Lamé equations. In addition to this, increasing the size of the

system being modelled requires the use of finer computational grids and is therefore computationally expensive. It is, therefore, important to develop new solution techniques which improve upon the efficiency of the spectral methods presented in chapter 4.

In terms of understanding the physical effects seen in the simulations presented in this work, a natural next step would be to study the effects of curvature on the transition from core-shell to quasi-Janus particle structure. In this respect, it would be interesting to see whether or not the concept of the Tolman Length may be applied.

Having applied the ternary Cahn-Hilliard model to obtain qualitative results for the CuAg system, we may extend this work to the modelling of other bimetallic nanoparticle systems. However, further work is also required to ascertain the limits of the applicability of rescaling the gradient energy coefficients and regular solution parameters when trying to obtain qualitative results for real nanoparticle systems (section 6.7).

List of References

[1] R. Ferrando, J. Jellinek, and R.L. Johnston. Nanoalloys: From theory to applications of alloy clusters and nanoparticles. *Chemical Reviews*, 108(3):845–910, 2008.

[2] M. Gaudry, E. Cottancin, M. Pellarin, J. Lermé, L. Arnaud, J. R. Huntzinger, J. L. Vialle, M. Broyer, J. L. Rousset, M. Treilleux, and P. Mélinon. Size and composition dependence in the optical properties of mixed (transition metal/noble metal) embedded clusters. *Phys. Rev. B*, 67:155409, 2003.

[3] E. Cottancin, J. Lermé, M. Gaudry, M. Pellarin, J.-L. Vialle, M. Broyer, B. Prével, M. Treilleux, and P. Mélinon. Size effects in the optical properties of $au_n ag_n$ embedded clusters. *Phys. Rev. B*, 62:5179–5185, 2000.

[4] N.L. Rosi and C.A. Mirkin. Nanostructures in biodiagnostics. *Chem. Rev.*, 105(4):1547–1562, 2005.

[5] J.H. Sinfelt. Supported Bimetallic-Cluster Catalysts. *J. Catalysis*, 29(2):308–315, 1973.

[6] S. Alayoglu, A.U. Nilekar, M. Mavrikakis, and B. Eichhorn. *Nature Materials*, 7:333–338, 2008.

[7] Silver nanoparticles as antimicrobial agent: a case study on e. coli as a model for gram-negative bacteria. *Journal of Colloid and Interface Science*, 275(1):177 – 182, 2004.

[8] J. S. Kim *et al.* Antimicrobial effects of silver nanoparticles. *Nanomedicine: Nanotechnology, Biology and Medicine*, 3(1):95 – 101, 2007.

[9] R.L. Johnston. Chapter 1 - metal nanoparticles and nanoalloys. In R.L. Johnston and J.P. Wilcoxon, editors, *Metal Nanoparticles and Nanoalloys*, volume 3 of *Frontiers of nanoscience*. Elsevier, 2012.

[10] D Bochicchio and R Ferrando. Structure and thermal stability of AgCu chiral nanoparticles. *Eur. Phys. J. D*, 66(115), 2012.

[11] C. Langlois, D. Alloyeau, Y. Le Bouar, A. Loiseau, T. Oikawa, C. Mottet, and C. Ricolleau. Growth and structural properties of CuAg and CoPt bimetallic nanoparticles. *Faraday Discuss.*, 138:375–391, 2008.

[12] C.T. Langlois, Z.L. Li, J. Yuan, D. Alloyeau, Nelayah, D. Bochicchio, R. Ferrando, and C. Ricolleau. Transition from core-shell to janus chemical configuration for bimetallic nanoparticles. *Nanoscale*, 4:3381–3388, 2012.

[13] C.T. Langlois, T. Oikawa, P. Bayle-Guillemaud, and C. Ricolleau. Energy-filtered electron microscopy for imaging core-shell nanostructures. *J. Nanopart. Res.*, 10:997–1007, 2008.

[14] M. Cazayous, C.T. Langlois, T. Oikawa, C. Ricolleau, and A. Sacuto. Cu-ag core-shell nanoparticles: A direct correlation between micro-raman and electron microscopy. *Phys. Rev. B*, 73:113402, Mar 2006.

[15] J. Belloni, M. Mostafavi, H. Remita, J-L Marignier, and M-O Delcourt. Radiation-induced synthesis of mono- and multi-metallic clusters and nanocolloids. *New J. Chem.*, 22:1239–1255, 1998.

[16] E Janssens, S Neukermans, X Wang, N Veldeman, RE Silverans, and P Lievens. Stability patterns of transition metal doped silver clusters: Dopant- and size-dependent electron delocalization. *Eur. Phys. J. D*, 34(1-3):23–27, 2005. 12th International Symposium on Small Particles and Inorganic Clusters, Nanjing, PEOPLES R CHINA, SEP 06-10, 2004.

[17] H.Y. Kang, C.Y. Peng, H.P. Wang, W.-K. Lin, I.-W. Sun, and S.-G. Chang. Preparation of ag nanospheres filled with cu. *Journal of Experimental Nanoscience*, 10(12):937 – 946, 2015.

[18] M. Pellarin, I. Issa, C. Langlois, M.-A. Lebeault, J. Ramade, J. Lerm, M. Broyer, and E. Cottancin. Plasmon spectroscopy and chemical structure of small bimetallic $Cu_{1-x}Ag_x$ clusters. *J. Phys. Chem. C*, 119(9):5002–5012, 2015.

[19] F. Baletto, C. Mottet, and R. Ferrando. Time evolution of Ag-Cu and Ag-Pd core-shell nanoclusters. *Eur. Phys. J. D*, 24:233–236, 2003.

[20] F. Baletto, C. Mottet, and R. Ferrando. Growth of three-shell onionlike bimetallic nanoparticles. *Phys. Rev. Lett.*, 90:135504, Apr 2003.

[21] G. Rossi, A. Rapallo, C. Mottet, A. Fortunelli, F. Baletto, and R. Ferrando. Magic polyicosahedral core-shell clusters. *Phys. Rev. Lett.*, 93:105503, 2004.

[22] L. Delfour, J. Creuze, and B. Legrand. Exotic behavior of the outer shell of bimetallic nanoalloys. *Phys. Rev. Lett.*, 103:205701, 2009.

[23] D. Bochicchio and R. Ferrando. Size-Dependent Transition to High-Symmetry Chiral Structures in AgCu, AgCo, AgNi, and AuNi Nanoalloys. *Nano Letters*, 10(10):4211–4216, 2010.

[24] D. Bochicchio and R. Ferrando. Structure and thermal stability of agcu chiral nanoparticles. *Eur. Phys. J. D*, 66:115, 2012.

[25] A. Rapallo, G. Rossi, R. Ferrando, A. Fortunelli, B.C. Curley, L.D. Lloyd, G.M. Tarbuck, and R.L. Johnston. Global optimization of bimetallic cluster structures. i. size-mismatched ag?cu, ag?ni, and au?cu systems. *J. Chem. Phys.*, 122(19):–, 2005.

[26] R. Ferrando, A. Fortunelli, and G. Rossi. Quantum effects on the structure of pure and binary metallic nanoclusters. *Phys. Rev. B*, 72:085449, Aug 2005.

[27] S. Nez and R. L. Johnston. Structures and chemical ordering of small cu?ag clusters. *J. Phys. Chem. C*, 114(31):13255–13266, 2010.

[28] D. Bochicchio and R. Ferrando. Morphological instability of core-shell metallic nanoparticles. *Phys. Rev. B*, 87:165435, Apr 2013.

[29] R. Ferrando. Symmetry breaking and morphological instabilities in core-shell metallic nanoparticles. *J. Phys.: Condens. Matter*, 27(1):013003, 2015.

[30] W.J. Boettinger, J.A. Warren, C. Beckermann, and A. Karma. Phase-field simulation of solidification. *Annu. Rev. Mater. Res.*, 32:163–194, 2002.

[31] J.W. Cahn. On spinodal decomposition. *Act. Met.*, 9:795–801, 1961.

[32] JW Cahn and JE Hilliard. FREE ENERGY OF A NONUNIFORM SYSTEM .1. INTERFACIAL FREE ENERGY. *J. CHEM. PHYS.*, 28(2):258–267, 1958.

[33] G. Caginalp and W. Xie. Phase-field and sharp-interface alloy models. *Phys. Rev. E*, 48:1897–1909, 1993.

[34] J. Crank. *Free and moving boundary value problems*. Clarendon Press, Oxford, 1987.

[35] F.J. Vermolen, C. Vuik, E. Javierre, and S. van der Zwang. Review on some stefan problems for particle dissolution in solid metallic alloys. *Nonlinear Analysis: Modelling and Control*, 10(3):257–292, 2005.

[36] N. Moelans, B. Blanpain, and P. Wollants. An introduction to phase-field modeling of microstructure evolution. *Calphad*, 32(2):268–294, 2008.

[37] L-Q Chen. Phase-Field Models for Microstructure Evolution. *Annu. Rev. Mater. Res.*, 32:113–140, 2002.

[38] JW Cahn. Free Energy of a Nonuniform System .2. Thermodyanmic Basis. *J. Chem. Phys.*, 30(5):1121–1124, 1959.

[39] JW Cahn and JE Hilliard. FREE ENERGY OF A NONUNIFORM SYSTEM .3. NUCLEATION IN A 2-COMPONENT INCOMPRESSIBLE FLUID. *J. Chem. Phys.*, 31(3):688–699, 1959.

[40] J.S. Rowlinson and B. Widom. *Molecular theory of capillarity*. Clarendon Press, Oxford, 1982.

[41] SM Allen and JW Cahn. MICROSCOPIC THEORY FOR ANTIPHASE BOUNDARY MOTION AND ITS APPLICATION TO ANTIPHASE DOMAIN COARSENING. *Acta Met.*, 27(6):1085–1095, 1979.

[42] AA Wheeler, WJ Boettinger, and GB McFadden. Phase-field model for isothermal phase transitions in binary alloys. *Phys. Rev. A*, 45(10):7424–7440, 1992.

[43] P.D. Olmsted. Lectures on Landau Theory of Phase Transitions. `http://www1.physics.leeds.ac.uk/~phy6pdo/teaching/landau.pdf`, 2000. Accessed: 30 May 2015.

[44] J.M. Yeomans. *Statistical Mechanics of Phase Transitions*. Oxford University Press, 1992.

[45] N. Provatas and K. Elder. *Phase-Field Methods in Materials Science and Engineering*. Wiley-VCH, 2010.

[46] V.L. Ginzburg and L.D. Landau. On the theory of superconductivity. *Zh. Exsp. Teor. Fiz.*, 20:1064, 1950.

[47] L. A. Girifalco. *Statistical Mechanics of Solids*. Oxford University Press, 2000.

[48] E.A. Lass, W.C. Johnson, and G.J. Shiflet. Correlation between {CALPHAD} data and the cahn-hilliard gradient energy coefficient and exploration into its composition dependence. *Calphad*, 30(1):42 – 52, 2006.

[49] A. Baldan. Progress in ostwald ripening theories and their applications to nickel-base superalloys. part i: Ostwald ripening theories. *J. Mat. Sci.*, 37(11):2171–2202, 2002.

[50] L.Q. Chen and A.G. Khachaturyan. Computer simulation of structural transformations during precipitation of an ordered intermetallic phase. *Acta Mater.*, 39(11):2533 – 2551, 1991.

[51] AA Wheeler, WJ Boettinger, and GB McFadden. Phase-field model for isothermal phase transitions in binary alloys. *Phys. Rev. E*, 47(3):1893–1909, 1993.

[52] I Steinbach, F Pezzolla, B Nestler, M Seesselberg, R Prieler, GJ Schmitz, and JLL Rezende. A phase field concept for multiphase systems. *Physica D*, 94(3):135–147, 1996.

[53] D.J. Eyre. Systems of cahn-hilliard equations. *SIAM J. Applied Mathematics*, 53:1686–1712, 1993.

[54] J.E Morral and J.W Cahn. Spinodal decomposition in ternary systems. *Acta Met.*, 19(10):1037 – 1045, 1971.

[55] L.Q. Chen and Jie Shen. Applications of semi-implicit fourier-spectral method to phase field equations. *Computer Physics Communications*, 108(2-3):147 – 158, 1998.

[56] SM Cox and PC Matthews. Exponential time differencing for stiff systems. *J. Comp. Phys.*, 176:430–455, 2002.

[57] D.J. Eyre. An Unconditionally Stable One-Step Scheme for Gradient Systems. `http://www.math.utah.edu/~eyre/research/methods/stable.ps`, 1998. Accessed: 30 May 2015.

[58] Y. Oono and S. Puri. Study of phase-separation dynamics by use of cell dynamical systems. i. modeling. *Phys. Rev. A*, 38:434–453, Jul 1988.

[59] W.H. Press, S.A.Teukolsky, W.T. Vetterling, and B.P. Flannery. *Numerical Recipes. The Art of Scientific Computing.* Cambridge University Press, 3rd edition, 2007.

[60] A-K Kassam and LN Trefethen. FOURTH-ORDER TIME STEPPING FOR STIFF PDES. *SIAM Journal on Scientific Comptuing*, 26:1214–1233, 2005.

[61] B.P. Vollmayr-Lee and A.D. Rutenberg. Fast and accurate coarsening simulation with an unconditionally stable time step. *Phys. Rev. E*, 68:066703, Dec 2003.

[62] M. Cheng and A.D. Rutenberg. Maximally fast coarsening algorithms. *Phys. Rev. E*, 72:055701, 2005.

[63] G Söderlind and L Wang. Adaptive Time-stepping and Computational Stability. *Journal of Computational Methods in Sciences and Engineering*, 2(3):1–19, 2003.

[64] W.C. Johnson. Influence of elastic stress on phase transformations. In H.I. Aaronson, editor, *Lectures on the Theory of Phase Transformations*. TMS Publications, 2nd edition, 1999.

[65] P. Fratzl, O. Penrose, and J.L. Lebowitz. Modeling of phase separation in alloys with coherent elastic misfit. *J. Stat. Phys.*, 95(5-6):1429–1503, 1999.

[66] P.H. Leo, J.S. Lowengrub, and H.J. Jou. A diffuse interface model for microstructural evolution in elastically stressed solids. *Acta Mater.*, 46(6):2113 – 2130, 1998.

[67] S.Y. Hu and L.Q. Chen. A phase-field model for evolving microstructures with strong elastic inhomogeneity. *Acta Mater.*, 49(11):1879 – 1890, 2001.

[68] M.P. Gururajan and T.A. Abinandanan. Phase field study of precipitate rafting under a uniaxial stress. *Acta Mater.*, 55(15):5015 – 5026, 2007.

[69] M.P. Gururajan. *Elastic inhomogeneity effects on microstructures — a phase field study.* PhD thesis, Indian Institute of Science, 2006.

[70] F. Cleri and V. Rosato. Tight-binding potentials for transition metals and alloys. *Phys. Rev. B*, 48:22–33, 1993.

[71] I. Atanasov, 2013. Personal communication.

[72] L. Vitos, A.V. Ruban, H.L. Skriver, and J. Kollár. The surface energy of metals. *Surface Science*, 411:186 – 202, 1998.

[73] A. Karma. Phase-field formulation for quantitative modeling of alloy solidification. *Phys. Rev. Lett.*, 87:115701, 2001.

[74] C. Shen, Q. Chen, Y.H. Wen, J.P. Simmons, and Y. Wang. Increasing length scale of quantitative phase field modeling of concurrent growth and coarsening processes. *Scripta Materialia*, 50(7):1029 – 1034, 2004.

[75] I. Atanasov. Spherical cap model for janus nanoparticles. *Unpublished work*, 2012.

[76] R.C. Tolman. The effect of droplet size on surface tension. *J. Chem. Phys.*, 17(3):333–337, 1949.

[77] G. Sh. Boltachev, V.G. Baidakov, and J.W.P. Schmelzer. First-order curvature corrections to the surface tension of multicomponent systems. *Journal of Colloid and Interface Science*, 264(1):228 – 236, 2003.

[78] H. Vehkamäki. *Classical Nucleation Theory in Multicomponent Systems*. Springer-Verlag, 2011.

[79] Y.A. Lei, T. Bykov, S. Yoo, and X.C. Zeng. The tolman length: Is it positive or negative? *Journal of the American Chemical Society*, 127(44):15346–15347, 2005.

[80] L. Gránásy. Semiempirical van der waals/cahn-hilliard theory: Size dependence of the tolman length. *J. Chem. Phys.*, 109(22):9660–9663, 1998.

[81] R. Lipowsky. The conformation of membranes. *Nature*, 349:475–481, 1991.

[82] R. Lipowsky. Domain induced budding of fluid membranes. *Biophys. J.*, 64:1133–1138, 1993.

[83] F. Jülicher and R. Lipowsky. Domain-induced budding of vesicles. *Phys. Rev. Lett.*, 70:2964–2967, 1993.

[84] F. Campelo and A. Hernandez-Machado. Shape instabilities in vesicles: A phase-field model. *Eur. Phys. J. Special Topics*, 143(1):101–108, 2007.